Bachelor's project

NTNU
Norwegian University of Science and Technology
Faculty of Natural Sciences
Department of Materials Science and Engineering

Ingeborg Ellingsen
Camilla Jektvik
Nora Kvalsvik

Sustainable Cathode Production for Lithium-Ion Batteries

Bachelor's project in Materials Science and Engineering
Supervisor: Ann Mari Svensson
Co-supervisor: Silje Nornes Bryntesen

May 2021

NTNU
Kunnskap for en bedre verden

Ingeborg Ellingsen
Camilla Jektvik
Nora Kvalsvik

Sustainable Cathode Production for Lithium-Ion Batteries

Bachelor's project in Materials Science and Engineering
Supervisor: Ann Mari Svensson
Co-supervisor: Silje Nornes Bryntesen
May 2021

Norwegian University of Science and Technology
Faculty of Natural Sciences
Department of Materials Science and Engineering

NTNU
Kunnskap for en bedre verden

NTNU
Norwegian University of
Science and Technology

Faculty of Natural Sciences

TMAK3001 - Bachelor thesis

Sustainable Cathode Production for Lithium-Ion Batteries

Authors:
Ingeborg Ellingsen
Nora Kvalsvik
Camilla Jektvik

Supervisors:
Ann Mari Svensson
Odne S. Burheim
Silje N. Bryntesen
Jacob Joseph Lamb

Client:
NTNU/FREYR

Contact person:
Silje N. Bryntesen

Project number: IMA-B-12-2021

Open paper

May, 2021

NTNU
Norwegian University of Science and Technology

Fakultet for naturvitenskap

TMAK3001 - Bachelor oppgave

Bærekraftig katodeproduksjon for litiumionebatteri

Forfattere:
Ingeborg Ellingsen
Nora Kvalsvik
Camilla Jektvik

Veiledere:
Ann Mari Svensson
Odne S. Burheim
Silje N. Bryntesen
Jacob Joseph Lamb

Oppdragsgiver:
NTNU/FREYR

Kontaktperson:
Silje N. Bryntesen

Prosjektnummer: IMA-B-12-2021

Åpen oppgave

Mai, 2021

Abstract

In recent years Lithium-ion batteries (LIBs) have become the corner-stone of energy storage for electrification of the transport sector. Significant improvements are still needed to enhance their manufacturing sustainability. The current state-of-the-art cathode material of Lithium-ion batteries consist of the active material $LiNi_{1/3}Mn_{1/3}Co_{1/3}O_2$ (NMC111), the electrical conductive agent Carbon Black (CB), and Polyvinylidene fluoride (PVDF) binder.

This thesis assesses a more sustainable cathode production for LIBs. Initially, slurry parameters are varied to find the optimal slurry composition in terms of mechanical and electrochemical performance. It concludes with a 85:10:5 wt% (NMC111:CB:PVDF) with a 1:2 ratio of powder to solvent, which achieved an initial discharge capacity of 156 mAh/g (C/10) and capacity retention of 93 % after 19 cycles.

The PVDF binder is only soluble in a few toxic solvents, such as *N*-methyl-2-pyrrolidone (NMP). The NMP solvent needs to be recovered through post-drying, which is one of the most energy intensive process steps within the cathode manufacturing. In an attempt to eliminate the recovery step, the PVDF binder was gradually replaced with lignin, an abundant, plant-derived, and water-soluble material. In general, an increasing amount of lignin lead to decreasing mechanical properties and cycling capacity. Using pure lignin as a binder with NMP as a solvent caused strong cohesion between the particles but low adhesion between the current collector and cathode material. Both the electrochemical performance and adhesion to the current collector increased when the drying temperature was lowered from 90 °C to 50 °C. The pure unleached lignin sample dried at 50 °C impressively achieved an initial discharge capacity of 138 mAh/g, 140 mAh/g and 141 mAh/g on the 1st, 3rd and 4th cycle with a C-rate of C/10, respectively. When the C-rate was upped to C/2, the sample achieved a discharge capacity of 124 mAh/g at cycle 14. With the exception of the sample using pure lignin as binder, calendering increased both the mechanical and electrochemical performance of the cathodes.

After successfully exchanging the PVDF binder with lignin the NMP solvent was exchanged with water, to completely eliminate the energy-intensive recovery step. This was unsuccessful, and resulted in thin slurries and uneven coating thickness. The problems were partly solved by adding phosphoric acid (PA). Lowering the pH of the slurry improved both slurry properties and adhesion to the current collector. This is a promising avenue for further work.

As a sub-goal, the thesis aimed to optimise the drying procedure for the cathode coatings. Temperature and air velocity were varied in a custom-made convection oven. Higher temperatures resulted in shorter drying times, and the difference was more pronounced at lower temperatures. An increase from 50 °C to 90 °C resulted in a 77% decrease in drying time, while an increase from 90 °C to 150 °C resulted in a 44% decrease in drying time. Higher air velocities were tougher on the samples. Decreasing the air velocity from 1.0 m/s to 0.5 m/s had larger effects on cracking than temperature, with less cracking on lower air velocity. EDS analyses of a standard sample dried at 50 °C showed even distribution of the NMC111, but some agglomeration of CB. The binder was evenly distributed within the material. Uneven coatings and varying coating geometry caused issues with the reproducibility throughout the drying experiments.

Suggestions for future work are presented. These focus on improving the procedures used in this thesis, and on replacing the toxic solvent NMP with water. Closer investigations should be made on how production parameters can be altered to make aqueous cathode slurries easier to work with.

Sammendrag

De siste årene har litiumionebatterier (LIB) inntatt en sentral rolle i energilagring for elektrifiseringen av transportsektoren. Det gjenstår fortsatt omfattende utvikling for at produksjonen skal bli bærekraftig. Det markedsledende katodematerialet består av det aktive materialet $LiNi_{1/3}Mn_{1/3}Co_{1/3}O_2$ (NMC111), det elektrisk ledende materialet Carbon Black (CB), og bindemiddelet polyvinyliden fluorid (PVDF).

Denne oppgaven undersøker hvordan katodeproduksjon for LIB kan bli mer bærekraftig. Innledningsvis ble slurry-parametre endret for å finne optimal sammensetning for mekanisk og elektrokjemisk ytelse. Det resulterte i et prosentvis vektforhold på 85:10:5 for NMC111:CB:PVDF, med prosentvis vektforhold på 1:2 mellom faste stoffer og løsemiddel. Denne sammensetningen oppnådde en initiell utladningskapasitet på 156 mAh/g (C/10) og en kapasitetsretensjon på 93 % etter 19 sykler.

Bindemiddelet PVDF er kun løselig i noen få, giftige løsemidler, eksempelvis N-metyl-2-pyrrolidon (NMP). NMP må ekstraheres etter tørking, og dette utgjør en av de mest energikrevende prosessene i hele katodeproduksjonen. I et forsøk på å eliminere dette produksjonssteget ble bindemiddelet PVDF erstattet med lignin, som er et fornybart, vannløselig plantemateriale. Generelt ledet økende mengde lignin til dårligere mekaniske egenskaper samt syklekapasitet. Rent lignin med NMP som løsemiddel ga sterk partikkelkohesjon, men lav adhesjon mellom strømsamleren og katodematerialet. Både adhesjonen til strømsamleren og den elektrokjemiske ytelsen økte når tørketemperaturen ble senket fra 90 °C til 50 °C. Prøven med rent, ufiltrert lignin tørket på 50 °C oppnådde en initiell utladningskapasitet på hele 138 mAh/g, 141 mAh/g og 140 mAh/g under henholdsvis første, tredje og fjerde sykel med en C-rate på C/10. Når C-raten ble økt til C/2 oppnådde prøven en utladningskapasitet på 124 mAh/g ved sykel 14. Med unntak av prøven med rent lignin som binder økte valsing både den mekaniske og den elektrokjemiske ytelsen til katodene.

Ettersom å bytte PVDF med lignin var en suksess ble løsemiddelet NMP forsøkt utbyttet med vann slik at ekstraksjonssteget kunne elimineres fra tørkeprosessen. Dette var hovedsakelig mislykket, og resulterte i tynne slurrier og ujevn tykkelse på katodebelegget. Problemene ble delvis løst ved å tilsette fosforsyre. Lavere pH i slurryen forbedret både slurry-egenskapene og adhesjonen til strømsamleren. Resultatene er lovende for framtidig forskning.

Et undermål for oppgaven var å optimalisere tørkeprosedyren for katodebelegget. Temperaturen og lufthastigheten ble variert i en spesiallaget konveksjonsovn. Høyere temperaturer ga kortere tørketid, og differansene var større ved lavere temperaturer. Ved å øke temperaturen fra 50 °C til 90 °C ble tørketiden redusert med 77%, mens en økning fra 90 °C til 150 °C reduserte tørketiden ytterligere 44%. Høyere lufthastigheter var hardere for prøvene, og redusert tørkehastighet fra 1,0 m/s til 0,5 m/s hadde større effekt på oppsprekkingen enn temperaturen. Lavere tørkehastighet resulterte i færre sprekker. EDS analyser av en standard-prøve tørket ved 50 °C viste jevn distribusjon av det aktive materialet, men noen agglomoreringer av CB. Bindemiddelet var jevnt distribuert gjennom katodebelegget. Ujevn beleggtykkelse og varierende geometri på belegget påvirket reproduserbarheten negativt, og dette var et gjennomgående problem i tørkeeksperimentene.

Forslag til framtidig arbeid er presentert, og fokuserer på å forbedre prosedyrene brukt i denne oppgaven samt videre arbeid for å erstatte NMP med vann. Videre arbeid bør gjøres for å optimalisere katodematerialet slik at det blir lettere å jobbe med.

Preface

First, we would like to thank our supervisor PhD Candidate Silje Nornes Bryntesen for excellent guidance in the laboratory, fast responses and funny conversations in our supervisor meetings. Her presence and optimistic approach have helped us produce many great results and to complete this thesis the way we aspired to.

We would also like to thank our supervisor Associate Professor Jacob Joseph Lamb for introducing us to Silje and her PhD project. He has provided us impeccable help in structuring the thesis and assistance with the English language.

We would also like to acknowledge NTNU for facilitating experiments during the Covid-19 pandemic. Especially, ENERSENSE and the LIBLab for providing a safe environment to execute our experimental work.

We wish to express gratitude towards MSc Student Armin Kahrom for assistance in providing results connected to the EDS analysis.

Contents

List of Figures

List of Tables

Chapter 1

Introduction

1.1 Background

As of March 2020, the average global temperature was 1.16°C above the 20th century average of 12.7°C [1]. Given the ongoing greenhouse gas (GHG) emissions, it is likely that the global temperature will exceed the Paris agreement goal of limiting global warming to an average temperature increase of 1.5 °C. The consequences of not maintaining the average temperature increase below the 1.5°C mark are increased climate extremes that can threaten the existence of our life on earth. Our dependence on the burning of fossil fuels contribute to excessively high amounts of GHGs [2]. The overall energy demand in the world is increasing, and in an effort to slow global warming, there is an ongoing shift from fossil fuels to renewable energy sources, like solar and wind [3]. This has led to the transition from combustion driven vehicles towards electric vehicles (EVs). Transitioning to EVs can potentially reduce CO_2 emissions by 125 million tons CO_2 per year in 2030, and up to 1.5 billion tons of CO_2 per year in 2050 [4].

The dominant battery technology for battery-driven EVs (BEVs) today are lithium-ion batteries (LIBs). Notably, BEVs represent a GHG-effective transition only if the electricity used to produce and drive the car is energy-effective, and originates from renewable energy sources [5]. Another important aspect to consider is that LIBs contain materials listed on EU's list of critical raw materials, such as lithium, cobalt and graphite. Currently, there are no viable substitutes, representing a high supply risk as EU is financially dependent on the supply of the materials [6]. Thus far, LIB production is predominantly led by Asian countries. With the expected growths in demands for LIBs, Europe aims to become less dependent on Asian supply and raw materials. Recently, this has led to several investments in the battery industry [7, 8]. In Norway, three battery production factories are planned to be in operation within the next few years, as well as recycling plants and several production facilities for materials used in LIBs [9]. Norwegian energy production, being 98% renewable, enables a more environmentally friendly battery production from cradle-to-grave [10]. Despite the potential of producing greener batteries from renewable energy sources in Norway, important work remains to enable a more energy-efficient production.

The production of a LIB is illustrated in Figure 1.1. First, the cathode active material, binder, conductive agent, solvent and additives are mixed and coated onto a current collector. This is followed by solvent removal through drying. The dried coating is compressed using a calendering process, then cut into the desired shape and assembled into battery cells. In a dry room free from moisture, the electrolyte is injected into the cell. Bryntesen *et al.* discussed that in a factory producing 1450 cells annually, the drying steps accounted for 82% of the total energy consumption and 19% with an annual production volume of 50 million cells. This is a large percentage, even though the total energy consumption percentage decreases with increased production volume. In the production of LIB components, the drying of the cathode is the most energy demanding and costly process [11].

During the slurry preparation, N-Methyl-2-pyrrolidone (NMP) is used to dissolve the polyvinylidene

fluoride (PVDF) binder. Once the slurry is mixed and spread onto the current collector, the slurry must be dried to remove the NMP. NMP is a toxic solvent and cannot be released into the atmosphere. Therefore, a significant amount of warm air is used in order to dry the electrode, as well as keeping the NMP vapour concentration in the air below its flammability level [12]. This makes the electrode drying an extensive and energy-demanding step within the production process of LIBs.

By exchanging NMP with water, the entire vapour recovery step can be significantly reduced; however, the PVDF binder currently used in LIB production is not soluble in water. An interesting alternative is to replace PVDF with lignin as the binder used in LIB production [11].

Lignin is a natural component extracted from biomass materials. It is a renewable, sustainable and abundant resource [13, 11]. With the battery industry establishment in Norway, the supply of lignin from Norway´s paper and pulp industry offers great potential for self-sufficiency with lignin-based LIBs. Introducing lignin as a binder and water as a solvent, together with Norway's access to renewable energy and lignin abundance, could lead to a more sustainable, environmentally friendly, and energy- and GHG-effective LIB production [11, 10, 13].

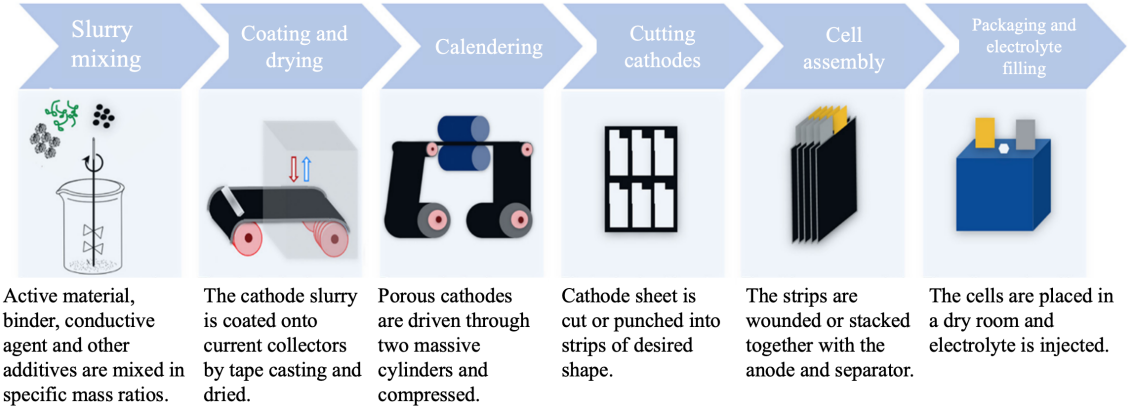

Figure 1.1: Lithium-ion battery cell production steps. From electrode manufacturing to cell assembly and packaging. Figure reused with permission from Bryntesen *et al.* [11].

1.2 Objectives

This BSc project aims to investigate a more energy- and GHG-effective production of the $LiNi_{1/3}Mn_{1/3}Co_{1/3}O_2$ (NMC111) cathode materials used in LIBs. The project coincides with ongoing research at NTNU aiming towards the establishment of a sustainable and ethically conscious battery industry in Norway, utilizing mineral resources and sustainable power sources in Scandinavia and surrounding countries. To reach this goal, the possibilities of exchanging the PVDF binder and the toxic NMP solvent with lignin and water, respectively, are investigated through a combination of literature studies and experimental work.

The approach to the experimental work is to change the process parameters of the slurry and see how this corresponds to changes in the cathode's electrochemical performance. The electrochemical performance is determined through galvanostatic cycling of coin half cells. The viscosity of a selection of slurries is determined by rheology measurements. Different samples are characterised in Energy Dispersive Spectroscopy (EDS) and Scanning Electron Microscopy (SEM) to analyse how the binder distribution and micro-structure correlates to electrode adhesion determined by a scratch test. To find a standard for comparison, the process parameters are first varied on slurries with PVDF binder and NMP solvent, followed by gradually exchanging PVDF with lignin, and NMP with water.

The thesis sub-goal is to dry NMC111 cathodes using a custom-made convection oven to decrease the drying time while maintaining or improving the current cathode quality. The drying time and weight reduction of the cathode coatings are logged continuously with varying air flows and

temperatures.

Chapter 2 gives an overview of the LIB system together with materials and their function. The chapter will go more in detail on PVDF and lignin as binders, NMP and water as solvents, as well as aspects connected to cathode drying. Chapter 3 presents the procedure of the experimental work, before the results will be presented and discussed in Chapter 4. Recommendations for further research will be discussed in Chapter 5, before concluding remarks are presented in Chapter 6.

1.3 Definitions and typical battery parameters

Cell voltage is determined by the potential difference between the electrodes. The voltage forces the electrons to move through a circuit. The *total cell voltage* is determined by the compatibility of the whole battery system. The *operating voltage*, also referred to as the open circuit potential (V_{OC}), is the potential when no power is drawn from, or applied to the battery [14].

Capacity corresponds to the amount of electrical charge the battery can accumulate during charge and deliver over time. It is usually specified in ampere hours (Ah). The *specific capacity* refers to the capacity relative to the mass of the active material (mAh/g) [15].

The *energy* stored in a battery is calculated as the product of the capacity and average voltage over time (Wh). Gravimetric and volumetric energy density refers to the energy per weight (Wh/kg) and per volume (Wh/l), respectively [15].

Power is the rate at which energy is transferred. Gravimetric and volumetric power density refers to the power available per mass unit (W/kg) and per volume (W/l), respectively [16].

The *Coulombic Efficiency (CE)* is the ratio of the charge put into the battery to the charge extracted from the battery over a cycle [17].

The *C-rate* represents a set constant current, which measures the rate of (dis-) charge the battery will provide or deliver during a specific time. For example, a fully charged battery with a capacity of 1 Ah discharged at 1C will fully discharge in 1 hour. If the C-rate was C/2, the same battery would take 2 hours to discharge [18].

Cycle life is calculated from the number of charge and discharge cycles the battery can handle. Usually if the discharge capacity decreases to less than 80% of its initial discharge capacity, the cell is considered to be at the end of its cycle life [19].

Self-discharge is caused by spontaneous reactions in the battery, leading to the battery discharging, despite not being in use [20].

Thermal runaway is caused by exothermal reactions inside the battery cell, resulting in fire or explosion. Thermal runaway can be triggered by internal short circuits and/or external influences [15].

Chapter 2

Theory

2.1 The fundamentals of batteries

A battery is an electrochemical cell that converts chemical energy to electrical energy through redox-reactions. A battery consists of two electrodes, a separator and an ion-conductive electrolyte. An external circuit connects the electrodes and allows current to flow. The separator isolates the electrodes electrically and physically from each other to avoid short-circuiting. The electrolyte allows ions to flow between the electrodes through the separator [21].

Primary batteries are non-rechargeable, while secondary batteries are rechargeable. A secondary battery has two operation modes, galvanic and electrolytic. Upon discharging, the galvanic cell convention occurs, characterised by spontaneous reactions. The oxidised and reduced electrodes are defined as the anode and cathode, respectively. Upon charging, the redox-reactions are reversed, making the positive electrode work as an anode and the negative electrode work as a cathode. This is characteristic for the electrolytic mode. By convention, the electrodes are named for their role in the galvanic mode [21]. The cathode and anode reaction is exemplified in Equation 2.1 and 2.2, respectively, where M represent a cathode metal and Z represent an anode material. The total cell reaction is exemplified in Equation 2.3 [21].

$$\text{Cathode reaction} \qquad M^+ + e^- \underset{\text{Charge}}{\overset{\text{Discharge}}{\rightleftharpoons}} M \tag{2.1}$$

$$\text{Anode reaction} \qquad Z \underset{\text{Charge}}{\overset{\text{Discharge}}{\rightleftharpoons}} Z^+ + e^- \tag{2.2}$$

$$\text{Total reaction} \qquad M \underset{\text{Charge}}{\overset{\text{Discharge}}{\rightleftharpoons}} Z \tag{2.3}$$

2.2 Lithium Ion battery system

The LIBs used in battery electric vehicles (BEVs) are secondary batteries and operate according to the principle described above. Figure 2.1 illustrates the basic principles and the configuration of a LIB in the state of discharging. It consists of an electrolyte and a membrane (i.e., separator) situated between two layered electrodes [15].

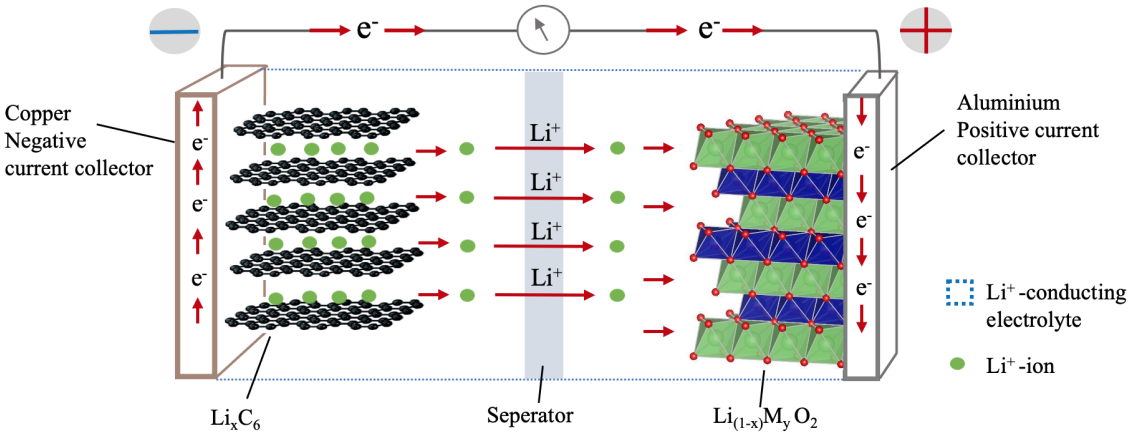

Figure 2.1: Schematic of a LIB showing the direction electrons and ions move in the state of discharge. Figure inspired by Leuthner *et al.*. [15].

The membrane is lithium-ion selective, porous and usually polymer-based. Typically, the electrolyte contains a solution of lithium salt in a mixture of organic solvent. In most cases, the anode is a graphite-based (Li_xC_6) material coated onto a current collector, often copper. The cathode is usually based on a transition metal (TM) oxide (e.g., $Li_{1-x}M_yO_z$, where M=Co, Mn, Ni), also referred to as the active material (AM). The AM is mixed with a polymer binder and an electrically conductive material (e.g., Carbon Black). The cathode is usually coated onto an Al-foil, which works as a current collector [15, 14].

During discharge, Li^+ deintercalates from the anode layers and releases one electron per Li^+ released. The current collector transfers electrical current (i.e., the released electrons) to the external load circuit. The Li^+ diffuses through the electrolyte and separator and intercalates into the cathode structure. The graphite anode is oxidised and the TMs in the cathode material are reduced. When charging, an applied external potential reverses the reactions. The Li^+ deintercalates from the cathode structure, migrates through the electrolyte and separator, and intercalates into the anode layers. The graphite anode is reduced, and the TMs in the cathode material are oxidised. The cathode is the primary provider of Li^+. The cathode and anode reactions are presented in Equation 2.4 and 2.5, respectively. The total cell reaction is presented in Equation 2.6 [15, 14].

$$\text{Cathode reaction} \qquad Li^+ + CoO_2 + e^- \underset{\text{Charge}}{\overset{\text{Discharge}}{\rightleftharpoons}} LiCo_2 \tag{2.4}$$

$$\text{Anode reaction} \qquad LiC_6 \underset{\text{Charge}}{\overset{\text{Discharge}}{\rightleftharpoons}} Li^+ + C_6 + e^- \tag{2.5}$$

$$\text{Total reaction} \qquad CoO_2 + LiC_6 \underset{\text{Charge}}{\overset{\text{Discharge}}{\rightleftharpoons}} LiCoO_2 + C_6 \tag{2.6}$$

2.2.1 The electrolyte

The electrolyte typically consists of a conductive lithium salt solution in a mixture with a non-aqueous organic solvent and various additives. According to Hartnig *et al.* [15], the electrolyte should strive to fulfill the requirements listed below:

- High ionic conductivity across a wide temperature range (-40°C to + 80°C) to ensure good flow of Li^+ between the electrodes.
- Sufficiently electrically insulated cell to force the electrical charge out into the external circuit.
- Cycling stability over several thousand cycles.

- Chemical and electrochemical compatibility with the other cell components in all operating conditions. It should be electrochemically stable up to potentials around 4 V, which is the general charging potential of current LIB technologies.
- In general, safety, environmental and economic concerns should be taken into account.

Lithium hexafluorophosphate ($LiPF_6$) is the most commercially used conductive salt. It has high conductivity in room temperature, is electrochemically stable up to 4.8 V vs. Li/Li^+ and has good compatibility towards other cell components. The $LiPF_6$ is extremely water sensitive, and if exposed to water the $LiPF_6$ breaks down and produces hydrofluoric acid (HF), which can deteriorate the cell.

Due to the highly oxidising anode and reductive cathode, using water as a solvent in the electrolyte would cause the development of unwanted hydrogen immediately. Therefore, the most suitable solvent materials are non-aqueous organic solvents, such as ethylene carbonate (EC), dimethyl carbonate (DMC), ethyl methyl carbonate (EMC) and diethyl carbonate (DEC) [15].

The flammability of the organic solvent and the water sensitivity of $LiPF_6$ can cause serious safety problems. Some of these problems may be solved by adding additives that are flame-retarding, remove the HF or promote a stronger SEI layer [15].

The electrochemical window and SEI film formation

As mentioned in Section 1.3, the total cell voltage is determined by the entire battery system. The electrolyte´s energy gap (E_g) between the lowest occupied molecular orbital (LOMO) and the highest occupied molecular orbital (HOMO) is referred to as the electrolyte´s electrochemical window (Figure 2.2). This window limits the battery cell voltage. If the anode (U_a) potential is above LUMO, and the potential of the cathode (U_c) is below HOMO, it will reduce the electrolyte on the anode and oxidise it on the cathode, respectively. During the first charging cycles, this can lead to the formation of a solid electrolyte interface (SEI) film on anode and cathode (Figure 2.2); which is significantly thicker on the anode than on the cathode [22, 14]. The SEI film increases the battery's internal resistance and consumes part of the Li^+, which leads to capacity and power loss. The SEI film's advantage is that it is electrically isolating, which prevents the electrodes from direct contact with the electrolyte and further secondary reactions [15].

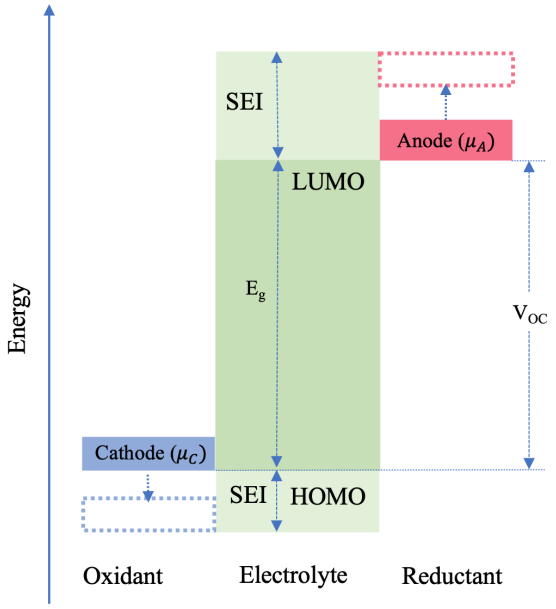

Figure 2.2: Schematic energy diagram of the energy relations of the electrolyte window (E_g), the electrochemical relations between the anode and cathode and the HOMO or LUMO of the electrolyte, to illustrate the formation of the SEI layer. Figure inspired by Liu *et al.* [14].

2.2.2 Anode materials

The main purpose of the anode is to store Li^+ in its structure. As of today, graphite is the most commonly used and commercialised anode material because of its low price, availability, high structural stability and low working potential versus Li/Li^+, ensuring a long cycling life [23]. As mentioned in section 2.2, the mechanism is based on intercalation/deintercalation of Li^+ in between the layered graphite structure (e.g., $6\,C(graphite) + Li^+ + e^- \longleftrightarrow LiC_6$). Due to challenges like the graphite material´s limited theoretical capacity of 373 mAh/g, researchers have started looking into materials with higher theoretical capacities, such as alloying and conversion-type materials [24].

In research using coin half-cells when evaluating a cathode material's performance, lithium metal is often used as an anode. Lithium is the lightest metal in the periodic table, has a high theoretical specific capacity (3860 mAh/g) and among the lowest electrochemical potential (-3.05V vs. SHE), which means that it oxidises easily and can achieve high open circuits potentials [25]. With the excessive supply of Li^+ in to the battery, lithium-metal as an anode will reduce sources of errors when evaluating a cathode material's performance [26].

2.2.3 Cathode - Active materials

The TM oxides are grouped from their crystal structure, where the most common are listed in Table 2.1 [27]. According to Akhilash *et al.* [27], the main tasks and requirements for the active material used in LIBs are:

- Insertion/extraction of Li^+ must be reversible
- Reaction between the AM and Li^+ should provide high free energy to obtain a high cell voltage.
- The AM should be a good electronic conductor, allowing easy addition and removal of electrons.
- The AM should be able to (de)intercalate the maximum number of Li^+ without much change in the structure.
- High diffusivity of Li^+ enables high power density.
- Cost effective and environment friendly.

Table 2.1: Properties, advantages and disadvantages of different cathode materials used in LIBs according to Blomgren [28] and Akhilash *et al.* [27]. $LiCoO_2$ (LCO), $LiNi_{1/3}Mn_{1/3}Co_{1/3}O_2$ (NMC111), $LiMn_2O_4$ (LMO), $LiFePO_4$ (LFP).

Cathode material	Specific capacity mAh/g		Average discharge voltage(V) vs.Li/Li^+	Advantages	Disadvantages
	Theoretical	Practical			
LCO	274	140	3.9	Commonly used, good cycle life, good energy	Moderate charged state thermal stability
NMC111	275	160	3.8	Good combination of properties (energy, power, cycle life and thermal stability	
LMO	200	148	4.0	Very good thermal stability, good power stability, inexpensive	Moderate cycle life, lower energy
LFP	170	150	3.5	Very good thermal stability and cycle life, good power capability	Special preparation conditions required, lower energy

Layered oxides

Layered oxides are one of the most used types of cathode materials in LIBs, where all have the same general formula $LiMO_2$, where M = TMs, and a similar chemical structure (isostructural) to the α-$NaFeO_2$-type. The structure belongs to the R-3m space group, which means that it has a unit cell with rhombohedral symmetry and mirror planes perpendicular to the c-axis.

The polyhedral plot in Figure 2.3 illustrates that the TMs and Li^+ are positioned in the octahedral sites where they are bonding to 6 oxygen atoms in total. The oxygen planes are stacked alternately and periodically (Li - O - TM – O – Li- O – TM- O) along the c-axis; this sequence is known as the "O3-type". A unit cell with n number of O^{2-} will form 2n tetrahedral and n octahedral sites. The oxygen bonded with the TM in the octahedral voids can be observed as a layer of MO_2. The diffusion of Li^+ takes place along the 2D interstitial space between the MO_2-layer (Figure 2.3), and the 2D diffusion channel gives a unique cycling mechanism [27, 29]. If all Li^+ is extracted from in-between the MO_2-layers, the structure may collapse. The layered oxide materials ability to keep stable when deintercalating a certain amount of Li^+ significantly impacts the cathode's practical capacity [27].

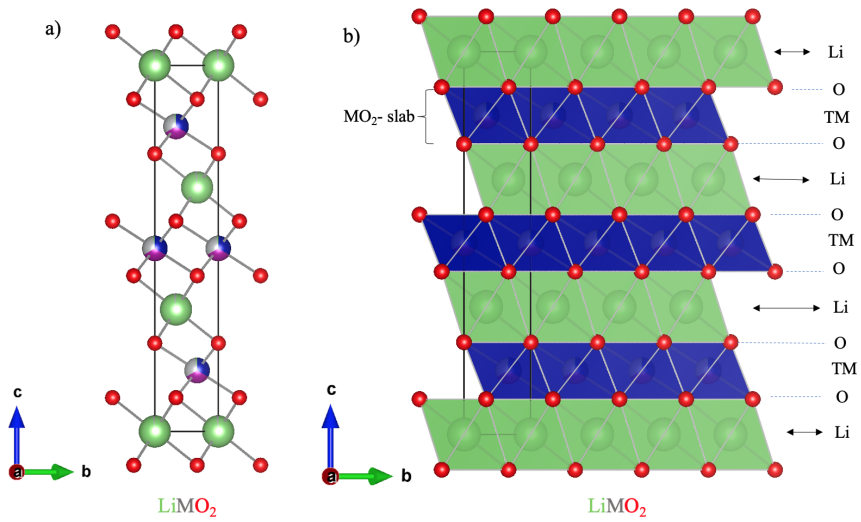

Figure 2.3: Unit cell of the layered NMC111 structure a) alternating and periodically stacking of NMC111 planes b) Made in VESTA based on Yin *et al.* [30].

LCO and NMC

The first generation of layered oxides used commercially was $LiCoO_2$(LCO). If all Li^+ were to be extracted from the structure, the material would have a theoretical capacity of 274 mAh/g; however, this would cause the collapse of the structure. To avoid structure collapse, LCO only uses about 50% of the available lithium in the structure (140 mAh/g). When lithium is deintercalated, the redox pair Co^{4+}/Co^{3+} is formed creating an average voltage of around 3.9 V (Table 2.1) [15]. Due to safety issues related to oxygen evolution, the charging is restricted to 4.2 V [27].

Cobalt is toxic by nature, and rare in the earth's crust, which also makes it expensive. According to Amnesty International it has also been connected to unethical mining [31]. As a result of LCOs disadvantages, the material has been modified and developed further in recent years. Research has focused on improving the specific capacity and voltage to increase the energy density and chemical substitution to increase the materials' stability. By partly substituting Co^{3+} with Mn^{+4} and Ni^{2+}, the $LiNiCoMnO_2$(NMC) material was proposed [30]. The evolution from LCO to NMC is illustrated in Figure 2.4. To balance the advantages and disadvantages of the TMs, the NMC material exists with various ratios of TMs, where the NMC111 material has been widely used [27].

NMC111 has a theoretical capacity of 275 mAh/g; however, for reasons of structure stability, only 66% of the available lithium is used. This leads to a practical capacity of 160 mAh/g, within the voltage window 2.5 - 4.4 V. When in a lithiated state the TMs have the charge Ni^{2+}, Mn^{4+} and Co^{3+} [15]. Both Ni and Co contribute with charge carriers when oxidised, which increases the electrical conductivity and overall electrochemical performance of the battery. Mn^{4+} does not contribute with charge carriers; however, it helps to stabilise the structure together with Ni. Disadvantages of the NMC111 material is the risk of phase transformations in a delithiated state and the risk of O_2 gas evolution if the charging voltage exceeds the stability window of the electrolyte. It also has a lower discharge voltage than LCO [27].

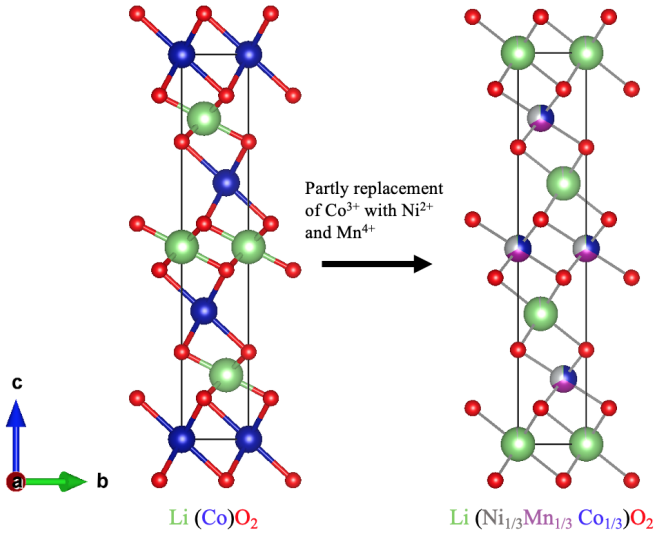

Figure 2.4: Illustration of the evolution from LCO to the NMC material. Made in VESTA inspired by Yin *et al.* [30] and Akhilash *et al.* [27].

2.3 Binder

The binder is typically chemically inert, and does not play a direct role in the electrochemical performance of the electrode. However, it is a functional additive, and if the binder performs sub-optimally, it would be detrimental to the electrode and by extension the LIB. As the binder is the cohesive agent in the electrode it needs to form strong cohesion both in the electrode material, and between the electrode material and the current collector. The mechanical properties of the electrode are mainly defined by the amount, distribution and molecular weight (MW) of the binder throughout the electrode [11, 32] . A decrease in the binder chain length and a lowered MW may cause a lower adhesion strength [11]. The binder should be compatible with the electrolyte, meaning that it needs to be insoluble in the electrolyte and experience minimal swelling. It also needs to have a high thermal and electrochemical stability, with minimal detrimental effects on electron- and ion-transport in the composite. The ideal binder would live up to all these demands while still having a low environmental impact, and low cost [11].

PVDF

Polyvinylidene fluoride (PVDF) is a highly inert thermoplastic [13] with a simple chemical structure, which can be seen in Figure 2.5. It is often used as a binder for cathode materials as it has good electrochemical stability, and high adhesion to electrode materials and current collectors [33]. As a fluoropolymer it is soluble in few solvents, which are typically expensive, toxic and/or flammable (e.g., NMP). This makes electrodes with this binder harder to recycle, as they would need thermal treatments to eliminate the PVDF. Thermal treatments raise new environmental concerns, as fluoropolymers decomposing in nitrogen (air) produce extremely toxic gases known to affect the ozone-layer [13].

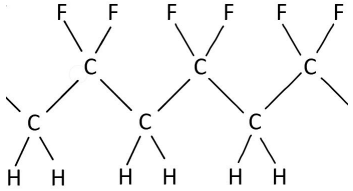

Figure 2.5: Structural formula of PVDF

Lignin

Lignin is a component of lignocellulosic biomass material - *in layman's terms: plant dry matter*, a renewable, sustainable and abundant resource. It is a structural material, with low price and density, high hardness, and resistance to heat, chemicals, friction and humidity [34]. Lignin is a macro-molecule composed of p-courmaryl alcohol (I); coniferyl alcohol (II); and sinapyl - alcohol (III) as illustrated in Figure 2.6 [35]. With the correct pre-treatment, lignin is water-soluble [36]. As of yet, the exploration of lignin as a binder material for LIB is limited [34].

Lu *et al.* [35] explored lignin as a binder material for $LiFePO_4$ cathodes in LIBs. They dissolved lignin in acetone and added 5% PEG to improve its elasticity to electrodes. The lignin was leached prior to use in order to remove smaller lignin chains, as they otherwise might leak into the electrolyte. Batteries made with unleached lignin as cathode binder and water as solvent with the composition 82 wt% $LiFePO_4$, 9 wt% Carbon Black and 9 wt% lignin showed a drastic decrease in specific capacity after the first six cycles. Using leached lignin as the binder, the resulting electrodes showed relatively high specific capacities of 117 mAh/g (C/10) and 148 mAh/g (1C) during cycle 4, and the binder had good stability. Calendering of the cathodes did not lead to enhanced performance, but rather worsened it as polarisation increased, and the specific capacitance lowered [35].

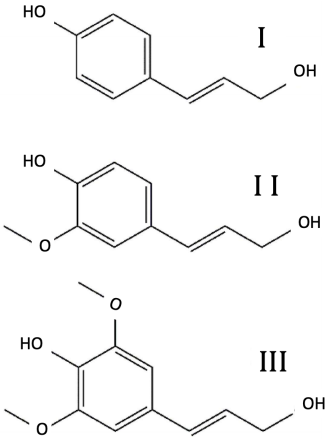

Figure 2.6: Structural building blocks of lignin: p-courmaryl alcohol (I); coniferyl alcohol (II); and sinapyl - alcohol (III) [35].

2.4 Solvents

A solvent is used to combine the cathode materials in a slurry as to facilitate coating on the current collector. Some of the most important factors to evaluate when comparing solvents are their impacts on the rheology and viscosity of the coating, the solubility of the binder, the evaporation rate and vapor pressure, the cost and environmental impact of the solvent, the dispersion stability and surface tension, as well as the flammability limit and safety [11]. Table 2.2 presents a comparison of the different solvent properties of NMP and water.

Table 2.2: Various solvent properties of NMP and water [11, 37, 38, 39]

Solvent	**Boiling temperature** [°C]	**Vapor pressure** [Pa] @ 20 °C	**Surface tension** [mN/m] @ 20 °C	**Flammable**	**Toxic**
Water	100	2339	72.80	No	No
N-methyl-2-pyrrolidone (NMP)	202	32	40.79	Yes	Yes

2.4.1 NMP

N-methyl-2-pyrrolidone (NMP) is an organic and toxic solvent with a high chemical and thermal stability. NMP has a good solvency for a wide range of organic and inorganic compounds, making it suitable to dissolve polymeric binders such as PVDF [11, 40]. The chemical structure of NMP is shown in Figure 2.7. The low surface tension of NMP makes it ideal for coating, as it will properly wet the current collector. NMC is not soluble in NMP, and as such Li-leaching is not an issue [41]. Using NMP as solvent in cathodes will also secure proper wetting of the hydrophobic CB, therefore NMP-based suspensions generally have less problems related to CB agglomerations compared to water-based suspensions [11].

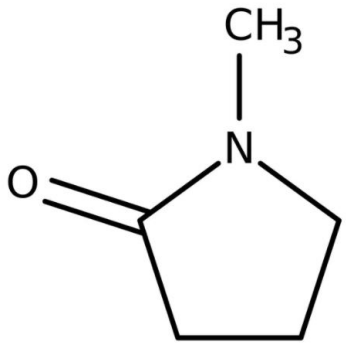

Figure 2.7: Chemical structure of *N*-methyl-2-pyrrolidone (NMP) [42].

NMP has a high boiling point, and low vapour pressure, demanding a lot of energy in drying [41]. Due to NMPs flammability, toxicity and risk of potential health hazards, the production line has to take extensive safety measures to prevent fire and explosion [11]. Because it is a volatile organic compound (VOC), it needs to be extracted from the air after drying, adding to the cost and energy consumption associated with its use. This demands a significant expense that involves multiple distillation towers, condensers, and significant amounts of energy [43]. According to Ahmed *et al.* [12] the drying and recovery process uses $\sim$ 10 kWh / kg NMP, and the energy use is estimated to be roughly 45 times greater than the energy required to vaporise NMP [12, 41].

2.4.2 Water

Water presents several advantages as a solvent in terms of both cost and environmental friendliness. It has lower boiling temperature and higher vapor pressure than NMP, but the latent heat of vaporization is about 4 times higher. This results in similar energy consumption for the drying process, but allows for faster drying when using water. As the water can be released into the atmosphere, the recovery step for NMP-processing is eliminated. Therefore, the total energy-use related to drying is lower when using water as solvent compared to NMP [13]. Despite this, aqueous slurry processing does present several challenges, with some of the most pressing challenges being:

- Replacing the PVDF binder with a water-soluble binder [44]
- Controlling particle agglomorations in the slurry [41]
- Mitigating lithium leaching from the AM [41]
- Mitigating corrosion of the current collector [45]

Water-based slurries also have a higher surface tension, making it harder to properly wet the current collector during electrode coating. In addition, waterborne binders generally have a lower adhesion strength between the electrode and the current collector compared to PVDF, affecting

cycle life [41]. Hawley *et al.* [46] discussed that water-based slurries in general can achieve higher solid loadings (60wt%) than NMP-based slurries (45wt%) due to a smaller viscosity contribution from the binder.

Particle agglomerations caused by attractive interactions between colloidal particles can result in inhomogeneous distributions of electrode components; therefore, poor electrochemical performance. This can be handled by use of dispersants and thickening agents, optimal mixing protocols and optimization of the coating parameters. If the drying protocol is not optimized, aqueous slurries are more likely to form cracks [41]. The high surface tension of water exacerbates electrode cracking during drying. This can be circumvented by mixing the water solvent with a solvent that has a lower surface tension [47]. As waterborne binders typically are more hydrophilic than PVDF they are also more prone to water adsorption, and special care needs to be taken to avoid significant water content in the LIBs, as it will affect the long term performance. This has been achieved in industrial production through a secondary drying protocol [41].

Lastly, the lithium in NMC is soluble in water, leading Li to leach out of the NMC-particles when they are in contact with water. The amount of leached Li increases as a function of increased exposure time and increased Ni-content in the AM [41]. Leached Li forms lithium hydroxide ($LiOH \cdot H_2O$) and insoluble carbonates (Li_2CO_3) in the slurry, and the depletion of lithium ions from the cathode leads to a noticeable loss of inventory, reducing the capacity of the LIB (Figure 2.8). A side-effect of this is increased pH in the slurry, leading to corrosion of the Al-foil current collector. The corrosion has a negative effect on the electrode homogeneity and the cell properties (e.g., specific capacity) [45].

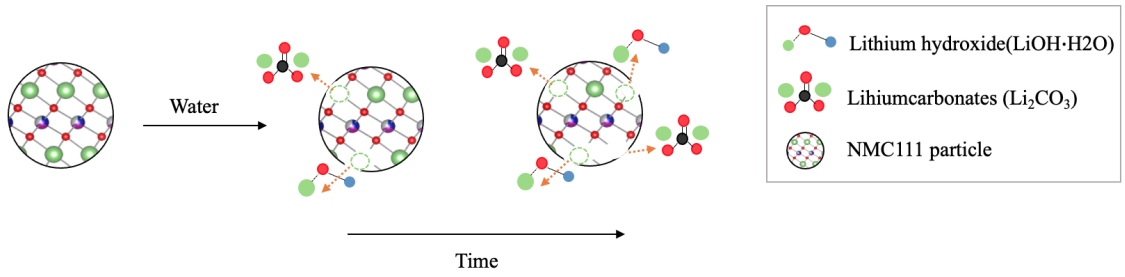

Figure 2.8: Leaching of lithium as a function of time and the formation of lithium hydroxide and insolvable carbonates, when using water as a solvent.

pH-control in water-based slurries

In order to avoid corrosion of the Al-foil current collector, the pH of the slurry needs to be within the stability window of pH 4.5-8.5 for the Al-foil. To lower the pH, acid can be added to the slurry. Bauer *et al.* [45] found the optimal pH window to be in the range of 9-10, as lower pH values caused significant leaching of Li from the AM. In addition, at the lower pH the viscosity and the resistance in the electrode increased, while the adhesion between the electrode material and the current collector reduced significantly. The rise of viscosity and resistance was presumed to be caused by more isolated CB fragments due to the high dispersing potential of the acid. In the adhesion-determining interface between the current collector and the electrode material, acid presumably accumulated causing the drop in adhesion. While moderate addition of acid to the pH range 9-10 was not enough to completely avoid corrosion of the Al-foil, it seemed to be the best compromise for ideal electrode and cell properties (e.g., specific capacity) [45]. Kazzazi *et al.* [48] found that independent of binder utilized, the addition of phosphoric acid (PA) led to a reduced amount of cracks and Al corrosion when the pH was lowered from 9.9 to 7.7.

Li_3PO_4-coating

Previous studies on H_3PO_4(PA) treatment of NMC111 when using PVDF as a binder and NMP as a solvent observed that the PA treatment lead to the formation of a Li_3PO_4-coating on the particle surface. This eliminated or minimised Li-residues (e.g., LiOH, Li_2O and Li_2CO_3) on the particle surface as shown in Equation 2.7, 2.8 and 2.9 [49].

$$3\,Li_2O + 2\,H_3PO_4 \Rightarrow {}_2Li_3PO_4 + 3\,H_2O \tag{2.7}$$

$$3\,LiOH + H_3PO_4 \Rightarrow Li_3PO_4 + 3\,H_2O \tag{2.8}$$

$$3\,Li_2CO_3 + 2\,H_3PO_4 \Rightarrow {}_2Li_3PO_4 + 3\,CO_2 + 3\,H_2O \tag{2.9}$$

The elimination of Li residues from the NMC surface prevents their oxidative decomposition and generation of gases during cycling at high voltages, thus improving cycling stability. The formation of the Li_3PO_4 coating scavenges HF and residual water in the electrolyte, suppressing HF propagation during charge/discharge cycles, further improving cycling stability. At the same time, the Li_3PO_4 coating forms a physical barrier preventing direct contact between the electrolyte and reactive transition metal ions in high oxidation states, suppressing side reactions between the electrolyte and NMC both during soaking and the first charge. Sahni *et al.* [49] showed a significant enhancement in the first discharge capacity, with a 36% increase in specific discharge capacity for NMC111 during the first discharge after PA treatment. This improvement is presumed to be due to the preservation of AM on the NMC surface, combined with enhanced Li^+ transport allowing increased Li^+ intercalation/de-intercalation at the electrode/electrolyte interface during charging/discharging. The enhancement may also be attributed to eliminating insulating Li residues at the NMC surface, and the Li-conductive Li_3PO_4 layer at the NMC surface [49]. Table 2.3 presents different studies and their findings on how acid treatment has been used to solve various problems.

Table 2.3: Challenges related to acid treatment and Li_3PO_4-coating, with possible solutions.

Problem	Findings	Reference
The addition of acid (HAc) to aqueous slurries has negative effects on slurry rheology, electrode conductivity and adhesion.	Highest cell capacities were obtained at a moderate reduction to pH 9-10, the addition of HAc accelerated cell degradation.	[45]
Corrosion of Al current collector with aqueous NCA slurries.	Addition of polyacrylic acid (PAA) lowered and stabilized slurry pH. Carboxyl groups were absorbed on NCA surface, creating a coating that averted excessive Li and Al dissolution and provided electrostatic stability, rejecting AM particle agglomeration.	[44]
Proving the generality of PA treatment enhancing the cycling stability of NMC cathodes made with NMP solvent and PVDF binder.	PA treatment resulted in the formation of a Li_3PO_4-coating on the surface of NMC particle. This improved rate capabilities, increased the specific capacity of the first discharge, and improved cycling stability for cathodes of NMC.	[49]
The performance of cathode electrodes based on TM oxides decaying with aqueous processing.	Adding small amounts of PA to the slurry during aqueous processing yields outstanding electrochemical performance for NMC111 cathodes in LIBs.	[50]

2.5 Drying

Drying is an energy intensive process, accounting for 12% of the total energy consumption in the world. Due to the geographical location of the bulk of the industry, the most common energy sources in industrial dryers include natural gas, propane, and other fossil fuels. Shortage of these energy sources have led drying industries and researchers to look for ways to reduce energy consumption from the drying process [51]. The result of reduced drying time is reduced energy consumption, which will benefit the environment and potentially increase production capacity.

Drying is a mass transfer process consisting of the removal of solvent by evaporation. The most common procedure is drying by convection, where a gas stream (e.g., air) applies the heat and carries the solvent as a vapour [52]. Other possibilities are vacuum drying, where heat is supplied by conduction or radiation. The basis of radiation as a heating mechanism is that all materials can radiate and receive heat in the form of electromagnetic radiation. The low pressure and temperature ensures a gentle drying of sensitive materials. Vacuum drying is a great solution when drying toxic materials as the vapour is conserved in a safe environment inside the chamber [53].

2.5.1 Convection drying

The industrial drying method for LIBs is usually performed by convection. The setup of the custom-made lab-scale convection oven used in this project is presented in Figure 2.9. Convection is the transfer of heat from one place to another using a flow of liquid or gas between these places. Convection problems arise when a heat flow crosses a phase boundary (i.e., convection takes place on the sample surface). A distinction is made between free and forced convection, where forced convection is when the liquid or gas phase is circulated due to a pump or fan. If an oven dries with forced convection, the Reynolds number can be calculated to assess if the flow is laminar, transitioning, or turbulent from Equation 2.10 [54].

$$Re = \frac{\rho \cdot v \cdot D}{\mu} \tag{2.10}$$

Where ρ is the density of the fluid, v is the velocity of the fluid flow, μ is the viscosity of the fluid and D is the diameter of the pipe the fluid flows through.

In the laminar flow area the fluid flows in parallel layers with no lateral mixing between the layers, and Re < 2000. In turbulent flow area, the fluid flows unsystematic with lateral mixing between the layers. This usually means a heterogeneous fluid in term of temperature and direction in the fluid flow, where Re > 3000. The transitioning area is a combination of both and it is difficult to properly determine what sort of airflow is occurring. In this area, $2000 \leq$ Re ≤ 3000 [54, 55].

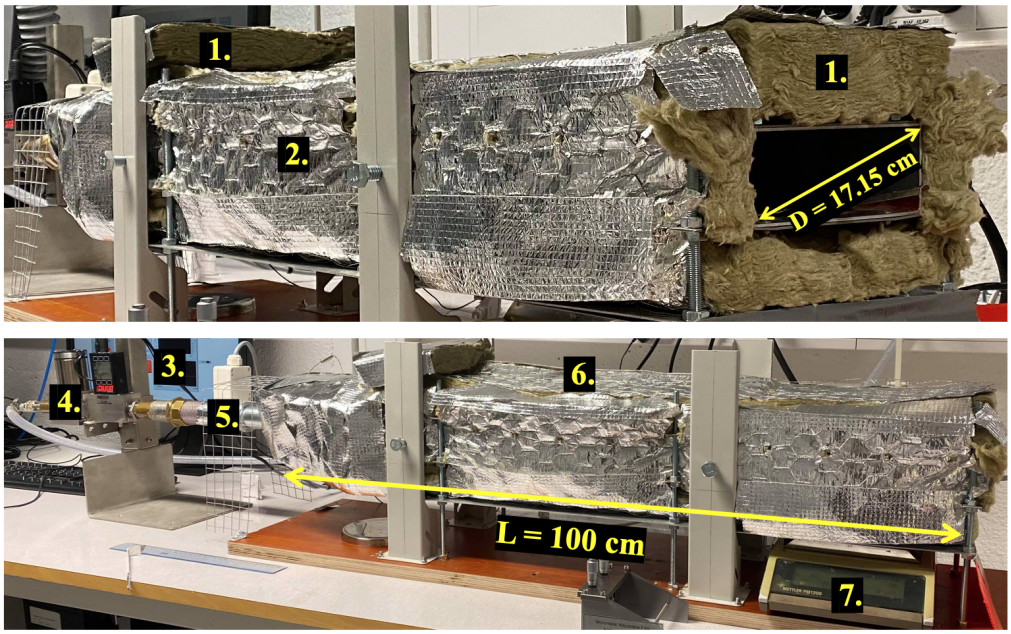

Figure 2.9: Set up of a custom-made lab-scale convection oven, where 1. Insulation, 2. Al-foil and Al-tape to secure insulation, 3. Computer program to log time, temperature and weight, 4. Air nozzle, 5. Heater and protective grid, 6. Thermometers, 7. Weight.

2.5.2 Electrode drying

Electrode drying is a complex process since it involves mass and heat transfer in the solid, liquid and gas phases. Figure 2.10 shows that there are three competing physical processes during the electrode drying – evaporation of the solvent (a, b), diffusion of the binder (c), and sedimentation of the particles (d) [46]. It is preferable with an even distribution of particles in the electrode. A dry electrode is important as NMP and water will pollute the LIB, resulting in a reduced battery capacity.

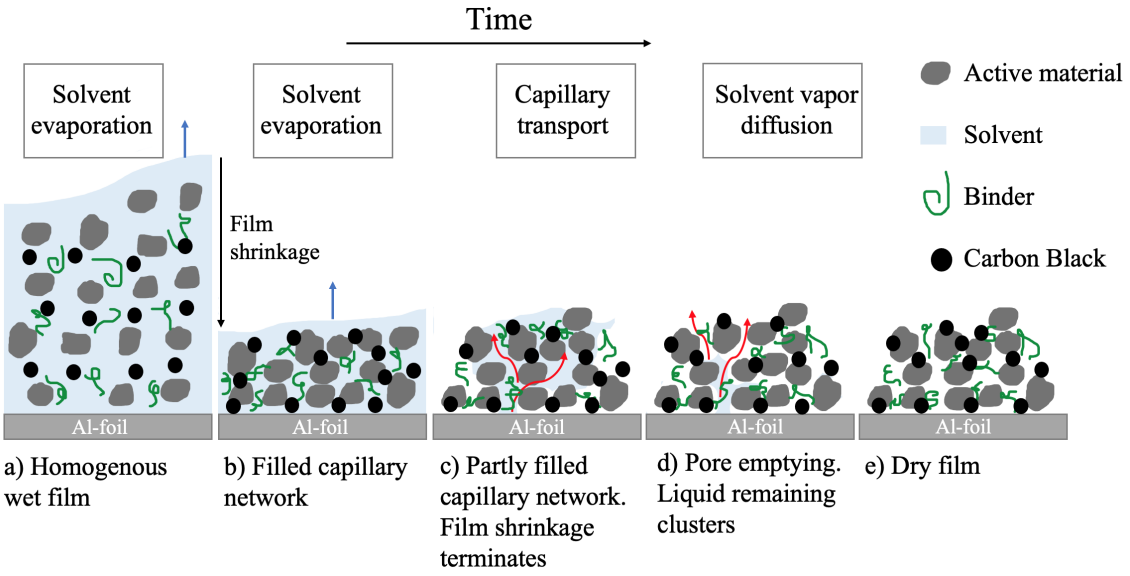

Figure 2.10: Drying mechanism within a cathode during drying. The cathode consists of carbon black, active material, polymer binder, and solvent and is coated onto an Al-foil. Figure inspired by Bryntesen *et al.* [11].

A way to measure drying is to measure the reduction of moisture content (MC) in a sample over time. MC is reported on either a wet or a dry basis; however, MC is often reported in the literature only as a percentage or factor, without any indication of which method used. The Equation 2.11 for wet basis is given below [56].

$$MC_{wet} = \frac{Solvent\ weight - evaporated\ weight}{Solvent\ weight} \tag{2.11}$$

The drying process can be divided into three phases, which can be observed on the drying curve in Figure 2.11. In the first phase, the solvent is heated and little solvent is removed. When the solvent reaches evaporation temperature, the drying moves into the second phase where constant solvent reduction can be observed as a constant drying rate. This is the phase where the bulk of the solvent evaporates. As the solvent is emptied from larger capillary pores, the remaining solvent is trapped in the structure, and the solvent transport out of the structure slows down. The drying rate reaches a new, lower constant drying rate until all the solvent is removed. This is the third drying phase [57].

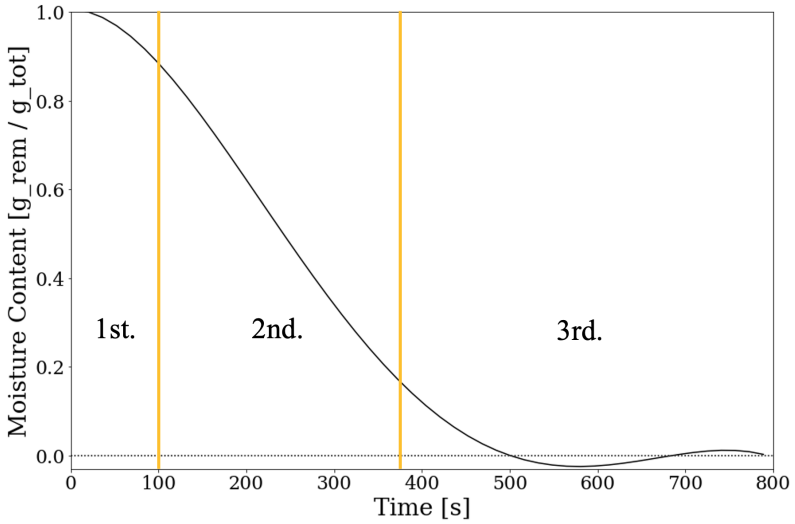

Figure 2.11: Characteristic drying curve divided into the three drying phases, where moisture content is plotted as a function of time.

The usage of toxic NMP as solvent makes it necessary for industries to use a large amount of heated air in the drying process. This is to keep the NMP vapour concentration far below the flammability level of 1.1 % at 140 °C [12]. NMP cannot be released into the atmosphere, therefore the drying air needs to be captured and cleaned in an energy demanding process. The re-use and recovery of NMP leads to a greater cost reduction in the production process. While considering energy aspects of drying, Bryntesen *et al.* [11] discussed the air-flow and temperature of the drying chamber should be at a minimum value at all times for optimal energy efficiency without compromising the coating structure.

Binder migration

A schematic of the drying process in the electrode material is displayed in Figure 2.10. The distribution of slurry-components are homogeneous throughout the film before the drying process starts. At the start of the drying process the solvent evaporates and the film shrinks. The solvent evaporates from the film surface, and when the film reaches its final porosity, some solvent is still trapped within the capillary network. The drying rate remains constant as larger capillary pores are emptied, with solvent moving towards the film surface through capillary transport. Additionally, the binder and carbon black is also dragged towards the film surface with the solvent [58].

Once larger pores are emptied, smaller liquid clusters may remain in the structure unavailable for capillary transport. This liquid needs to evaporate within the porous structure, and further energy is required to overcome the additional transport resistance, leading to a reduced drying rate at the end of the drying process. After the initial drop in the drying rate, the film will reach a lower constant drying rate until the solvent has completely evaporated. This is especially prominent in thicker electrodes [58].

Kumberg *et al.*[58] have observed a correlation between drying time, cell performance and electrode adhesion to the substrate, and their results indicate that high drying rates lead to a depletion of binder at the interface between the current collector and the active material (bottom) as shown in Figure 2.12. The higher drying rate leaves less time for back-diffusion of binder, which is driven by the developing binder concentration gradient. Because of the potential for back-diffusion, higher drying temperatures at certain drying rates are beneficial for micro-structure homogeneity. Longer drying times will also give more time for back-diffusion. Thicker electrodes will need more time for it, as the binder has to move through longer pathways in comparison to thin electrodes [58].

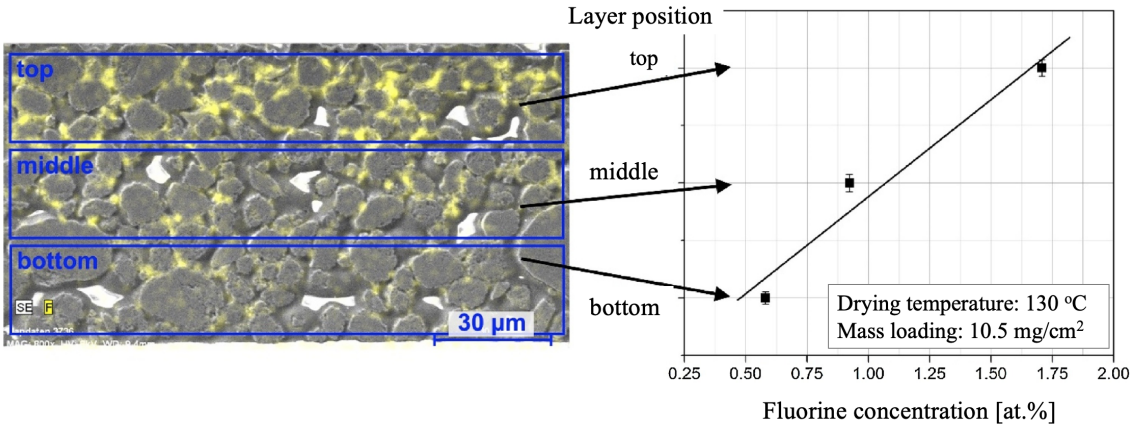

Figure 2.12: The left image shows the binder (yellow - fluorine) distribution along an electrode coating cross-section. The image to the right shows an increasing binder concentration towards the coating surface [59].

Cracking

Cracking is caused by stress from capillary forces during drying [47]. Cracking strongly depends on particle size distribution, additives, surface tension and rheology [58]. The high surface tension of aqueous slurries can result in an accumulation of capillary stresses during drying, leading to increased cracking of the electrode material [11]. Cracking results in poor particle-to-particle connection, leading to poor electrical conductivity. Fragmentation can result in loss of active material from the cathode migrating into the electrolyte. Cracking also increases side reactions during cycling, as the cracks expose the AM and generate new sites for surface phase transformation (SEI transformation), accelerating cell degradation [60]. An example of a cracked electrode surface is presented in Figure 2.13.

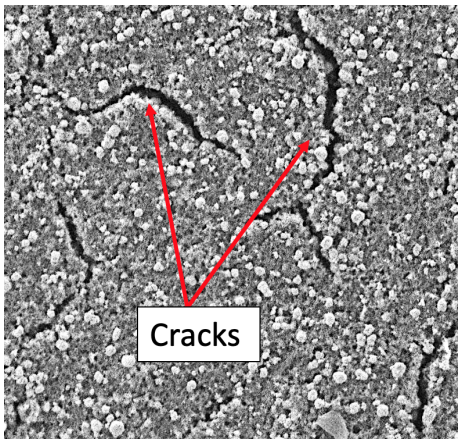

Figure 2.13: SEM image presenting a cracked electrode surface.

2.6 Calendering

Calendering is a compaction process where a constant, compressing load is applied to electrodes after drying to control and decrease the electrode materials final thickness and porosity [11]. Calendering improves particle-to-particle contact in the electrode material and increases the adhesion between the electrode and current collector. It also improves the volumetric energy density, as the same amount of AM is compacted in a smaller space post-calendering. However, the porosity decrease of the electrode does reduce the specific area of the electrode and increases the tortuosity, which may hinder Li migration within the electrode. Because of this, it is important to control the density to obtain the best electrode performance. Zheng *et al.* [61] found the optimal performance of NMC111 cathodes with PVDF binder to be at a porosity around 30 - 40%. The true density of the electrode can be calculated from Equation 2.12, the packing density from Equation 2.13 and the final porosity from Equation 2.14.

$$Electrode\,true\,density = \frac{Materials\,density}{Materials\,wt\%} \tag{2.12}$$

$$Packing\,density = \frac{Electrode\,weight\,loading}{Electrode\,thickness} \tag{2.13}$$

$$Porosity = 1 - \frac{Packing\,density}{Electrode\,true\,density} \tag{2.14}$$

2.7 Characterization techniques

2.7.1 Rheology measurments

Viscosity is a measure of friction between the molecules in the fluid when it is exposed to shear forces [21]. A cathode slurry is viscoelastic, which means that it has both viscous and elastic properties when deformed. The viscous properties allow the slurry to change shape when exposed to stress, and the elastic properties will make the slurry return to its original shape when the stress is released. A viscous slurry with liquid-like properties is easier to coat than an elastic slurry with gel-like properties. When coating the slurry onto an current collector, a shear rate is applied to the slurry from the doctor blade. Therefore, it is essential to know the viscosity of the slurry at the respective shear rate to ensure optimal coating [43].

By the use of a rheometer, the viscosity can be measured by applying an increasing shear rate (1/s) from a steady-state flow mode. If the viscosity decreases with an increasing shear rate, the slurry is showing a shear thinning behaviour. Storage modulus (G´) and loss modulus (G´´) can be measured with an increasing angular frequency from an oscillatory mode. Storage- and loss-modulus relates to the elastic and viscous portion of the slurry, respectively. If the storage modulus dominates over the loss modulus, it indicates that the slurry has gel-like rather then liquid-like properties [43]. Al-Shroofy *et al.* [43] tested the viscosity on samples with increasing amounts of NMP solvent to investigate how this affected the slurry properties. The study showed that decreasing amounts of NMP increased the viscosity.

The viscosity, loss modulus and storage modulus may help understand the interaction between the slurry's components, and find the correct viscosity before the slurry is coated onto the current collector [43].

2.7.2 Scratch test

A scratch test can give an indication of the adhesion between the electrode film and current collector, and the cohesion between the particles in the electrode film. Visual inspection of the scratch tracks can be used to evaluate the degree of delamination between the current collector and the electrode coating; therefore, allowing the observation of its resistance against scratch damage [62]. The scratch test is executed by applying a vertical progressive force (mN) to the coating.

2.7.3 Scanning Electron Microscopy

A scanning electron microscope (SEM) is used to study the micro-structure and topography of a material sample. In an electric field, a thin electron beam (referred to as the primary electron beam) is focused towards the respective sample surface. The beam creates an interaction volume beneath the sample's surface, where various signals are produced at different depths [63], as illustrated in Figure 2.14.

The signal from the secondary electrons (SE) are electrons knocked out from the atoms inner shell by the primary electron beam. SE are emitted from a depth of 0 - 100 nm and provide information on the topography of the sample. From 100 - 1000 nm depth, back-scattered electrons (BSE) are created (Figure 2.14). The primary electron's attraction to the positive atom core causes part of the primary electrons to deflect and emit out from the sample. The BSE beam provides information on heavy and light phases (termed the atomic number contrast or Z-contrast). BSE beams may also provide information on the topography of the sample, but not with the same quality as SE [64].

Detectors count electrons from the emitted SE and BSE, and convert them to an electrical signal. The more electrons sent out from one area, the stronger the signal. Heavy elements back-scatter electrons stronger than light elements, and therefore appears brighter on the image. After scanning the entire sample area, pixels with different shades of grey create contrast, which forms a picture of the micro-structure of the sample [64].

The sample needs to withstand vacuum, be dry and be electrically conductive. A thin metallic surface coating (e.g., gold) must be applied to non-conductive materials [63].

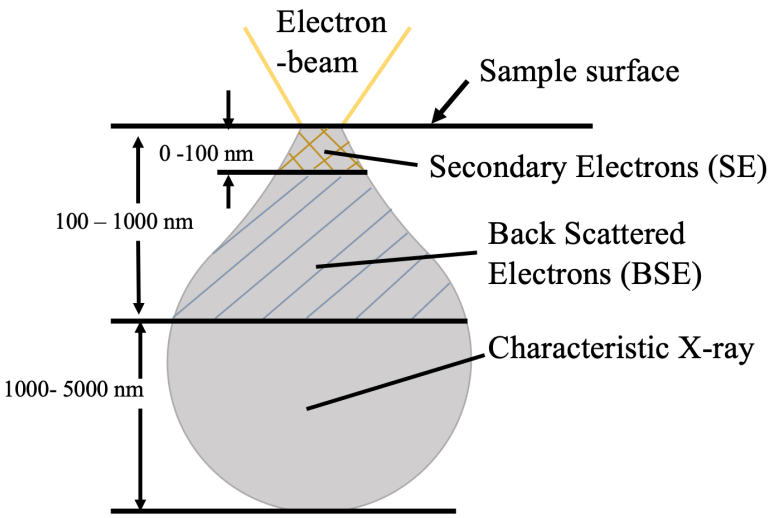

Figure 2.14: Interaction volume beneath the sample surface where BSE, SE and X-rays are created.

2.7.4 Energy Dispersive Spectroscopy

In Energy Dispersive Spectroscopy (EDS), the energy of the X-rays are measured and provides information about the chemical composition of the specimen. By scanning the entire surface of the specimen, and assigning different elements various colours, it is possible to map the composition. If different elements emit X-rays with similar energy, lines in the EDS spectra may overlap each other resulting in imprecise results. EDS methods are often integrated into the SEM [64]. X-rays are created from 1000 - 5000 nm beneath the sample surface (Figure 2.14). At the same time as secondary electrons are created, electrons from higher energy levels decelerate, and the loss of energy emits as photons (X-rays). The X-rays have a characteristic wavelength in particular to the specimen elements.

2.7.5 Electrochemical characterisation

To evaluate the electrochemical performance of the electrode material, the LIB is usually charged and discharged. Charging and discharging constitutes one cycle, whereas a half-cycle is referred to as one (dis)charging step [19].

Cycling tests can be carried out through several methods. Galvanostatic cycling and cyclic voltammetry (CV) are often used, where both methods provide information about capacity, but under different circumstances. A constant current (C-rate) is applied during galvanostatic cycling, whereas a constant potential sweep rate (V/s) is used during CV cycling. The galvanostatic cycling method is often used during discharging and the first charging cycles because it allows more time for the electrochemical processes to reach completion. For the subsequently charging half-cycles, CV may be applied. When forcing a constant potential, the current can increase and exceed the kinetic limit preventing capacity from being accessed [19]. The high current can also lead to a collapse of the electrode structure. Therefore, a lower and more controlled charging current is preferable during the first cycles. The advantage of CV is that it provides rate information, and circumvents overvoltage and irreversible side reactions [19].

To avoid over (dis)charging, the cycling test must be terminated after a certain amount of time or potential. If over (dis)charged, the (dis)charge will continue past the point where all AM has been utilised. The over (dis)charge may cause a breakdown of other cell components since these only are stable within a certain potential window. The electrochemical performance of the electrode can be presented in a charge/discharge plot, as illustrated in Figure 2.15, where the potential (V

vs Li/Li^+) is plotted as a function of specific capacity (mAh/g) [19].

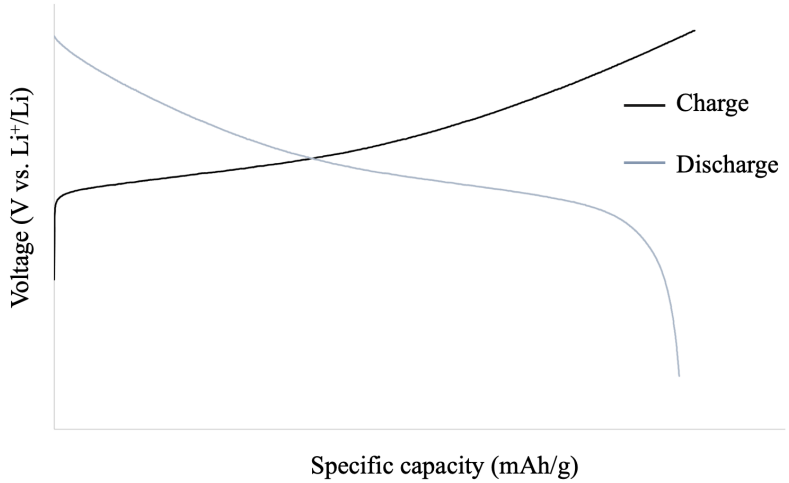

Figure 2.15: Illustration of a charge/discharge plot where voltage (V) vs Li/Li^+ is plotted as a function of specific capacity (mAh/g).

Chapter 3

Methods

The following sections describe the experimental methods used in the research of this thesis. They are divided into 5 main parts: Slurry preparation, coin cell assembly, calendering, characterisation methods and convection drying experiments.

3.1 Slurry preparation

An abbreviated notation is used to present the formulation of the cathode composition. To exemplify, 85:10:5 indicates that the cathode consist of 85 wt% active material, 10 wt% conductive material and 5 wt% binder. The specific materials used are given in Table 3.1. PVDF is dissolved in NMP in a 1:20 wt% ratio before being introduced to the cathode slurry. To create a cathode material slurry, beginning with the active material (NMC111) allowed the suitable amounts of the other chemicals to be calculated using the theoretical mass Equation 3.1.

The mixing sequence started with adding the powders NMC111 and CB in a small container. The PVDF:NMP solution was then added, and at last, extra NMP was added to reach the desired powder:solvent ratio. The amount to be added can be calculated using Equation 3.2.

In the slurry mixing procedure, the amount of each chemical is usually given as a mass ratio (wt%), where the recipe can be calculated using Equation 3.1 and 3.2.

$$Theoretical\ mass = \frac{Weighed\ amount}{Wt\%} \cdot 100 \tag{3.1}$$

$$Extra\ Solvent = (Solvent\ ratio \cdot theoretical\ mass) - binder\ in\ solvent + binder \tag{3.2}$$

The slurry-mix was put in a mixer (Thinky-Mixer ARE-250) and mixed at 1500 rpm for 25 min and an additional 2000 rpm for 5 min. The prepared slurry was coated onto a straightened aluminium foil fastened using a tape caster with a vacuum (MSK-AFA-HC100). The slurry was poured in a straight line in front of the doctor blade, which had a 150 µm raised gap, and coating was performed with a shear rate of 1.5 s^{-1}. A schematic of the slurry preparation is shown in Figure 3.1. The coated electrodes were placed in a vacuum oven to dry at 90 °C for 21 hours.

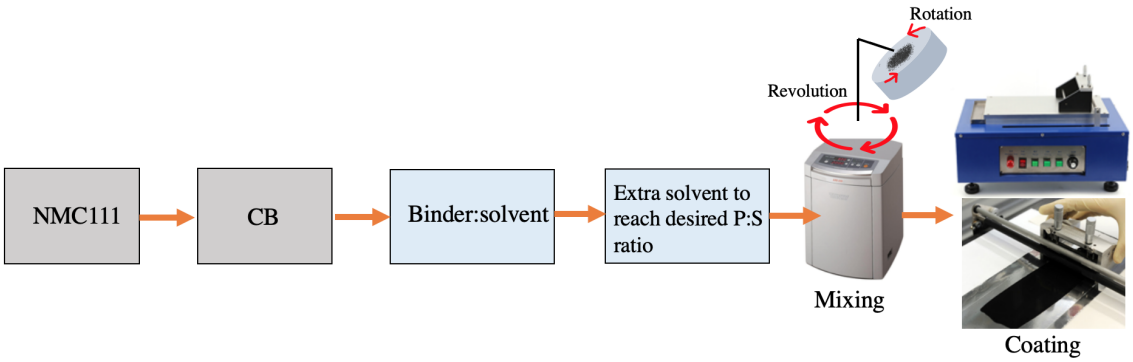

Figure 3.1: Mixing sequence of the slurry preparation. P:S denotes powder to solvent ratio and CB denotes Carbon Black. Figure inspired by Bryntesen *et al.* [11].

Table 3.1: Detailed list of materials used and their suppliers

Materials	Chemical Name and Abbreviation	Supplier	Product code
Active Material	NMC111 $LiNi_{1/3}Mn_{1/3}Co_{1/3}O_2$	Targray	N/A
Binder 1	PVDF Poly(vinylidene flouride) average Mw 540,000 by GPC, powder	Sigma-Aldrich	1002912638
Binder 2	Lignin Alkali - low sulfonate content	Sigma-Aldrich	1003004015
Conductive Carbon	Carbon Black (Super C45)	TIMCAL C-NERGY^{TM}	N/A
Solvent	NMP N-Methyl-2-pyrrolidone	Sigma-Aldrich	102135677
Electrolyte	$LiPF_6$	Sigma-Aldrich	1002988447

3.1.1 Varying powder to NMP ratio

Increasing or decreasing the powder to NMP (P:NMP) ratio only affects how much NMP should be added to the slurry. The slurry mixing was the same for all samples as they follow the standardised 85 wt% NMC111, 10 wt% CB and 5 wt% PVDF. The amount of NMP was calculated using Equation 3.2. The chosen P:NMP ratios were 1:1.5, 1:2 and 1:2.5. All slurries followed the same mixing, coating and drying procedure as mentioned in Section 3.1.

3.1.2 Increasing the wt% of the NMC111

Increasing the wt% NMC111 affected the whole slurry formula. The chosen wt% of the NMC111 were 85, 90 and 96, with twice as much CB as PVDF, as shown in Table 3.2. The amount of each chemical was calculated using Equation 3.1. The powder to NMP (P:NMP) ratio was 1:2. All slurries followed the same mixing, coating and drying procedure as explained in Section 3.1.

Table 3.2: Chemicals used and the wt% of each component

Active material	Conductive material	Binder
85 wt% NMC111	10 wt% CB	5 wt% PVDF
90 wt% NMC111	6.67 wt% CB	3.33 wt% PVDF
96 wt% NMC111	2.67 wt% CB	1.33 wt% PVDF

3.1.3 Introducing lignin as binder

The lignin binder was dissolved in NMP to make a 1:20 wt% solution of lignin:NMP, and mixed for 20 hours before use in slurry production. Lignin was introduced by gradually exchanging the PVDF binder with lignin. The formula was still 85:10:5 (NMC111:CB:Binder). The exchange was performed with lignin:PVDF ratios of 1:2 and 1:1. The slurry mixing began with adding the NMC111 and CB powders. The PVDF/NMP solution was then added, followed by the lignin/NMP solution. The amount of each chemical was calculated using Equation 3.1. Extra NMP was added to reach the desired 1:2 P:S ratio from Equation 3.2. The prepared slurry was coated onto a straightened aluminium foil fastened using a tape caster with a vacuum (MSK-AFA-HC100). The slurry followed the same mixing, coating and drying procedure as described in Section 3.1. Eventually, the PVDF binder was completely replaced with lignin. The wt% was still 85:10:5 (NMC111:CB:Binder). Initially, the NMC and CB powders were added, followed by the lignin/NMP solution, where the amounts were calculated using Equation 3.1. The amount of NMP needed to reach 1:2 P:S ratio was calculated using Equation 3.2. The slurry followed the same mixing and coating procedure as described in Section 3.1; however, the drying was completed at 50 °C as well as the standard 90 °C in the vacuum oven for 21 hours.

Water as solvent

The lignin/water (L/W) solution was mixed in a 1:20 wt% lignin:water ratio for 24 hours with 10 wt% acetone added to ensure the dissolution of lignin. The cathode-slurry mixing followed the same procedure as in section 3.1 with the wt% of 85:10:5 (NMC111:CB:Binder), initially adding the NMC111 and CB powders, followed by 5 wt% of PEG to the amount of lignin, and finally the L/W mixture. The amount of each component was calculated using Equation 3.1. A timer was started when the L/W solution was introduced in the powder mix in order to track the exposure time of NMC to water. Finally, extra water was added to reach the desired P:water (P:W) ratio, which was calculated using Equation 3.2. The P:W ratios tested were 1:1.5, 1:1.7 and 1:2. The slurries were mixed in a mixer (Thinky-Mixer ARE250) for 24 minutes at 2000 rpm. The slurry was coated onto a straightened aluminium foil fastened using a tape caster with a vacuum (MSK-AFA-HC100). The slurry was poured in a straight line in front of the doctor blade with a 200 µm raised gap, and coated with a shear rate of 2.0 s^{-1}. The samples were dried in a convection oven at 50 °C with an air velocity of 0.5 m/s.

Introducing phosphoric acid

A 1:10 wt% lignin:water solution was made in order to facilitate lower powder to water (P:W) ratios, with 10 wt% acetone added to ensure the dissolution of lignin. The solution was mixed for 24 hours prior to use.

A pre-made phosphoric acid (PA) solution (pH = 1.61) was added to the slurry, with 1:100 wt% ratio PA:NMC111. Using 0.2 mL of PA in the slurry, the amount of NMC111 to be added was calculated from the diluted PA, allowing the calculation of the amounts of remaining components.

The amounts of the different components for a slurry with 0.2 mL PA solution is shown in Table 3.3, with a powder wt% 85:10:5 (NMC111:CB:Binder) ratio. The mixing procedure began with adding NMC111 and CB, followed by the PA solution. As PA was diluted with water, a timer was started when the PA was introduced to the powders. The new L/W solution in 1:10 wt% ratio was used, and the amount of extra water added to reach the P:W 1:1.7 ratio was calculated with Equation 3.2. The slurry was mixed for 25 minutes at 1500 rpm and 5 minutes at 2000 rpm in a mixer (Thinky-Mixer ARE-250). The prepared slurry was coated onto a straightened aluminium foil fastened using a tape caster with a vacuum (MSK-AFA-HC100). The slurry was poured in a straight line in front of a doctor blade that had a 150 µm raised gap, and coated with a shear rate of 1.5 s^{-1}.

Table 3.3: Amount of each chemical to make the cathode slurry mix with 0.2 mL of PA

NMC [g]	CB [g]	Diluted PA [mL]	Lignin:water 1:10 [g]	Water[g]
0.5606	0.06594	0.2	0.3297	0.6230

3.2 Coin-cell assembling

The dried coatings were cut into circular electrodes with a radius of 7.5 mm using an electrode cutter. The electrodes were weighted and put into zip-lock bags, being careful not to touch the cathode material as to avoid damaging it. The cells where then placed in a glove-box with a dry argon atmosphere for coin cell assembly. The cathodes were left in open zip-lock bags in the glove-box over night to ensure that any water and oxygen dissipated from the electrodes. The coin cells were assembled according to the order of components illustrated in Figure 3.2, and then crimped (MSK-PN110-S) at 90 psi.

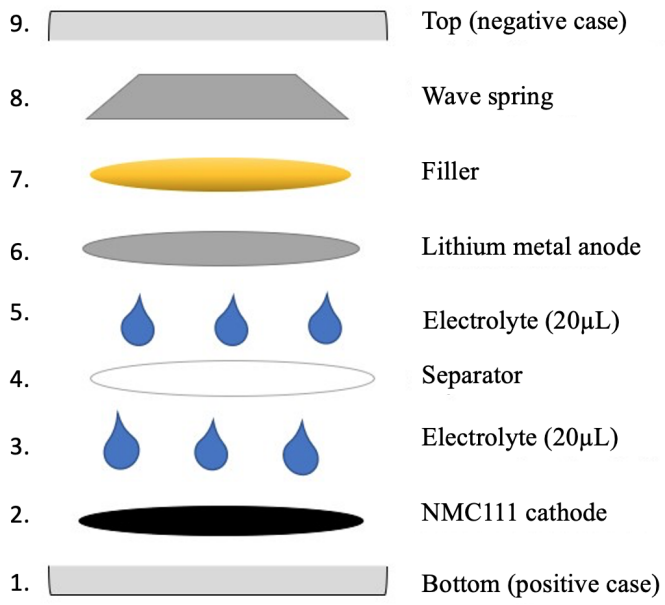

Figure 3.2: Coin-cell assembly for a 232 battery. Figure inspired by Bryntesen *et al.* [11].

3.3 Calendering

A hot rolling press (MSK-HRP-01, MTI Corporation) with the speed set to 9.75 mm/s and the gap set to 40 μm was used to calender the cathode coatings. The samples were calendered four times, with a 180° change in direction between each calendering.

3.4 Characterization methods

3.4.1 Rheology measurements

A rheometer AR-G2 (TA Instruments Trios V2.6) with a 40 mm parallel plate geometry at 20 °C was used to test slurry rheology. The test was carried out using a steady-state flow mode, followed by an oscillatory mode. Prior to testing, the samples that were not tested directly after production were remixed at 2000 rpm for 10 minutes in a mixer (Thinky-Mixer ARE-250). A 30 second soak time was set to achieve the correct temperature and equilibrium of the slurry before testing.

The viscosity of the slurry was measured with increasing shear rate (1/s) from the steady-state flow mode. The loss storage modulus (G´) and loss modulus (G´´) was measured with an increasing angular frequency from the oscillatory mode.

3.4.2 Scratch tests

A micro scratch tester (MST, Anton Paar) was used to investigate the effect of calendering on the mechanical properties of the electrode.

A linear progressive scratch test with a Rockwell diamond indenter was placed on the sample. The non-calendared samples had increasing loads from 30 - 200 mN applied, with a loading rate of 28.33 mN/min for a 3 mm scratch. For the calendared samples, an increasing load from 30 - 500 mN was applied, with a loading rate of 94 mN/min for a 5 mm scratch.

3.4.3 SEM

The cathodes were examined using two different SEMs with different resolutions. Table 3.4 displays the SEMs set working parameters. A table SEM (JEOL) was used to image the cathodes surface, where the bigger SEM (Zeiss) was used to image the particles. The software Image J (version 1.53a) was used to measure the crack length and crack area on cathode coatings from the SEM images.

Table 3.4: Settings for SEM analysis

Apparatus	Working distance	Accelerating Voltage	Magnification
JEOL Neoscope JCM-6000	19-21 mm	10 kV	200x
Zeiss Supra 55VP	10-20 mm	10 kV	3500x

3.4.4 EDS

The EDS was integrated to the SEM (Zeiss Supra 55VP). The cross-section was assessed by cutting the cathode in half using scissors. The sample examined was placed in the SEM with the cross-section adjusted to where the electron beam was emitted. A Everheart-Thornley Secondary Electron Detector was used to detect the materials X-rays at the SEM magnitude of 3450x.

3.4.5 Galvanostatic Cycling

The coin cells were tested electrochemically through galvanostatic cycling. Lithium metal was used as the anode, and therefore the potential was measured relative to Li/Li^+. All electrochemical tests where done on a computer controlled Lahne CT2001A at room temperature. The mass of the AM was added to calculate the specific capacity continuously. The coin cells were initially discharged, therefore all tests started with charge cycles. The charge cycles were programmed with a cut-off

voltage $\geq$ 4.3 V and the discharge cycles were cut-off at $\leq$ 3.0 V. The experimental time was set to 10 seconds for both the charge and discharge step.

The settings for the galvanostatic cycling tests are described in Table 3.5. During the first three cycles, a relatively low charge and discharge C-rate of C/10 was applied to ensure the formation of the SEI layer and avoid structural collapse of the cathode material. The following 19 cycles had a constant voltage charge rate (CVC), with a charge C-rate of C/2 followed by a predefined constant voltage of 4.3 V until the C-rate $\geq$ of C/10 was reached. The discharge C-rate was set to C/2.

Table 3.5: Settings galvanostatic cycling tests

Cycle	**Charging**		**Discharging**
	C-rate	CV	C-rate
1-3	C/10	-	C/10
3-19	C/2	4.3	C/2

Rate test
During the first four cycles, a charge and discharge C-rate of C/10 was applied, followed by an increasing charge C-rate from C/5 to C/2 and an increasing discharge C-rate from C/5 to 5C. A constant current was applied from cycle 4 - 29 until the desired current was reached, then followed by a constant voltage of 4.3 V until the C-rate $\geq$ of C/10 was reached. During the final cycles, both the charge and discharge C-rate was restored to the initial C-rate. Table 3.6 presents the rate-test experimental settings.

Table 3.6: Setting rate test

Cycle	**Charging**		**Discharging**
	C-rate	CV	C-rate
1-4	C/10	-	C/10
4-9	C/5	4.3	C/5
9-14	C/2	4.3	C/2
14-19	C/2	4.3	1C
19-24	C/2	4.3	2C
24-29	C/2	4.3	5C
29-34	C/10	-	C/10

3.5 Convection drying

The prepared slurry was coated onto a straightened and fitted aluminium foil fastened using a tape caster with a vacuum (MSK-AFA-HC100). Slurry was poured in a straight line in front of the doctor blade (200 µm raised gap), and coated with a shear rate of 2.0 s^{-1}. The aluminium foil was fastened to a spatula using aluminium tape to avoid the sample moving around when the airflow was on (Figure 3.3). After the sample was placed on the scale, the scale was tared to record the mass loss. To ensure stable readings, there was no movement in close proximity to the oven, as it would affect the air flow on the scale. The weight was recorded with intervals of 30 seconds drying, then two stable readings. A python script (Appendix B) was used to plot the values. The drying experiments with their respective drying parameters are presented in Table 3.7.

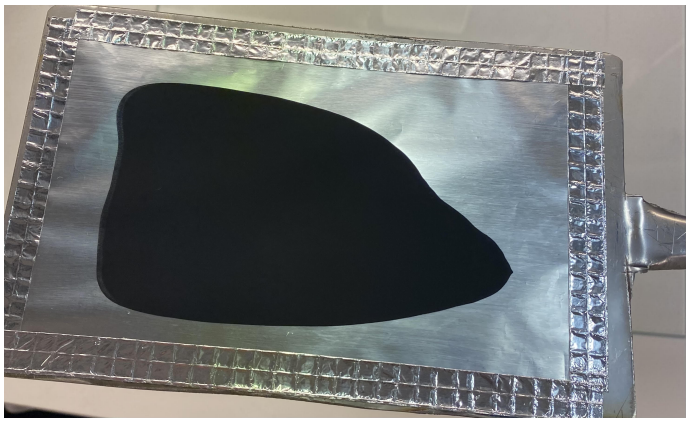

Figure 3.3: The coated Al-foil fastened to the spatula with aluminium tape prior to drying in the convection oven.

Table 3.7: . All samples in the experiments used a 85:10:5 wt% NMC111:CB:binder. P:S denotes powder to solvent wt% ratio

P:S	Drying temp.[°C]	Air flow [m/s]	Binder/Solvent
1:2	room temp.	0	PVDF/NMP
1:2	50	1	PVDF/NMP
1:2	90	1	PVDF/NMP
1:2	150	1	PVDF/NMP
1:2	150	0.5	PVDF/NMP
1:2	150	0.5	Lignin/NMP
1:2	50	0.5	Lignin/Water
1:1.7	50	0.5	Lignin/Water
1:1.5	50	0.5	Lignin/Water

Chapter 4

Results and Discussion

4.1 Varying slurry composition

The following sections present and discuss the results when varying different slurry parameters. The goal was to understand how changing the different slurry parameters affect the cathode properties and cycling performance, in order to select the overall best performing sample as a reference for comparison moving into further testing. An overview of the samples, tests, and an evaluation of performance are presented in Figure 4.1.

	Rheology	Mechanical	Mechanical*	Cycling	Cycling*
Varying P:NMP ratio, PVDF binder, 90˚C	1:1.5	1:1.5	1:1.5	1:1.5	1:1.5
	1:2 (Std)	1:2 (Std)	1:2 (Std)	1:2 (Std)	1:2 (Std)
	1:2.5	1:2.5	1:2.5	1:2.5	1:2.5
Varying wt%NMC111, PVDF binder, 90˚C	85 wt% (Std)	85 wt% (Std)	85 wt% (Std)	85 wt% (Std)	85 wt% (Std)
	90 wt%	90 wt%	90 wt%	90 wt%	90 wt%
	96 wt%	96 wt%	96 wt%	96 wt%	96 wt%
Introducing lignin binder, 90˚C	Lignin(1):PVDF(2)	Lignin(1):PVDF(2)	Lignin(1):PVDF(2)	Lignin(1):PVDF(2)	Lignin(1):PVDF(2)
	Lignin(1):PVDF(1)	Lignin(1):PVDF(1)	Lignin(1):PVDF(1)	Lignin(1):PVDF(1)	Lignin(1):PVDF(1)
	Lignin	Lignin	Lignin	Lignin	Lignin
Varying P:NMP ratio, lignin binder, 50˚C	Lignin 1:1	Lignin 1:1	Lignin 1:1	Lignin 1:1	Lignin 1:1
	Lignin 1:1.5	Lignin 1:1.5	Lignin 1:1.5	Lignin 1:1.5	Lignin 1:1.5
	Lignin 1:2	Lignin 1:2	Lignin 1:2	Lignin 1:2	Lignin 1:2
Varying P:W ratio, lignin binder 50˚C	Lignin/Water 1:1.5	Lignin/Water 1:1.5	Lignin/Water 1:1.5		
	Lignin/Water 1:1.7	Lignin/Water 1:1.7	Lignin/Water 1:1.7		
	Lignin/Water 1:2	Lignin/Water 1:2	Lignin/Water 1:2		
Lignin/Water with PA, 50˚C	Lignin/Water-PA	Lignin/Water-PA	Lignin/Water-PA		

O – Good
O – Reasonably
O – Not satisfactory

*Calendered, Powder:NMP (P:NMP) ratio, Powder:Water (P:W) ratio

Figure 4.1: An overview of all samples when varying slurry parameters together with their performance. The colour of the cell represents how well the samples performed, where green cells performed good, yellow performed reasonably and red performed unsatisfactory. Tests have not been performed on the samples in grey cells.

4.1.1 Powder to NMP ratio

Changing the powder to NMP solvent ratio (P:NMP) gave an overview on how the amount of NMP affected viscosity and how the viscosity relates to cycling data. All tested samples have a powder wt% ratio of 85:10:5 (NMC111:CB:PVDF). The samples with P:NMP ratio of 1:1.5, 1:2, and 1:2.5 shown in Figure 4.2 exhibited a decreased viscosity with increasing shear rate (1/s) and decreased viscosity with a increasing amount of NMP. This is similar to what Shroofy *et al.* [43] reported in their studies. As presented in Figure 4.3, the slurry samples with a P:NMP ratio of 1:2 and 1:2.5 both had a G´<G´´, which implies a liquid-like behavior. Whereas the P:NMP ratio of 1:1.5 had a G´>G´´, which suggests a gel-like behavior. Gel-like properties are undesirable, and no further tests were performed with the P:NMP ratio 1:1.5.

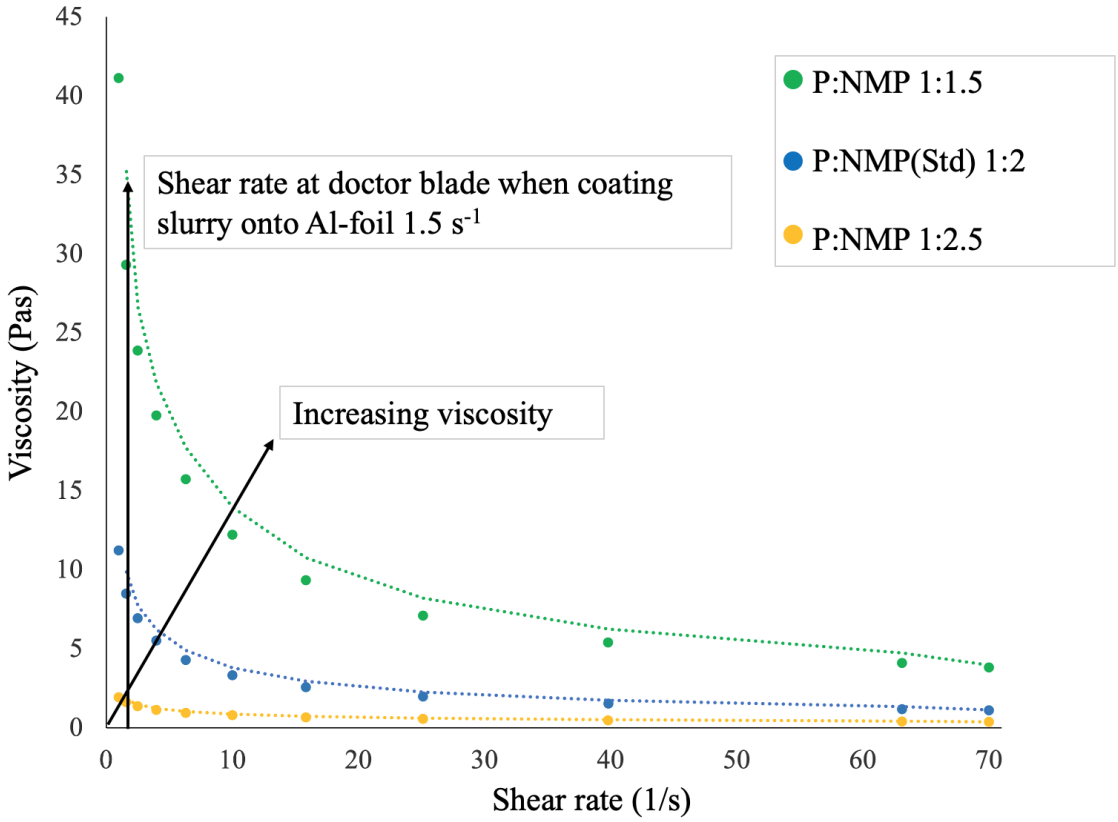

Figure 4.2: Flow rheology measurements of the viscosity as a function of shear rate on slurries with an increasing amount of NMP solvent. P= 85:10:5 (NMC111:CB:PVDF). The vertical arrow shows the shear rate used in the doctor blade when coating slurry onto the Al-foil. The 45° arrow show increasing viscosity as a function of shear rate. All samples are coated with 150 μm raised gap.

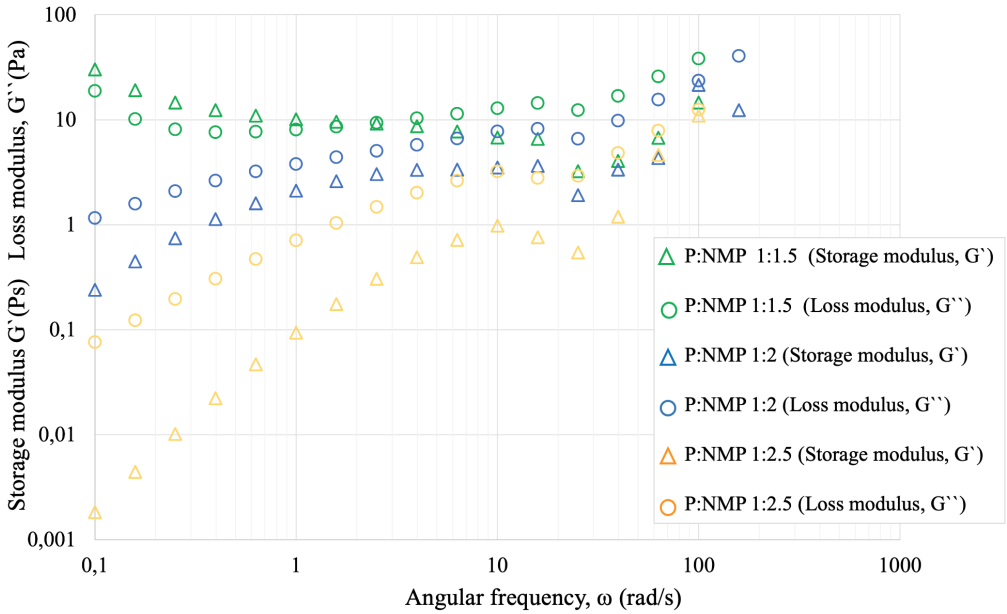

Figure 4.3: Oscillatory shear measurements as a function of angular frequency sweeps, with an increasing amount of NMP. P= 85:10:5 (NMC111:CB:PVDF). All samples are coated with 150 μm raised gap.

The galvanostatic cycling tests of the P:NMP ratios of 1:2 and 1:2.5 are presented in charge/discharge plots in Figure 4.4 and 4.5, respectively. The P:NMP ratio of 1:2 had an initial discharge capacity of 156 mAh/g (C/10), which can be compared to the expected practical capacity of 160 mAh/g listed in Table 2.1. The electrode functioned stably during repeated charge-discharge cycles with no obvious reduction in performance. It had a capacity retention of 93 % after 19 cycles. The P:NMP 1:2.5 showed an initial discharge capacity of 149 mAh/g (C/10), which is almost as good as the P:NMP 1:2 ratio. The P:NMP ratio 1:2.5 sample does not have a plateau during cycle 1. The CE is 80 % (Cycle 1), which could mean that a different amount of Li^+ has intercalated and deintercalated into/from the electrodes. The lack of a plateau may indicate that unknown side reactions are taking place, preventing the Li^+ to react with NMC111 or C, which is compensated by decreasing the potential. The CE increases to 98.5% after the 5th cycle and to 99% during the following cycles. It is difficult to explain the exact reason for the absence of a plateau. This can be investigated through an impedance test; however, since it is a formation cycle and the cell restores after the 3rd cycle, it is not crucial for the overall performance of the coin cell. For later cycles with a higher C-rate of C/2, the overall performance of the P:NMP 1:2.5 was better than the P:NMP 1:2 ratio. After 19 cycles, it had a capacity retention of 88.5%; however, the difference in performance was not significant enough to make up for the fact that the P:NMP 1:2.5 was very fluid and challenging to coat onto the Al-foil. Because of this, the P:NMP 1:2 ratio was chosen as the standard ratio in further testing.

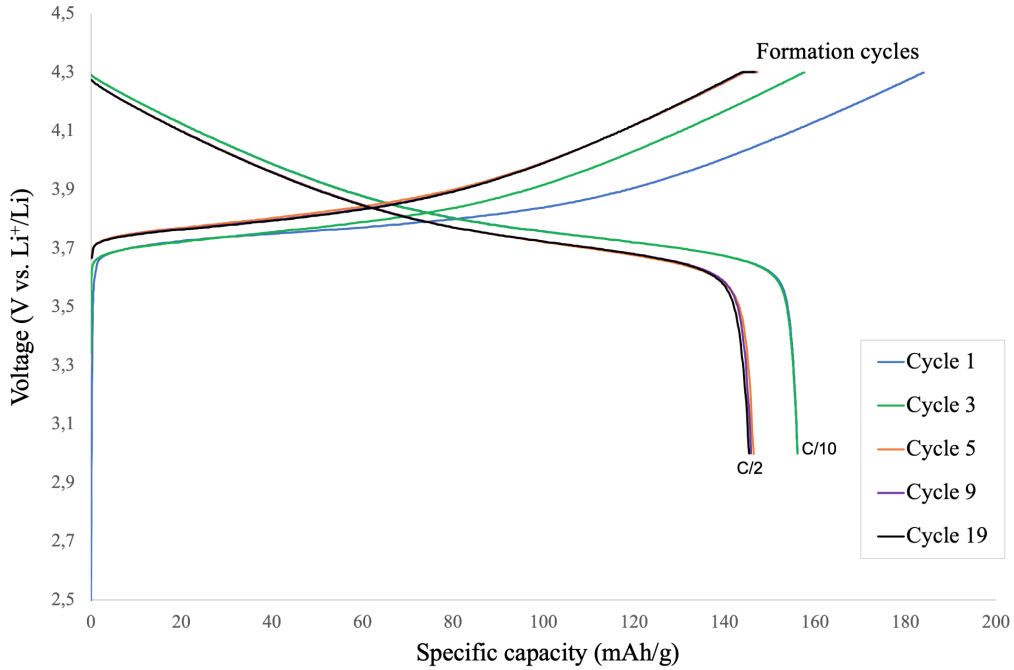

Figure 4.4: Charge/discharge plot of a coin cell with powder to NMP ratio 1:2, powder wt% ratios of 85:10:5 (NMC111:CB:PVDF), coated with 150 μm raised gap. The specific capacity (mAh/g) is plotted as a function of voltage (V vs. Li/Li$^+$).

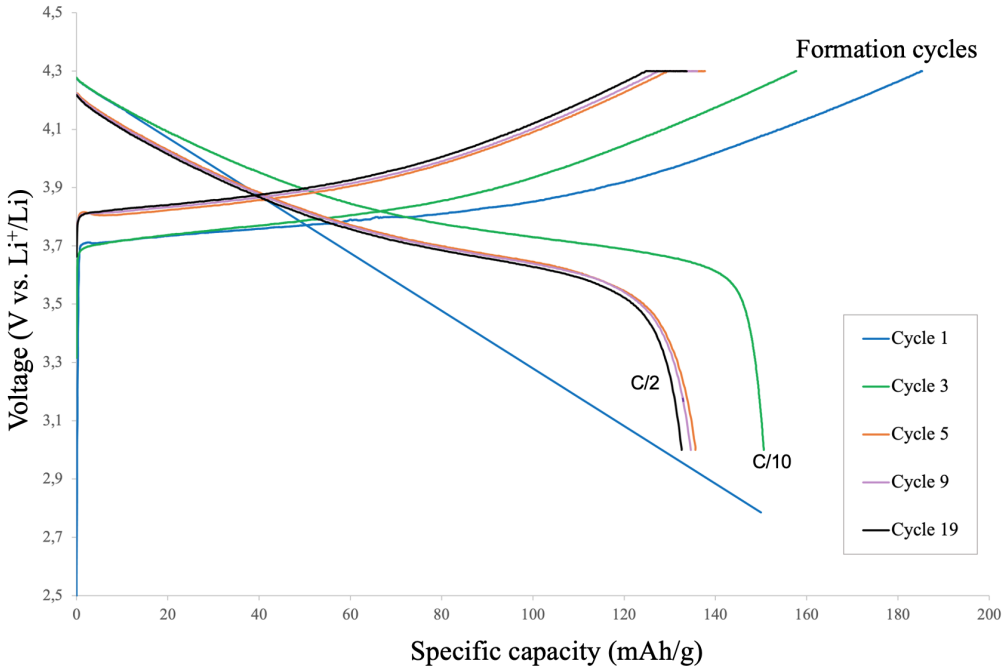

Figure 4.5: Charge/discharge plot of a coin cell with powder to NMP ratio 1:2.5, powder wt% ratios of 85:10:5 (NMC111:CB:PVDF), coated with 150 μm raised gap. The specific capacity (mAh/g) is plotted as a function of voltage (V vs. Li/Li$^+$).

4.1.2 Increasing weight percentage of NMC111

The weight percentage of NMC111 was increased to see how this affected the slurry properties. A higher amount of AM in the slurry should give a higher energy density of the battery, as materials like the binder and CB do not contribute directly to the electrochemical storage capabilities of the battery. Visual analyses of the cathode surfaces were performed, and the electrochemical performance of the suitable cathodes was tested. The increase of wt% NMC111 from 85 to 90 and 96 led to a decrease in CB and binder in the slurry. The decrease in CB drastically decreased the slurry viscosity as CB is a very light material, meaning a small decrease in mass resulted in a large decrease in powder volume. When coating the samples consisting of 85 wt% NMC111 and 90 wt% NMC111, the samples had an even surface texture. The sample consisting of 96 wt% NMC111 became almost transparent due to the low powder mass, with rough surface texture, and no useful electrodes could be produced from the coating. The effect of increasing wt% NMC111 is shown in Figure 4.6.

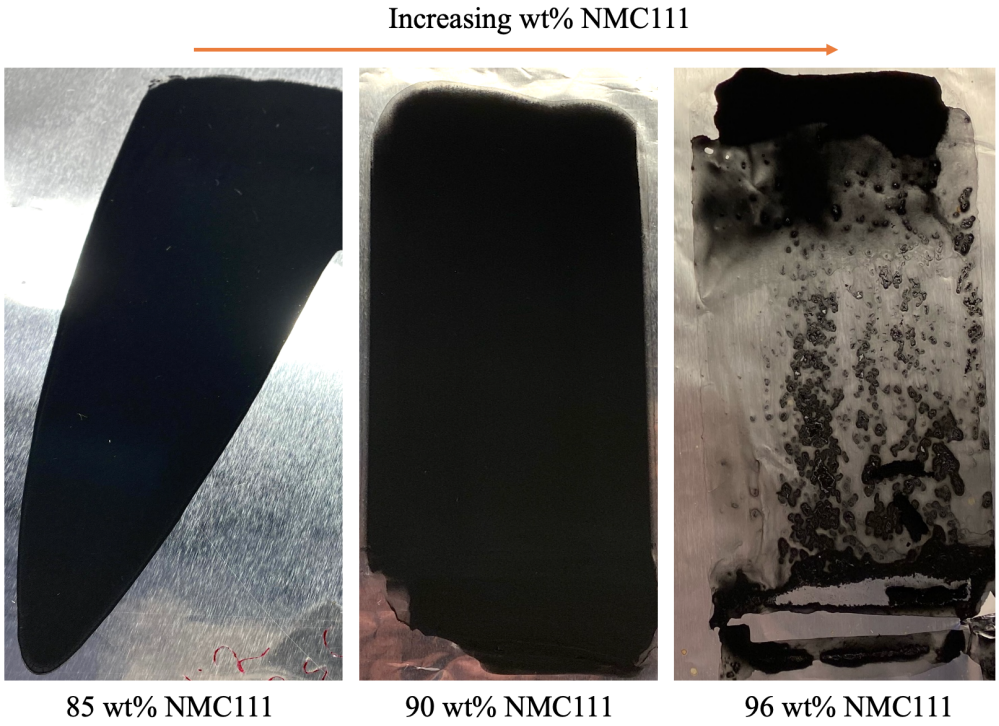

Figure 4.6: Surface texture of samples dried in a vacuum oven at 90 °C with an increasing wt% of NMC111, powder to NMP ratio of 1:2, coated with a 150 μm raised gap.

From galvanostatic cycling tests, the 90 wt% NMC111 had an initial discharge capacity of 130 mAh/g (C/10) (Figure 4.7a) during the formation cycles, which is lower than the 85 wt% NMC111 (Figure 4.3). Even though the 90 wt% NMC111 sample had a higher capacity retention of 82.9% (Cycle 1-19), the overall performance was still not as good as the one with 85 wt% NMC111 (Cycle 1-19). Calendering increased the initial discharge capacity from 130 - 140 mAh/g (C/10) (Figure 4.7b) during the formation cycles. Here, the 90 wt% NMC111 performed better than the 85 wt% NMC111 sample; however, it did not perform better when the C-rate increased from C/10 to C/2. The calendered sample was set to cycle 100 cycles and managed to cycle 59 cycles (56 mAh/g). It had a capacity retention of 51.6% (cycle 1-19) and 33.6 % (cycle 1-59). The shape of discharge cycle 19 (Figure 4.7a) does not have the characteristic shape of NMC111 with a plateau around 4V. Therefore, it is reasonable to believe that it originated from another crystal structure. Another reason could be unfamiliar side reactions. At the beginning of charge cycle 1 (Figure 4.7a and 4.7b) distinct tops are observed, which may be caused by side reactions or impurities in the cathode materials.

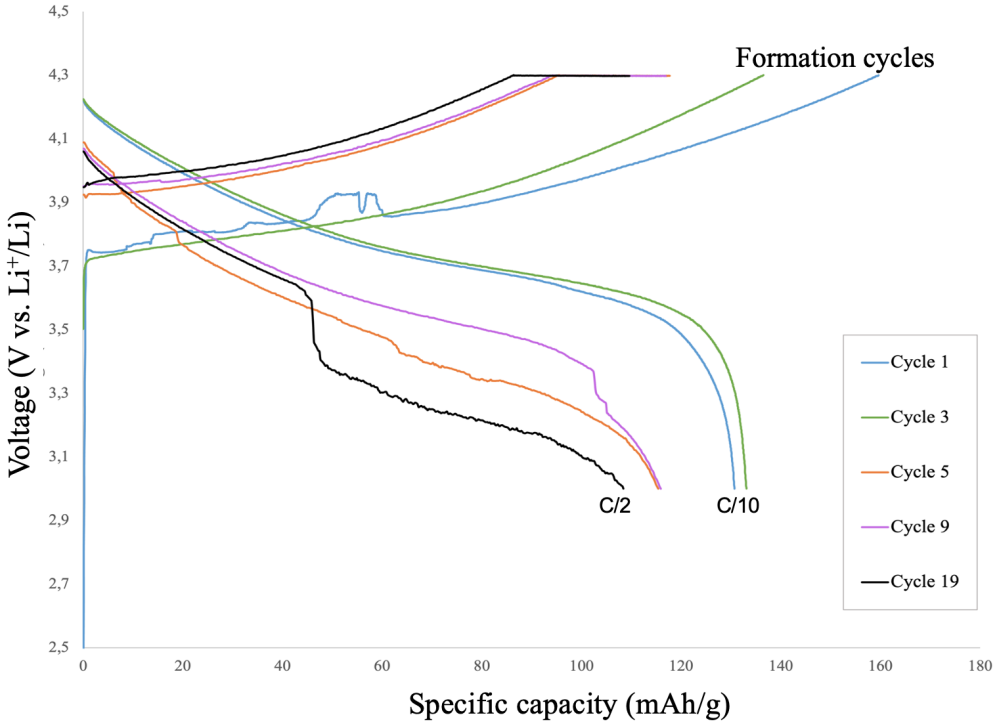

(a) Non-calendered

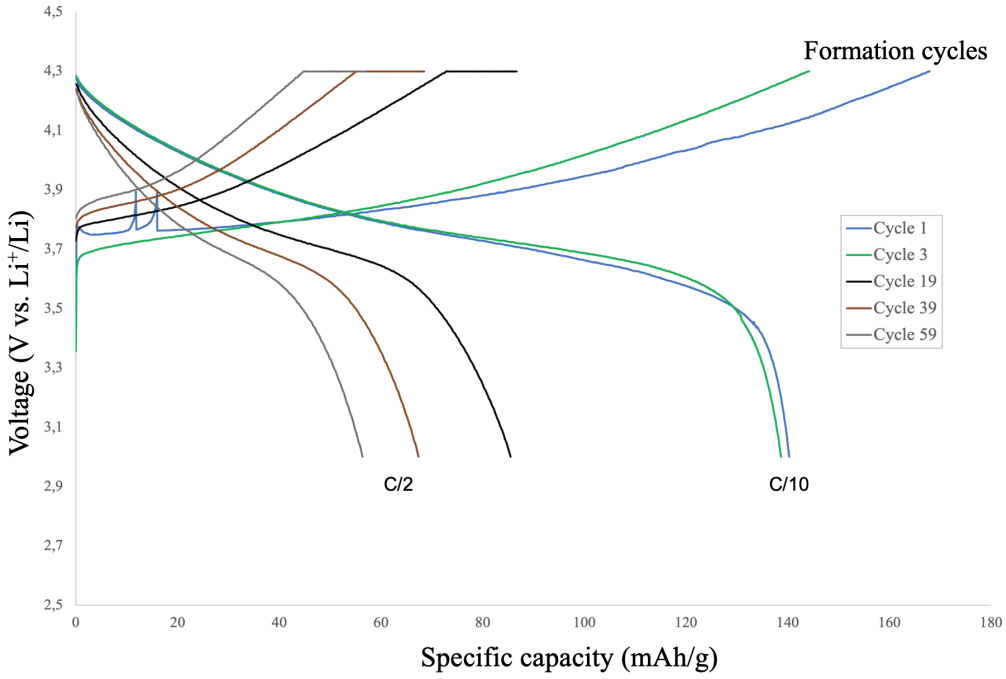

(b) Calendered

Figure 4.7: Charge/discharge plot of a coin cell with a (a) non-calendered coating (b) calendered coating. Both samples have a powder wt% ratios of 90:6.67:3.33 (NMC111:CB:PVDF), powder to NMP ratio of 1:2, coated with 150 μm raised gap. The specific capacity (mAh/g) is plotted as a function of voltage (V vs. Li/Li$^+$).

In a rate test (Figure 4.8), the 90 wt% NMC111 sample performed similarly to the 85 wt% NMC111 at lower C-rates but failed at C-rates between 1C and 5C, unlike the 85 wt% NMC111, which only decays slightly at higher C-rates. Both samples restored when the C-rate was lowered to the initial

C-rate of C/10. The calendered 90 wt% NMC111 sample failed completely even when cycling at low C-rates; however, it showed an increased initial discharge capacity when the C-rate was lowered to the initial C-rate of C/10 after 30 cycles. In theory, an increased amount of AM should improve the capacity. Most likely, both 90 wt% NMC111 and the calendered 90 wt% NMC111 sample has lower capacity than 85 wt% NMC111 sample due to cracks and poor adhesion.

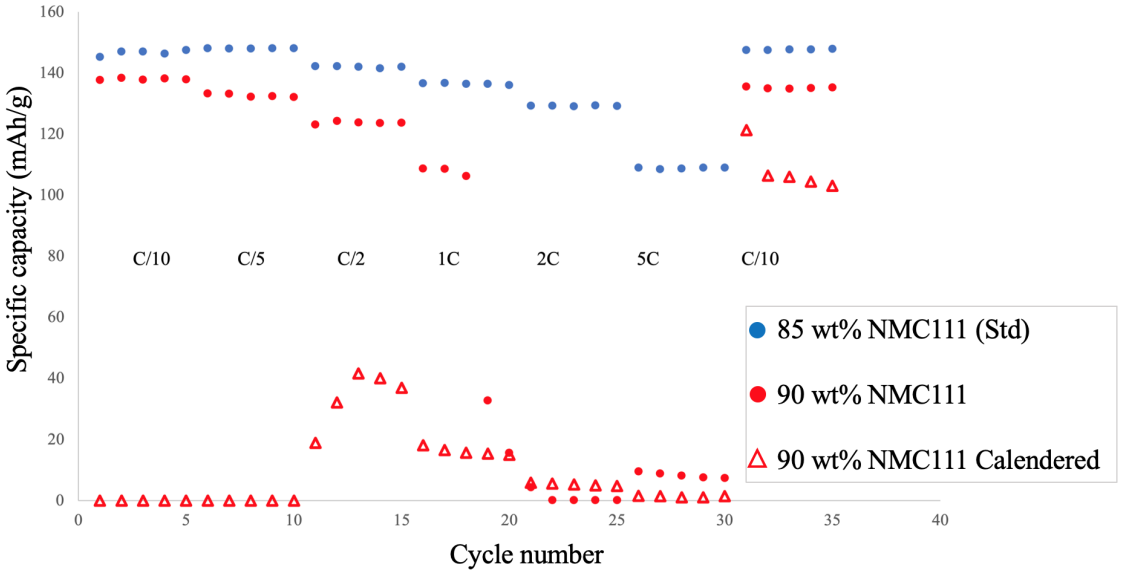

Figure 4.8: Rate test on coin cells with powder wt% ratio of 85:10:5, 90:6.67:3.33 and calendered 90:6.67:3.33 (NMC111:CB:PVDF). All samples were coated with a 150 μm raised gap and have a powder to NMP ratio of 1:2. The specific capacity (mAh/g) is plotted as a function of cycle number with increasing C-rate until cycle 29, where the C-rate is set to its initial C/10.

Based on the results presented and discussed above, and the conclusions from section 4.1.1, the 85 wt% NMC111 with a powder to NMP (P:NMP) ratio of 1:2 showed the overall best performance both in terms of ease of appliance, a smooth coating surface, electrochemical performance and performance in the rate test. Therefore, the composition 85:10:5 (NMC111:CB:PVDF) with P:NMP ratio 1:2 was chosen as the standard sample for comparison going into further testing.

4.1.3 Introducing lignin as a binder

Lignin was gradually introduced as a binder by substituting the PVDF binder in a lignin:PVDF ratio of 1:2 and 1:1 in a slurry with the wt% ratios of 85:10:5 (NMC111:CB:Binder). The electrochemical performance of the cathodes with increasing lignin ratio was tested through galvanostatic cycling. The mechanical properties (i.e., adhesion strength) of the electrodes with increasing wt% of lignin were tested through scratch testing of non-calendered and calendered samples.

The charge/discharge plot of the 1:1 combination of lignin and PVDF is presented in Figure 4.9a. This lignin(1):PVDF(1) sample has an initial discharge capacity of 110.9 mAh/g and capacity retention of 18.7 % after 19 cycles. It dropped from 110.9 mAh/g at C/10 to 41.7 mAh/g when the C-rate increased to C/2 between cycle 3 and 5. Despite the degradation on higher C-rates, the sample showed little variation in capacity from cycle 5 to 19. When calendering the lignin(1):PVDF(1) sample, the initial discharge capacity increased from 110.9 mAh/g to 136.6 mAh/g (Figure 4.9b), which is almost as good as the standard using pure PVDF as a binder and powder wt% ratios of 85:10:5 (NMC111:CB:PVDF) presented in Figure 4.4. After the 3rd cycle, the discharge capacity dropped significantly (50.9 mAh/g) but cycled stably with little variation in capacity between cycle 19 - 99. The sample had a capacity retention of 37.3 % after 19 cycles and 33.9 % after 99 cycles.

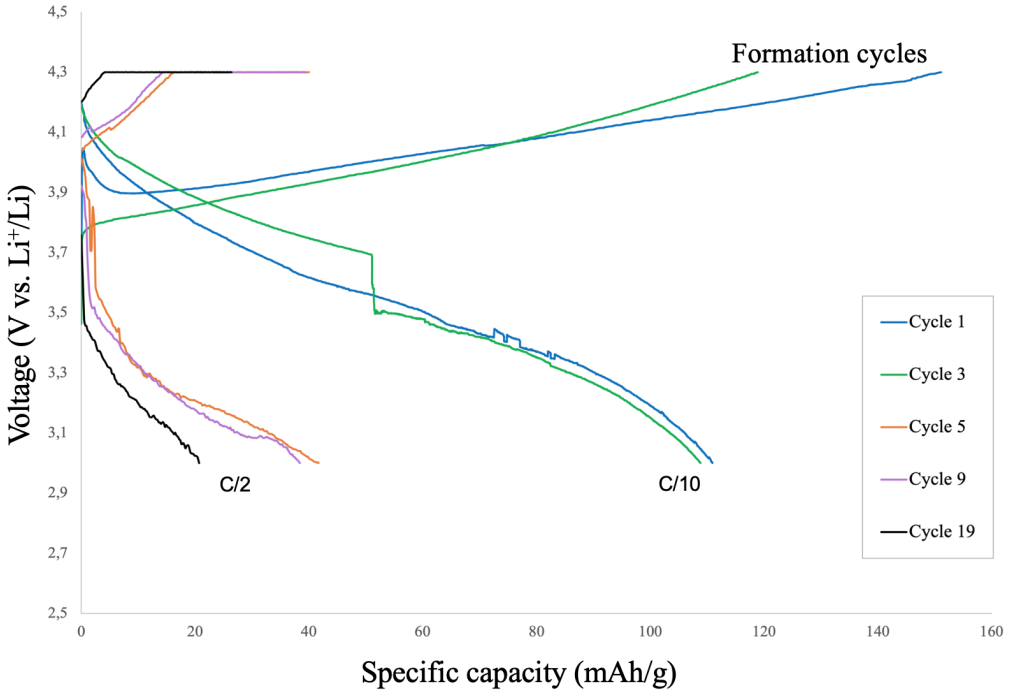

(a) Non-calendered

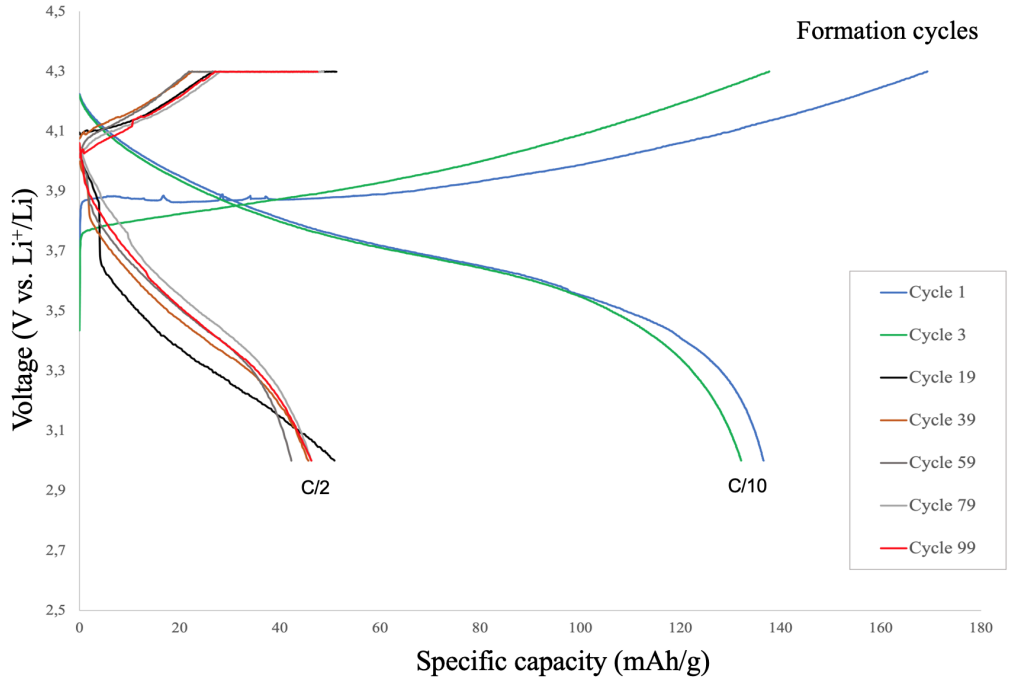

(b) Calendered

Figure 4.9: Charge/discharge plot of a coin cell with calendered cathode coating using a lignin to PVDF ratio of 1:1, powder wt% ratios of 85:10:5 (NMC111:CB:Binder), powder to NMP ratio of 1:2, coated with 150 μm raised gap. The specific capacity (mAh/g) is plotted as a function of voltage (V vs. Li/Li$^+$).

The 1:2 ratio of lignin:PVDF performed up to the standard (PVDF binder) when cycling at low C-rates (C/10), as shown in Figure 4.10. The performance gradually decreased with increasing C-rates, until it failed between 1C - 5C. The sample restores almost completely when the C-rate is lowered to the initial C/10. On the lower C-rates between C/10 - 1C, the calendered lignin(1):PVDF(2) sample performed almost as well as the non-calendered lignin(1):PVDF(2).

When the C-rate is lowered to the initial C/10, the calendered lignin(1):PVDF(2) performed better than the non-calendered lignin(1):PVDF(2). The 1:1 ratio of lignin:PVDF (Figure 4.10) fails completely at both low and high C-rates during the rate test. This was partly fixed by calendaring the sample. The calendered lignin(1):PVDF(1) sample managed to cycle on low C-rates, but it experienced quick degradation with increasing C-rates. It restored when the C-rate was set to the initial C/10.

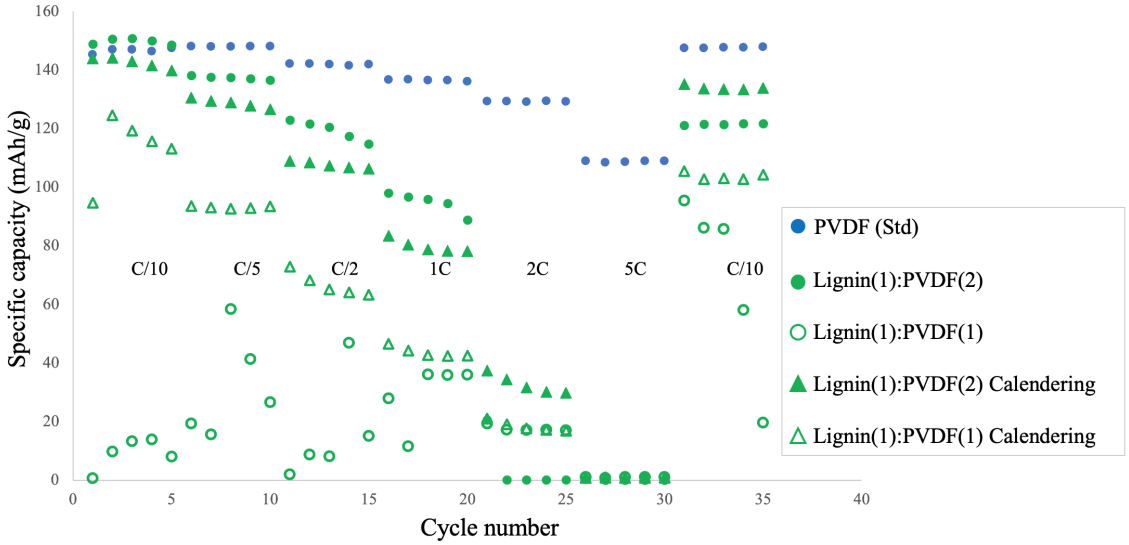

Figure 4.10: Rate test on coin cells with lignin:PVDF ratio of 1:1, 1:1 (calendered), 1:2, 1:2 (calendered), as well as pure PVDF. All samples have a powder wt% ratio of 85:10:5 (NMC:CB:Binder), powder to NMP ratio of 1:2, coated with 150 μm raised gap. The specific capacity (mAh/g) is plotted as a function of cycle number with increasing C-rate until cycle 29, where the C-rate is set to its initial C/10.

The rate tests in Figure 4.10 show that cathodes with larger amounts of PVDF versus lignin perform better. By looking at the cycling and rate test plots, they show that the performance of the battery generally improves after calendering the cathode material.

Pure lignin as binder

Pure lignin was introduced as a binder to improve the sustainability of the cathode. Exchanging the PVDF binder with water soluble lignin would enable aqueous processing of the cathodes, reducing the energy consumption in the production process. The lignin was added in a slurry with a powder wt% ratio of 85:10:5 (NMC111:CB:Lignin) and a varying powder:NMP (P:NMP) ratio. A rheology test of the slurries as well as visual analyses of the surfaces were completed for the varying P:NMP ratio, and the 1:2 P:NMP ratio was electrochemically tested as well.

Rheology tests were performed on samples with 1:2 and 1:1.5 P:NMP ratio. As shown in Figure 4.11, the samples exhibited a decreased viscosity with increasing shear rate (1/s) and increased viscosity with a decreasing amount of NMP, similar to when varying powder to NMP ratio when using PVDF as a binder in Section 4.1.1. Both the P:NMP ratio 1:1.5 and 1:2 had G´<G´´at lower frequencies (Figure 4.12), which suggests the preferable liquid-like behaviour when coating the cathode slurry onto the Al-foil.

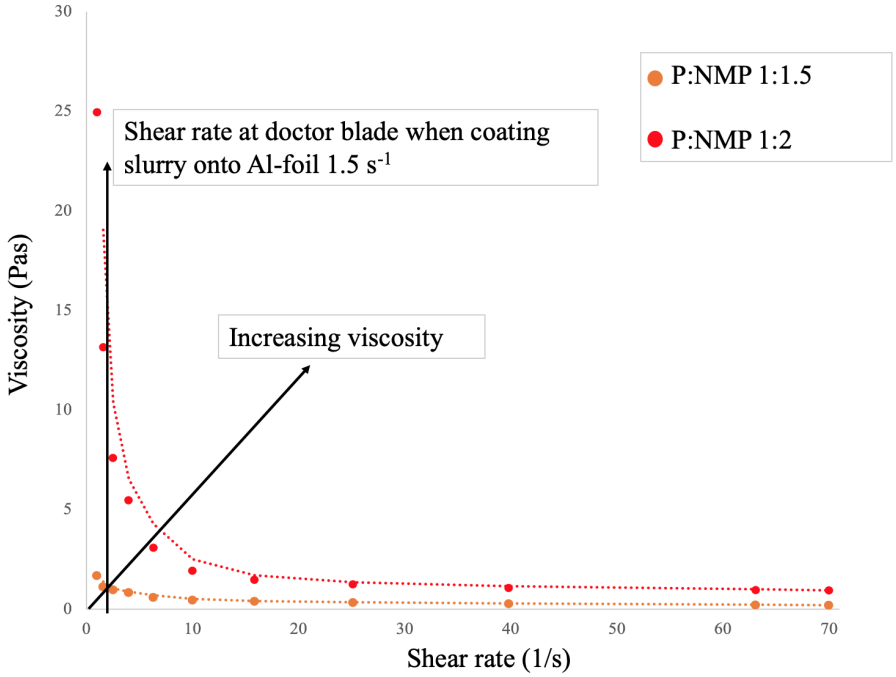

Figure 4.11: Flow rheology measurements of the viscosity as a function of shear rate on slurries with an increasing amount of NMP solvent and lignin as binder. The vertical arrow shows the shear rate used in the doctor blade when coating slurry onto the Al-foil. The 45° arrow show increasing viscosity as a function of shear rate. P= 85:10:5 (NMC111:CB:Lignin) and all samples are coated with a 150 μm raised gap

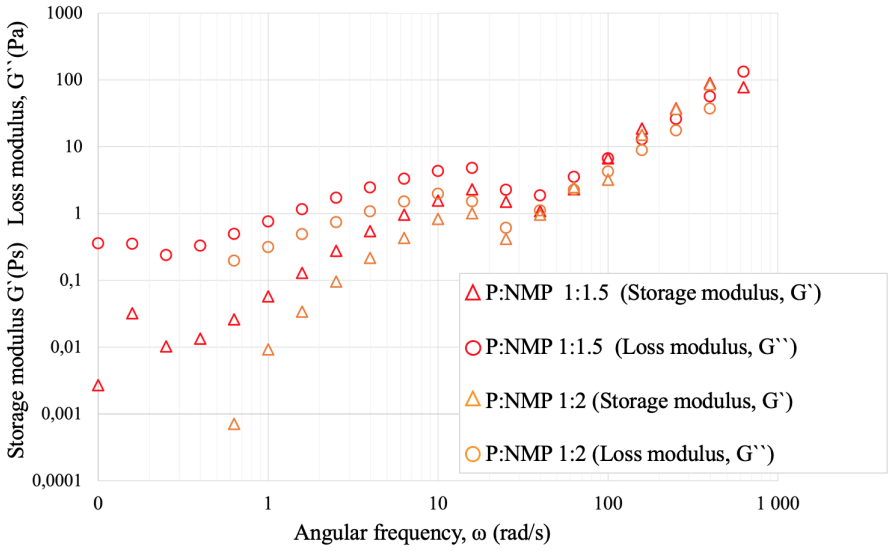

Figure 4.12: Oscillatory shear measurements as a function of angular frequency sweeps, with an increasing amount of NMP and lignin as a binder. P= 85:10:5 (NMC111:CB:Lignin). All samples are coated with a 150 μm raised gap.

From visual observations of the surface texture in Figure 4.13, it is clear that decreasing the NMP content caused rougher texture on the sample surfaces. The P:NMP ratio 1:2 had the least amount of cracks and an overall smoother surface. The rough texture on sample P:NMP 1:1 and 1:1.5 might be caused by the lignin binder not being dissolved adequately in the slurry; this could potentially be solved by increasing the mixing time.

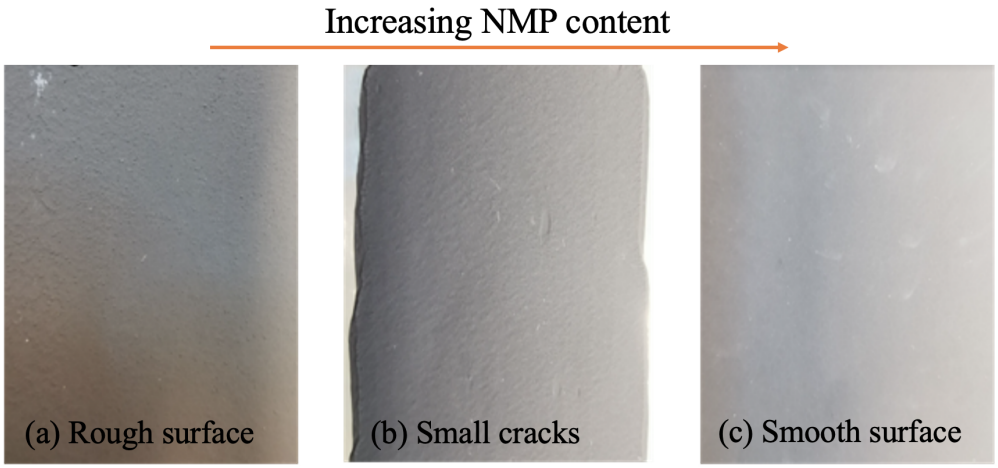

Figure 4.13: Coated surfaces using lignin as binder with powder wt% ratio of 85:10:5 (NMC111:CB:Lignin) and powder to NMP ratios of (a) 1:1, (b) 1:1.5, and (c) 1:2. All samples are coated with a 150 μm raised gap.

As the binder is the cohesive agent in the cathode material, it needs to form strong cohesion both between the particles in the cathode material and between the cathode material and the current collector. It is observed from Figure 4.14 that the sample with P:NMP 1:2 ratio dried at 90°C contains a relatively large area where the cathode material experienced poor adhesion with the Al-foil, and the coating has curled up along the edges. The curling may indicate that the sample has strong cohesion between the particles but low adhesion between the Al-foil and cathode material. The issue was partly solved by decreasing the drying temperature to 50°C. Despite the temperature reduction, poor adhesion was still observed in parts of the coating area, which lead to problems when cutting electrodes as the poor adhesion made the cathode material flake. The lignin used was unleached, which means the binder material partially consisted of lignin particles with low MW (i.e., short lignin chains). Lu *et al.* [35] reported that unleached samples dissolved into the electrolyte when cycling. The poor adhesion observed in Figure 4.14 may, to a certain degree, be due to short lignin chains in the cathode material.

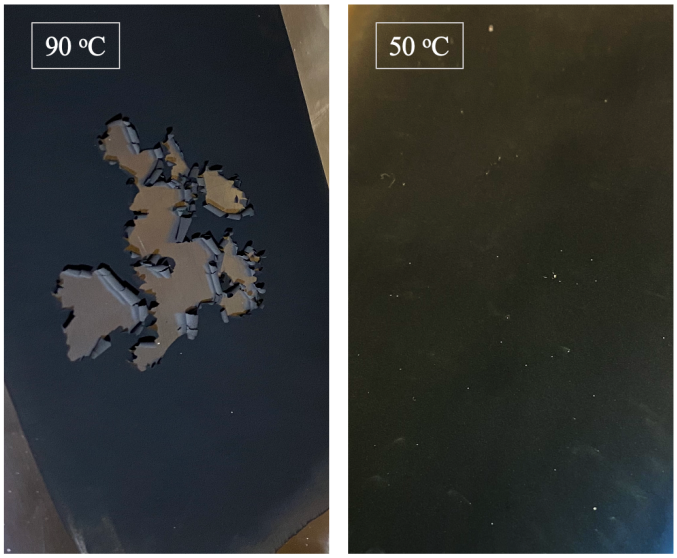

Figure 4.14: Coated surfaces dried at 90 C° and 50 C° when using lignin as binder with powder wt% ratios of 85:10:5 (NMC111:CB:Lignin), powder to NMP ratio of 1:2, coated with a raised gap of 150 μm.

Galvanostatic cycling tests from samples using pure lignin as a binder dried at 90 °C (Figure 4.15) has an initial discharge capacity of 79.1 mAh/g (C/10) that increased to 83 mAh/g (C/10) during the 3rd discharge cycle. When the C-rate increased from C/10 to C/2 between cycle 3 and 5 the discharge capacity also dropped significantly. The capacity retention was 59.3 % after 19 cycles.

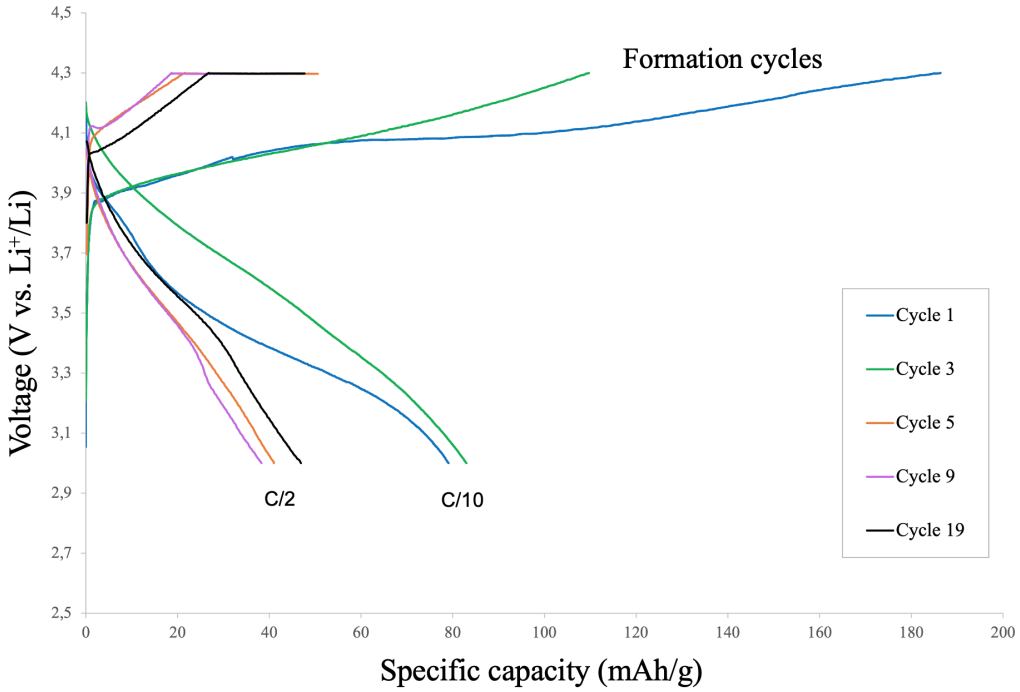

Figure 4.15: Charge/discharge plot of a coin cell using lignin as a binder with powder wt% ratios of 85:10:5 (NMC111:CB:Lignin), powder to NMP ratio of 1:2, coated with 150 μm raised gap and dried at 90 °C. The specific capacity (mAh/g) is plotted as a function of voltage (V vs. Li/Li$^+$).

In rate tests, when comparing the standard using pure PVDF binder to pure lignin binder (Figure 4.16), where both samples have a powder wt% of 85:10:5 (NMC111:CB:Binder) and P:NMP ratio of 1:2, it is clear that the drying temperature affects the performance of the LIB. The lignin sample dried at 50 °C at C-rates below C/2 performs almost as well as the standard (PVDF binder). The 90 °C sample did not perform as well, with a significant gap in specific capacity compared to the 50 °C sample. None of the lignin samples could sustain higher C-rates, where the 50 °C sample failed at >1C, and the 90 °C sample failed already at C/5.

The lignin sample dried at 50 °C (Figure 4.16) has an initial discharge capacity of 138.4 mAh/g, 140.6 mAh/g and 140 mAh/g on the 1st, 3rd and 4th cycle at C/10, respectively. When the C-rate was upped to 1C, the sample achieved a discharge capacity of 123.6 mAh/g at cycle 14. Lu *et al.* [35] achieved 148 mAh/g (C/10) and 117 mAh/g (1C) during the 4th cycle; however, the study used an LFP cathode produced with water as the solvent, which has different chemical properties than the NMC111 cathode. The study also used a different ratio with a higher wt% lignin, which often increases the electrode adhesion. The results are still comparable due to the similar practical capacities from Table 2.1 of 150 mAh/g (LFP) and 160 mAh/g (NMC111). More importantly, in Lu *et al*'s [35] study, the LFP cathodes were leached since their unleached cathodes failed due to small particles of lignin diffusing into the electrolyte.

Despite using unleached lignin as a binder, the lignin sample dried at 50°C was able to cycle. It achieved a higher capacity than the LFP cathode on the 14th cycle (1C) and a comparable capacity of 138 mAh/g (C/10) during the 1st cycle. The lower capacities (79.1 mAh/g, C/10) of the lignin sample dried at 90 °C (Figure 4.15) may indicate that short lignin chains with low MW has diffused into the electrolyte and caused the lower capacity. The lignin dried at 50 °C (Figure 4.16) might have been less affected by the lignin diffusion into the electrolyte and, therefore, achieved higher capacities. The reason for this may be that the lower temperature resulted in lower drying rates,

giving lignin with low MW time to diffuse back into the material. This would leave less lignin with low MW at the surface available to leach into the electrolyte.

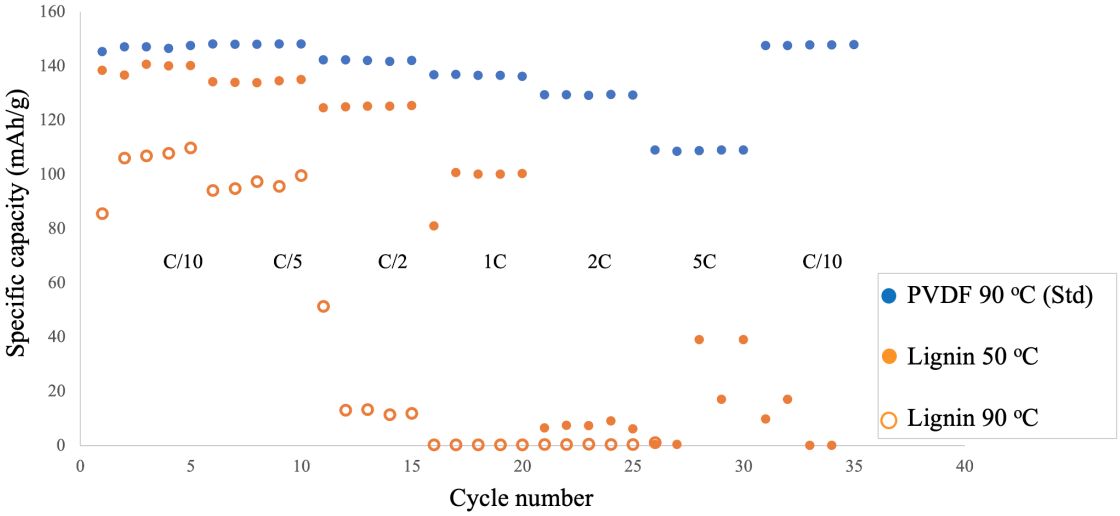

Figure 4.16: Rate test on coin cells using lignin as binder where the cathode coatings were dried at 90 °C and 50 °C, as well as the standard(PVDF binder) dried at 90 °C. All samples have a powder wt% ratio of 85:10:5 (NMC111:CB:Binder), powder to NMP ratio of 1:2 and were coated with a 150 μm raised gap. The specific capacity (mAh/g) is plotted as a function of cycle number with increasing C-rate until cycle 29, where the C-rate is set to its initial C/10.

By comparing the third cycle in Figure 4.17, the galvanostatic cycling data shows that the performance of the LIB generally decreased with increasing lignin content, with exception of the lignin sample dried at 50 °C that performed up to the standard (PVDF binder). The rate test in Figure 4.18 further confirms that an increasing lignin content decreased the overall performance of the LIB. The lignin:PVDF 1:2 ratio showed similar performance to the standard (PVDF binder) at C/10. Despite the capacity decrease with increasing C-rates, the P:NMP 1:2 ratio partially restored when the C-rate was lowered to the initial C/10.

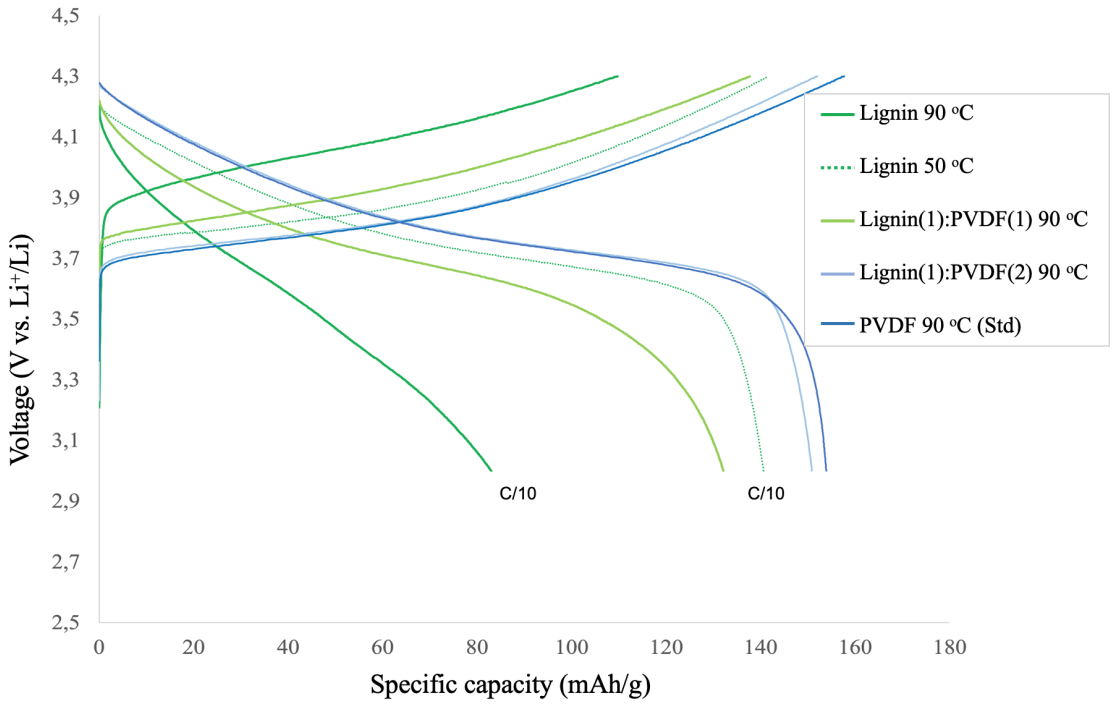

Figure 4.17: Charge/discharge plot of the 3rd cycle from coin cells with an increasing lignin content. All samples have a wt% ratio of 85:10:5 (NMC111:CB:Lignin), powder to NMP ratio of 1:2 and are coated with a 150 μm raised gap. The specific capacity (mAh/g) is plotted as a function of voltage (V vs. Li/Li$^+$)

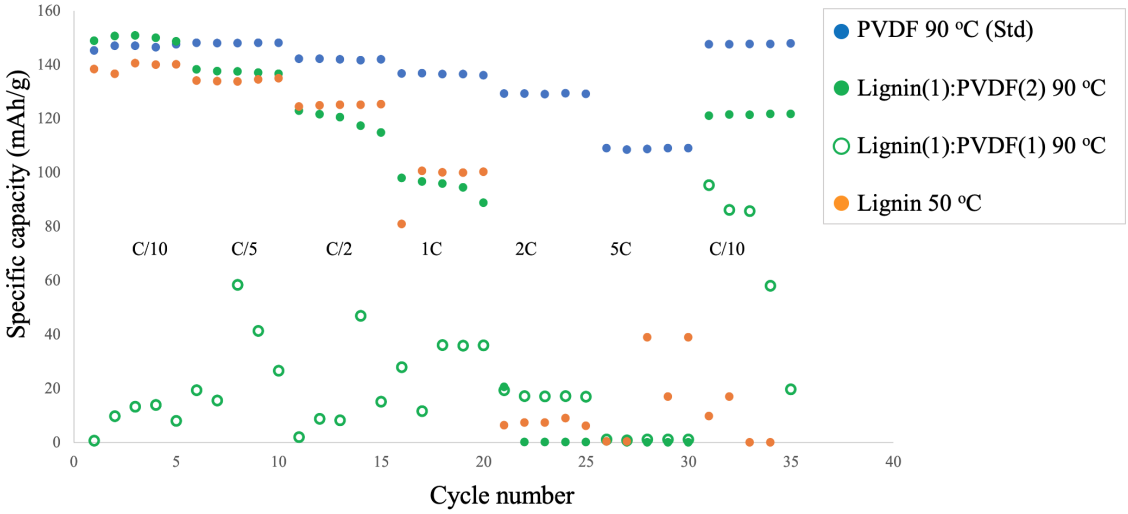

Figure 4.18: Rate test on coin cells with increasing lignin content. All samples have a wt% ratio of 85:10:5 (NMC111:CB:Binder), powder to NMP ratio of 1:2 and are coated with a 150 μm raised gap. The specific capacity (mAh/g) is plotted as a function of cycle number with increasing C-rate until cycle 29, where the C-rate is set to its initial C/10.

From scratch testing, it is observed from Figure 4.19 that calendering increases the cohesion between the Al-foil and the coating on the standard (PVDF), lignin(1):PVDF(2) and lignin(1):PVDF(1) samples. The non-calendered samples have flakes coming off from the scratch edges, indicating higher cohesion within the electrode material but low adhesion to the Al-foil. The calendered samples are not showing the same flaking tendency, which indicates that the samples increased their adhesion from calendering. All of the samples decreased both their porosity (Ap-

pendix Table A.2) and coating thickness (Table 4.1) from calendering. This reflects the theoretical background from Section 2.6, which says calendering should give lower porosity, thus increased particle-to-particle cohesion. The sample using pure lignin as a binder deteriorated completely when calendered, showing very poor adhesion between the electrode material and the Al-foil. This corresponds to Lu *et al.* [35] study where calendered samples with pure lignin as a binder in LFP electrodes experienced worsened electrode adhesion to the current collector when calendered. In general, the coatings are so mechanically weak and thin that it is challenging to measure the particle-to-particle strength through the scratch test.

Table 4.1 present the thickness and the scratch depth of the non-calendered and calendered samples. The non-calendered samples PVDF, Lignin (1):PVDF(2) and Lignin(1):PVDF(1), and all the calendered samples have a coating thickness < the deepest scratch depth, which indicates that the indenter has scratched the Al-foil. The Al-foil can be observed in the middle of the scratch (Figure 4.19). This could be avoided by utilizing a more sensitive scratching test with a lower minimum load (< 30 mN).

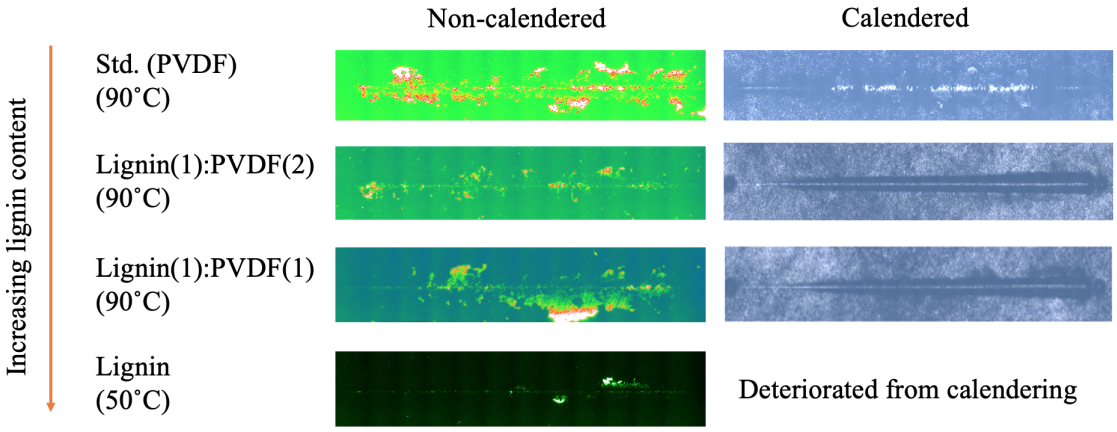

Figure 4.19: Scratch tests images of samples with increasing lignin content. The non-calendered and calendered coatings have 3.0 mm and 5.0 mm scratch and an increasing load from 30 - 200 mN and 30 - 500 mN, respectively. All samples have a powder wt% ratio of 85:10:5 (NMC111:CB:Binder), powder to NMP ratio of 1:2 and are coated with a 150 μm raised gap.

Table 4.1: Scratch tests results for the electrodes with increasing lignin content. The non-calendered and calendered cathode coatings have 3.0 mm and 5.0 mm scratch and an increasing load from 30 - 200 mN and 30 - 500 mN, respectively. Thickness is the average thickness of the cathode coating. Scratch depth is the deepest scratch at a certain length and load during the test. All samples have a powder wt% ratio of 85:10:5 (NMC111:CB:Binder), powder to NMP ratio of 1:2 and are coated with a 150 μm raised gap.

	Non-calendered				**Calendered**			
Sample	**Thickness**	**Scratch depth**	**Length**	**Load**	**Thickness**	**Scratch depth**	**Length**	**Load**
	[μm]	[μm]	[mm]	[mN]	[μm]	[μm]	[mm]	[mN]
PVDF	39.3	45.0	2.3	150	26.3	75	4.5	453
Lignin(1):PVDF(2)	45.0	55.0	2.3	150	32.0	45	5.0	500
Lignin(1):PVDF(1)	51.0	67.0	2.9	290	39.0	43.0	5.9	490
Lignin(50°C)	49.0	30.0	2.9	290	Deteriorated from calendaring			

4.1.4 Introducing water as a solvent

Since using lignin as a binder and NMP as solvent successfully managed to cycle (Figure 4.16), NMP was exchanged with water as it is nontoxic and a more sustainable choice. From Hawley

et al. [46] is it mentioned that aqueous slurries can achieve higher solid ratings than NMP-based slurries. Therefore, it was experimented with reducing the powder to water (P:W) ratios. The different ratios were visually analysed. Eventually, PA was added to the powder:water (P:W) ratio 1:1.7 to minimise corrosion on the Al-foil.

The P:W 1:2 ratio was very thin and fluid, and difficult to work with (Figure 4.20). Colour changes were observed in the area pointed out with a green arrow, and may be due to improper mixing of the powder in the water. Around the edges, the blue arrow points to areas where the surface tension of water is pulling the material in the slurry apart, leaving patches bare with no material. Material separating in the water left little area suitable for electrode cutting. Therefore, the P:W 1:2 ratio was decreased to 1:1.5. Even though the P:W 1:1.5 ratio was easier to work with than the P:W 1:2 ratio, the dried coating had many cracks, and the particles may not have been adequately mixed. This could be solved by increasing the mixing time; however, increasing the NMC111 particle's exposure time to water may lead to increased Li-leaching. Instead, the P:W ratio was increased to 1:1.7. This ratio was very liquid, making the coating process challenging. Continuous difficulties with thin and uneven coatings resulted in no useful electrodes.

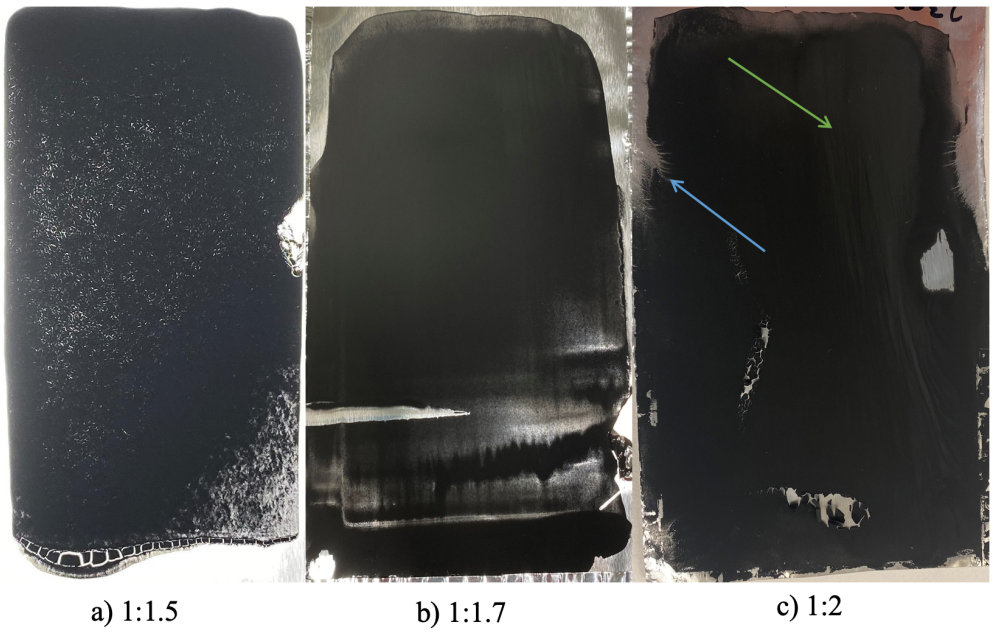

Figure 4.20: Coated surfaces using lignin as binder and water as a solvent, with a powder wt% ratio of 85:10:5 (NMC111:CB:Lignin), coated with a 150 μm raised gap and powder:water ratios of (a) 1:1.5, (b) 1:1.7, and (c) 1:2. All samples were dried in a convection oven with air velocity of 1 m/s.

The combination of the lower boiling temperature and higher vapour density of water compared to NMP leads to an increased drying rate assuming constant drying parameters. Increased drying rates results in more tension accumulating in the material in a shorter period, leading to capillary-driven crack formation. The higher drying rates also result in less back-diffusion of the binder that has migrated during the capillary drying phase. Therefore, cracking was expected when using water as a solvent and was confirmed from Figure 4.21, where both samples have the same powder to solvent ratio and drying temperature.

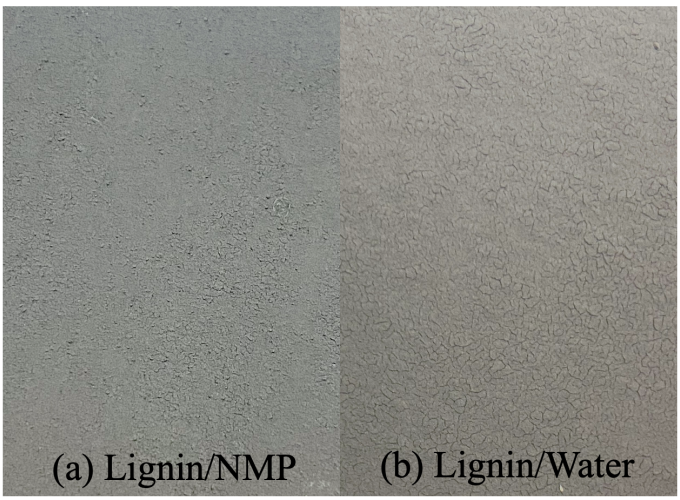

Figure 4.21: Dried coating surfaces with a powder wt% ratio of 85:10:5 (NMC111:CB:Lignin) and powder:solvent ratios of 1:1.5 with (a) NMP as solvent, coated with a 150 μm raised gap and dried at 50 °C in a vacuum oven, (b) Water as solvent, coated with a 200 μm raised gap and dried in a convection oven at 50 °C and 0.5 m/s.

Adding PA

A slurry with a powder to water ratio (P:W) of 1:1.7, lignin as binder (Lignin/Water) and powder wt% ratio of 85:10:5 (NMC111:CB:Lignin) had an initial pH of 11.2 (Table 4.2). According to Bauer *et al.* [45], a pH between 9 - 10 indicates the ideal compromise between corrosion on the Al-foil and Li-leaching. Therefore, PA was added to the slurry to lower the pH, and thus minimise corrosion. With a final slurry pH of 8.3, the slurry was within the stability window of the Al-foil, but the NMC particles may have experienced significant Li-leaching, as indicated by Bauer *et al.* [45]. The mixing time and heat treatment may not be sufficient to make a protective Li_3PO_4 - coating on the NMC particles to limit Li-leaching.

Table 4.2: The effect on pH when introducing PA to slurry with a powder to water ratio of 1:1.7, powder wt % of ratio is 85:10:5 (NMC111:CB:Lignin) and coated with a 200 μm raised gap.

Sample	**pH**		
	Slurry	**PA- solution**	**Slurry with PA**
Lignin/Water-PA	11.2	1.61	8.3

The scratch tests of both dried non-calendered and calendered Lignin/Water-PA samples (Figure 4.22) with wet slurry pH of 8.3 showed clean scratch lines with no visible flaking. This indicates that both samples had good adhesion to the current collector. The results contradict earlier findings by Bauer *et al.* [45], where they saw lower adhesion between the current collector and the electrode material when the pH was lowered to 9 - 10. They presumed the drop in adhesion at the interface was caused by acid accumulating there, which may not be the case for these samples. Kazzazi *et al.*[48] found, independent of utilized binder, that the addition of PA led to a reduced amount of cracks and Al corrosion when the pH was lowered from 9.9 to 7.7. Reduced amounts of cracks and Al corrosion could be the reason for the good adhesion when adding PA compared to the sample also using pure lignin in Figure 4.19.

From Table 4.3 the scratch depth on both the non-calendered and the calendered sample surpassed the thickness of the electrode material and the Al-foil at the end of the scratch test. Therefore, the last part of the scratch should not be considered when evaluating the results. Optimally, the scratch test should be done with a lower load to avoid scratching of the Al-foil. The non-calendered sample had a greater thickness than the calendered sample because the electrodes were cut from different areas of the coating (Table 4.3).

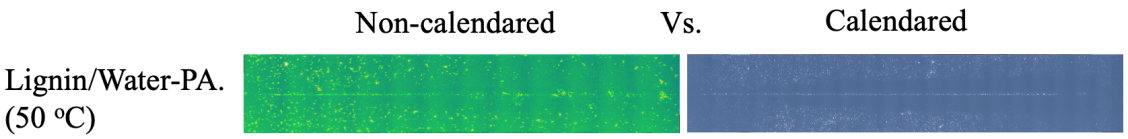

Figure 4.22: Scratch test images on samples using lignin as binder, water as solvent and PA as pH controller. The non-calendered and calendered coatings have a 3.0 mm and 5.0 mm scratch and an increasing load from 30-200 mN and 30-500 mN, respectively. All samples have a powder wt% ratio of 85:10:5 (NMC111:CB:Lignin), powder to water ratio of 1:1.7 and are coated with a 200 μm raised gap.

Table 4.3: Scratch test results on samples using lignin as a binder and PA as a pH controller. The non-calendered and calendered cathode coatings have a 3.0 mm and 5.0 mm scratch and an increasing load from 30-200 mN and 30-500 mN, respectively. Thickness is the average thickness of the cathode coating. Scratch depth is the deepest scratch at a certain length and load during the test. All samples have a wt % powder ratio of 85:10:5 (NMC111:CB:lignin), powder to water ratio of 1:1.7 and coated with a 200 μm raised gap.

	Non-calendered				**Calendered**			
Sample	**Thickness**	**Scratch depth**	**Length**	**Load**	**Thickness**	**Scratch depth**	**Length**	**Load**
	[μm]	[μm]	[mm]	[mN]	[μm]	[μm]	[mm]	[mN]
Lignin/Water-PA	35	63	2.65	180	46	110	5	500

4.2 Convection drying

To increase the efficiency of the drying process in terms of time and energy consumption, different temperatures and air velocities were tested when drying the samples listed in Table 4.4 in the convection oven (Figure 2.9). The goal of this was to examine how the drying parameters affected the final cathode in terms of adhesion strength and cracking. The raised gap was increased from the 150 μm used in Section 4.1 to 200 μm to allow larger amounts of solvent for evaporation, in order to see clearer trends in the drying. Uneven coating thickness and geometry may have caused uneven drying rates across the coatings. This was a problem throughout the experimental work.

Table 4.4: Slurry and drying parameters used while drying in the convection oven. All samples in the experiments had a 85:10:5 wt% (NMC111:CB:binder) ratio. P:S denotes powder to solvent wt% ratio.

P:S	**Drying temp.[°C]**	**Air velocities [m/s]**	**Binder/solvent**
1:2	Room temp.	0	PVDF/NMP
1:2	50	1	PVDF/NMP
1:2	90	1	PVDF/NMP
1:2	150	1	PVDF/NMP
1:2	150	0.5	PVDF/NMP
1:2	150	0.5	Lignin/NMP
1:2	50	0.5	lignin/Water
1:1.7	50	0.5	lignin/Water
1:1.5	50	0.5	lignin/Water

4.2.1 NMP/PVDF

From Figure 4.23, it is clear that increasing temperatures will reduce the drying time. By increasing the temperature from 50 °C to 90 °C the drying time was reduced by 77% (from ∼ 3900s to 900s). Further increasing the temperature from 90 °C to 150 °C reduced the drying time by 44% (from ∼ 900s to 500s). When considering the economical aspect, the lowered temperature is unlikely to compensate for the increased drying time.

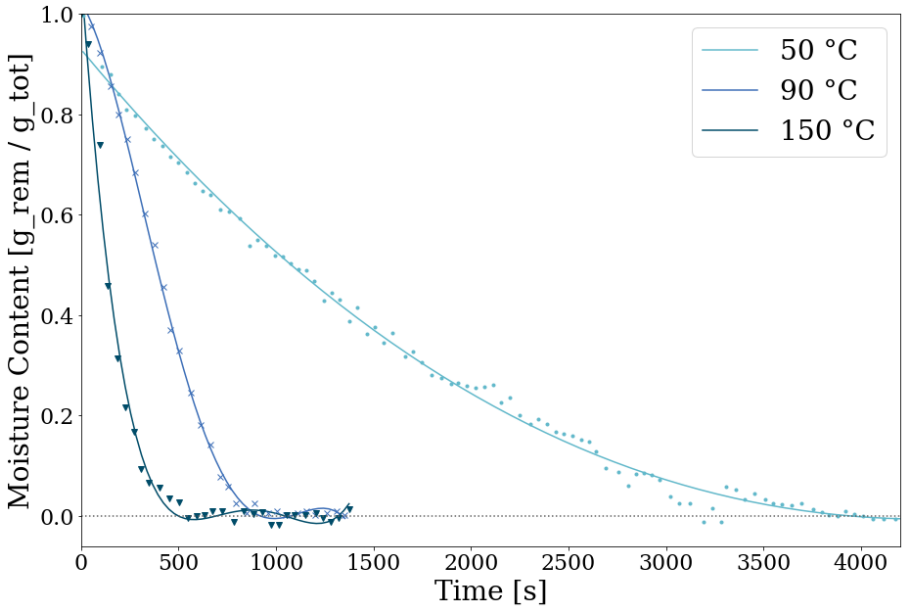

Figure 4.23: Moisture content as a function of time on samples dried at various temperatures in the convection oven with an air velocity of 1 m/s. All samples have powder to NMP ratio of 1:2 with, powder wt% ratio of 85:10:5 (NMC111:CB:PVDF), coated with a 200 μm raised gap. Moisture content is measured by grams of the remaining moisture divided by total moisture used in the coating. Symbols represent the actual measuring whereas the solid line is the best fitted polynomial to the symbols.

Different drying air velocities when drying a standard sample at 150 °C did not affect the drying time as shown in Figure 4.24. After decreasing the air velocity from 1 m/s to 0.5 m/s both curves indicate dry state at ∼ 500 s. The Reynolds number was calculated using Equation 2.10 to Re = 5269 for 1 m/s and indicates a turbulent airflow and Re = 2635 for 0.5 m/s which is a transitioning airflow. Presumably a more laminar air flow would constitute a gentler drying, while a more turbulent air flow would give more uneven temperatures across the surface. It is therefore likely that the higher air velocity is tougher on the sample. Inspecting the curves, they look different despite the coatings reaching dry state simultaneously. With higher air velocity it seems the heating phase (first phase) is skipped, while the evaporation phase (second phase) is short. The third phase makes up more than half of the total drying time, which presents great opportunities for improvement. With lower air velocity, the three phases of drying are easily identifiable, and the third phase is short, relative to the curve for the higher air velocity.

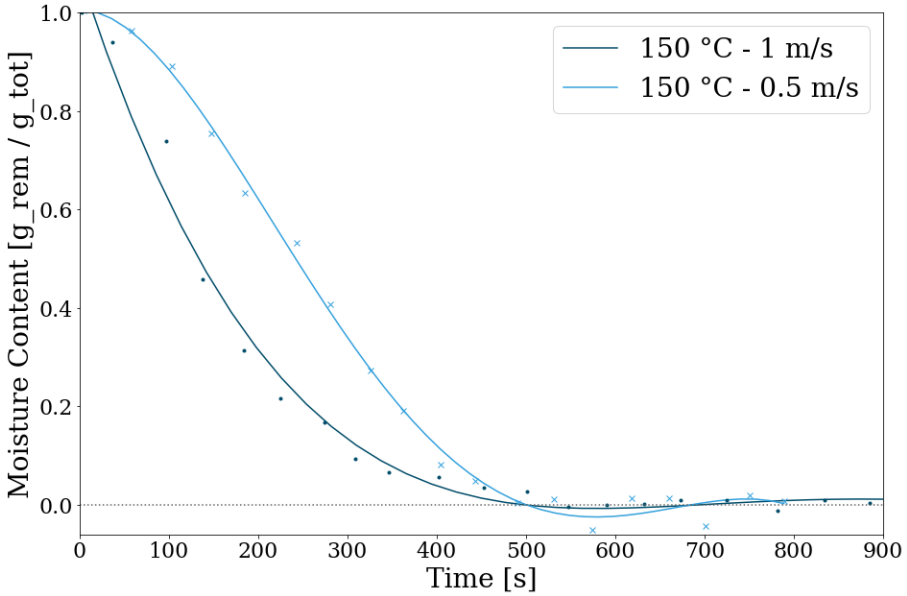

Figure 4.24: Moisture content as a function of time on samples dried with various air velocity in the convection oven. All samples have powder to NMP ratio of 1:2, powder wt% ratio of 85:10:5 (NMC111:CB:PVDF), coated with a 200 μm raised gap. Moisture content is measured by grams of the remaining moisture divided by total moisture used in the coating. Symbols represent the actual measuring whereas the solid line is the best fitted polynomial to the symbols.

A "worst case scenario" in terms of time efficiency was tested where the standard sample was dried in room temperature ($\sim$ 22 °C) without additional air flow over two days, see Figure 4.25. The moisture content curve started to flatten after around 48h, and the cathode could be considered dry. This drying procedure has the lowest energy impact compared to samples presented in Figure 4.23 and 4.24. The toxic NMP requires a large amount of heated air to keep the concentration far below the flammability level. The long drying process means an increased volume of air that requires NMP recovery. The increased energy consumption from the recovery step may exceed the energy saved by drying at a lower temperature. Therefore, the lowered temperature is not necessarily more energy effective than drying at higher temperatures.

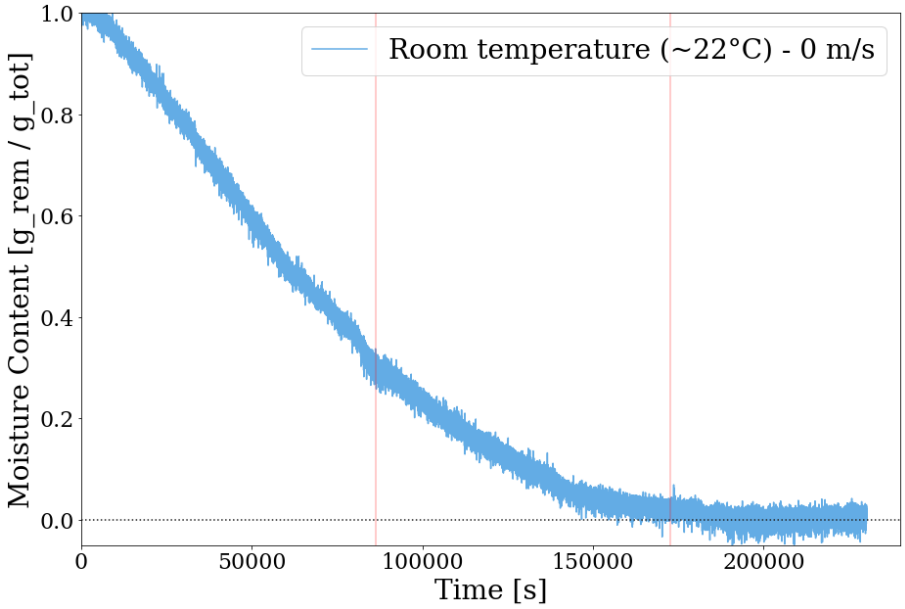

Figure 4.25: Moisture content as a function of time on samples dried in room temperature ($\sim$ 22 °C), no extra airflow. The pink lines represent 24 hours. Powder to NMP ratio of 1:2 with, powder wt% ratio of 85:10:5 (NMC111:CB:PVDF), coated with a 200 μm raised gap. Moisture content is measured by grams of the remaining moisture divided by total moisture used in the coating. All measurements were plotted as there was no drying interval used.

The drying process can generally be divided into three stages; in the initial heating phase the slurry is heated until the solvent reaches the evaporation temperature. This phase can be observed clearly at the start of the drying curve for 90 °C in Figure 4.23, for 150 °C - 0.5 m/s in Figure 4.24, and for room temperature in Figure 4.25. The second drying phase is characterised by a constant evaporation rate, seen as a constant slope in all curves in Figure 4.23, 4.24 and 4.25. Here, the bulk of the solvent evaporates from the material. The curve flattens as the drying process moves into the third phase, where the remaining solvent is emptied from smaller capillary pores, as described in Section 2.5.2. The third phase is especially prevalent for samples dried in gentler conditions (Figure 4.25 at ~22 °C). It can also be observed in the drying curves of 90 °C and 150 °C in Figure 4.23, as well as both drying curves in Figure 4.24. The falling rate period is often a relatively time consuming step compared to amount of solvent removed. This becomes especially clear looking at Table 4.5 where there drying time of the third phase is compared to the solvent reduction as percentages of total drying time and solvent reduction, respectively.

Table 4.5: Solvent reduction in the third drying phase as percentage of total amount of solvent removed. All samples has a powder 85:10:5 wt% (NMC111:CB:Binder) ratio and powder to solvent ratio of 1:2.

Sample	**Drying time [% of tot]**	**Solvent reduction [% of tot]**	**Ref Figure**
$\sim$ 22 °C - 0 m/s	30	6	4.25
50 °C - 1 m/s	N/A	N/A	4.23
90 °C - 1 m/s	16	3	4.23, 4.26
90 °C - 1 m/s (2)	53	14	4.26
150 °C - 1 m/s	44	12	4.23, 4.24
150 °C - 0.5 m/s	19	11	4.24

To validate the accuracy of the convection oven, the reproducibility was investigated. As the sample dried at 90 °C had the most desirable surface (Figure 4.26) compared to the 50 °C and 150 °C sample, a parallel sample was made and dried under the same conditions. As shown in Figure

4.26, it was reproducible with some deviation. By comparing the slope numbers of the curves the standard deviation for each curve was calculated. With a 95% confidence interval the first (blue) had 60% accuracy, whereas the second (purple) had 54% accuracy. The deviation is believed to be due to difference in the geometry of the samples, and uneven coating thickness.

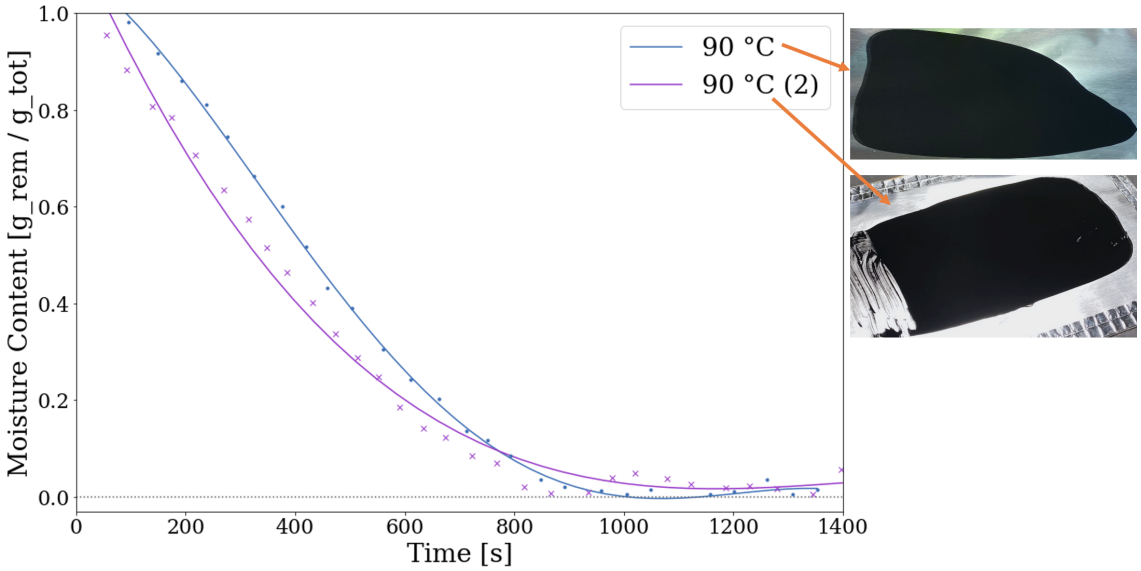

Figure 4.26: Reproducibility of two standard coatings dried at 90°C with an air velocity of 1.0 m/s. Powder to NMP ratio of 1:2, powder wt% ratio of 85:10:5 (NMC111:CB:PVDF), coated with a 200 μm raised gap. Moisture content is measured by grams of the remaining moisture divided by total moisture used in the coating. Symbols represent the actual measuring whereas the solid line is the best fitted polynomial to the symbols.

To summarise, the coatings experienced faster dying with increased temperature. The different air velocities did not affect the drying time, but did affect the shape of the drying curve. The lowest energy impact of drying is achieved when the cathode is left to dry in room temperature, but this drying procedure is likely not more environmentally friendly considering the added energy consumption from the recovery step. The parallel samples showed some deviation, assumed to be due to unequal geometry and uneven coating thickness. The lack of standardised geometry is an issue for the reproducibility of all the drying curves, and should be mended in future experiments.

4.2.2 Cracking

Cracking analyses were completed on the samples from Section 4.2, where the coatings were dried with varying temperature and air velocity, using the standard powder to NMP (P:NMP) ratio of 1:2 with a powder wt% ratio of 85:10:5 (NMC111:CB:PVDF). From SEM images, the area and crack length was analysed using ImageJ software. In Figure 4.27 the blue area is the crack area, whereas the yellow lines are the crack lengths, with the calculated values presented in Table 4.6. The most gentle drying parameters show the least cracks on the surface.

The coating dried in a vacuum oven at 90°C overnight (Figure 4.27) had the lowest mean value for the crack length (66 µm) and crack area (356 µm^2) compared to the coatings dried in the convection oven (Table 4.6). According to Li *et al.* an increased drying velocity can lead to capillary driven crack formation due to quicker evaporation and tension accumulation. Therefore, it was expected that the coatings dried at low temperatures and air velocities would be less affected by cracks. Oppositely, the 50 °C - 1 m/s coating had the largest mean crack length (192 µm) and area (2135 µm^2). The coating dried at 90 °C - 1 m/s, had a mean crack length and area of 93 µm and 585 µm^2, respectively. When the temperature increased to 150°C - 1 m/s, the mean crack length increased to 170 µm, and the mean crack area decreased to 468 µm^2, compared to the 90 °C - 1

m/s. Since the deviation between 90 °C - 1 m/s and 150 °C - 1 m/s is small and the results only represent a small part of the cathode area, it is challenging to determine the true effect of increased temperature. The average crack length and area of the 50 °C - 1 m/s coating might have looked different if the entire surface area was analysed.

By decreasing the air velocity from 1.0 m/s to 0.5 m/s for the coating dried at 150 °C the mean crack length decreased from 170 µm to 70 µm and the mean crack area from 468 µm^2 to 213 µm^2. The 150 °C-0.5m/s coating had the lowest crack length and cracked area out of all the coatings dried in the convection oven, indicating that the air velocity has a larger effect on cracking than the temperature.

Table 4.6: Estimated crack length and crack area on cathode coatings dried with various temperatures and air velocities in the convection oven. Image J software is used to obtain information from the SEM images. All samples have a wt% of 85:10:5 (NMC111:CB:PVDF) and powder to NMP ratio of 1:2.

Temperature	**Air velocity**	**Length** [μm]			**Area** [μm^2]		
[°C]	[m/s]	Min	Max	Mean	Min	Max	Mean
90	0	23	172	66	73	1949	356
50	1.0	27	519	192	167	5570	2135
90	1.0	30	179	93	87	1984	585
150	0.5	21	181	70	42	711	213
150	1.0	52	518	170	112	2066	468

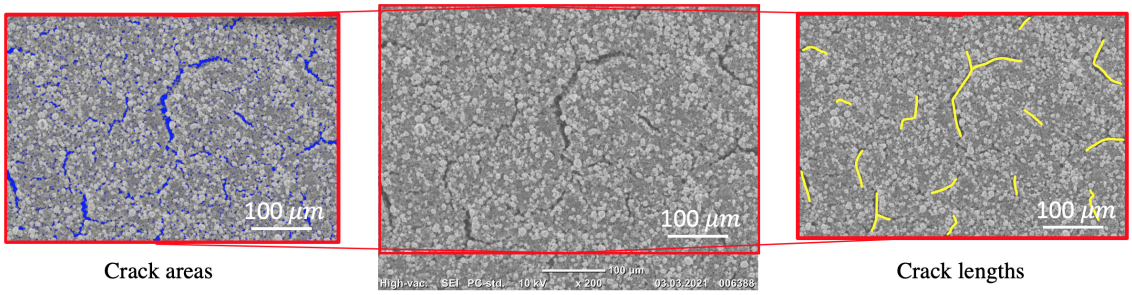

(a) Vacuum, 90°C (20h)

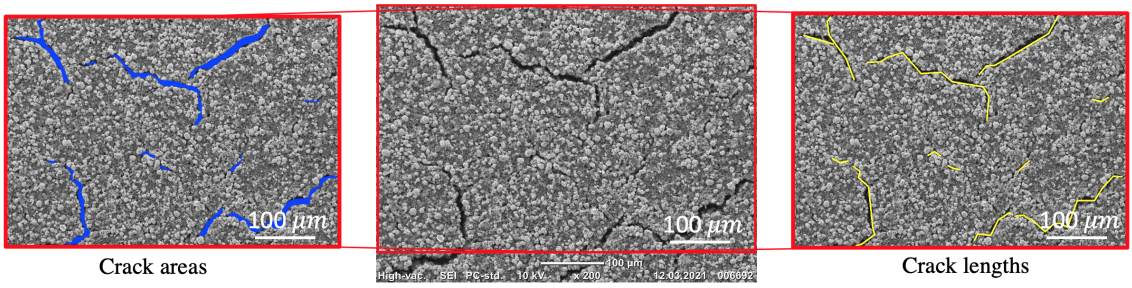

(b) Convection, 50°C - 1 m/s

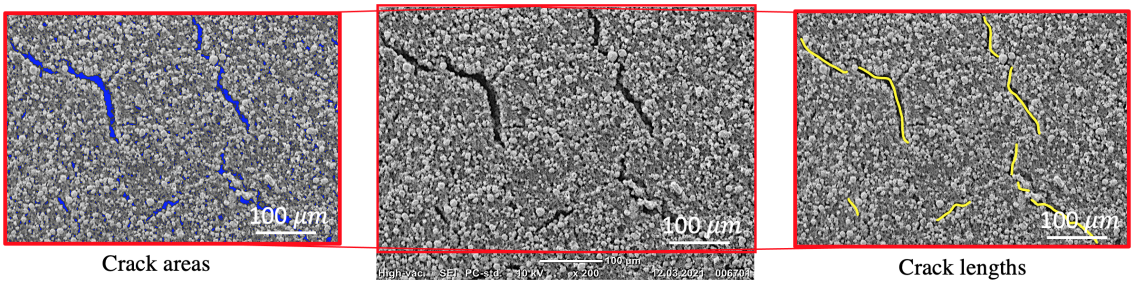

(c) Convection, 90°C - 1 m/s

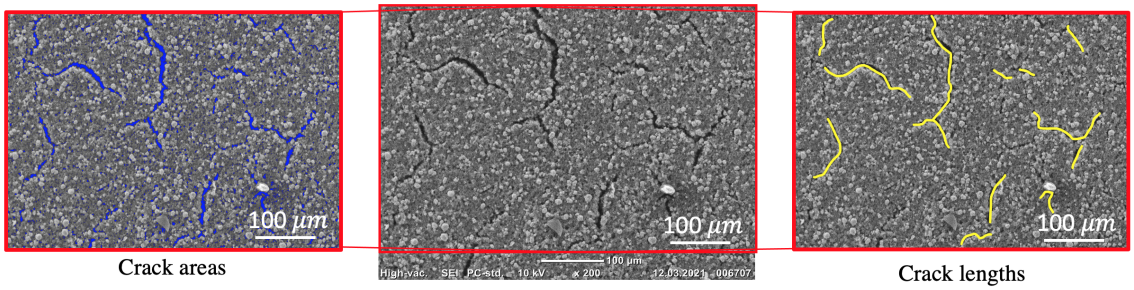

(d) Convection, 150°C - 0.5 m/s

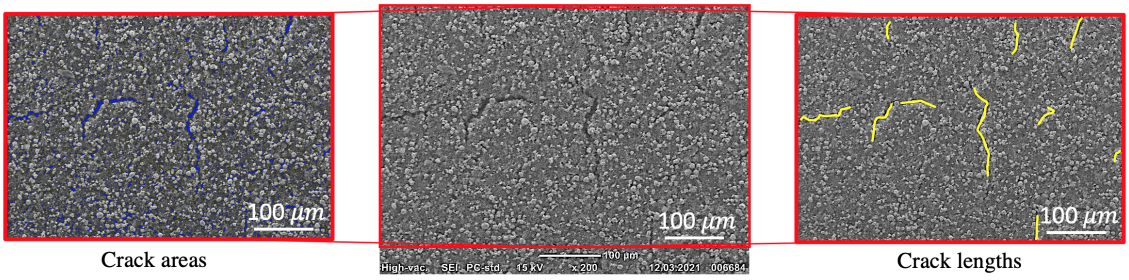

(e) Convection, 150°C - 1 m/s

Figure 4.27: SEM images of crack area (blue areas) and crack length (yellow lines) on samples dried with various temperatures and air velocities. All samples have a wt% of 85:10:5 (NMC111:CB:PVDF) and powder to NMP ratio of 1:2. Images are analysed using the ImageJ software.

4.2.3 Scratch

Scratch tests were completed on non-calendered and calendered samples, where samples were dried with varying temperatures and air velocity. Samples were made with the standard powder to NMP (P:NMP) ratio of 1:2 with a powder wt% ratio of 85:10:5 (NMC111:CB:PVDF). From Figure 4.28 it is observed that the sample dried at room temperature (0 m/s) and the samples dried at 90 °C (1 m/s) and 150 °C (1 m/s) had good adhesion within the cathode particles and to the Al-foil for both the non-calendered and calendered samples. A clear, increasing tendency between extreme drying conditions and adhesion was expected to be observed, but the authors have been unable to identify it.

The calendering was expected to improve adhesion between the electrode material and Al-foil, as was observed in the scratch tests done on samples with increasing lignin content (Figure 4.18). The sample dried at 50 °C with an air velocity of 1 m/s had bad adhesion to the Al-foil, as can be observed from the cathode material flaking off from the scratch edges on both the calendered and the non-calendered sample in Figure 4.28. From the first glance at the scratches it may look like the flaking starts at the same point in the scratches, however the scratch for the calendered sample is longer, with higher load. The flaking starts at $\sim$ 250mN, while in the non-calendered sample, the flaking starts at $\sim$ 90 mN. As such, calendering has improved adhesion for these samples as well. The large flakes indicate good cohesion within the electrode material.

From Table 4.7 all calendered samples have reached the thickness of the sample and the Al-foil at the end of the scratch test, therefore the last part of the scratch should not be considered when evaluating the test. This is not the case for the non-calendered samples with the exception of the 150 °C - 1 m/s sample, therefore the 30 - 200 mN load with a 3.0 mm scratch seem like more optimal scratch parameters than the 30 - 500 mN load with the 5.0 mm scratch length.

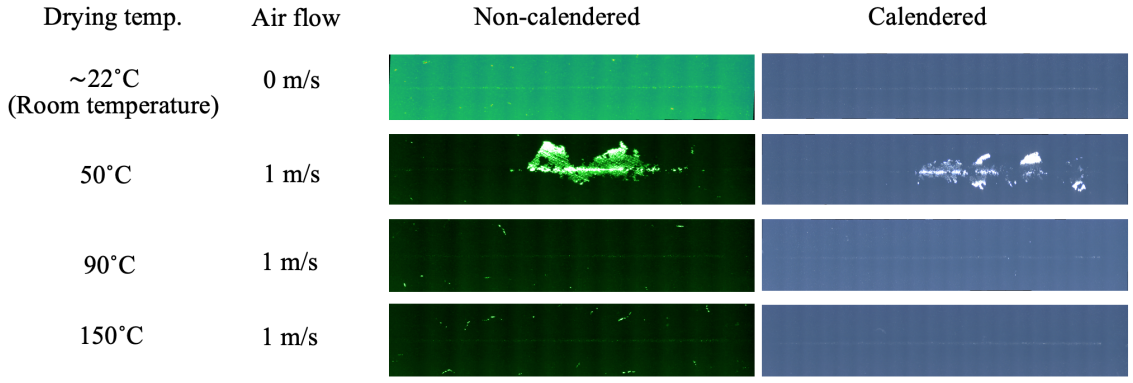

Figure 4.28: Scratch test images from samples with increasing drying temperature in the convection oven. The non-calendered and calendered cathode coatings have 3.0 mm and 5.0 mm scratch and an increasing load from 30 - 200 mN and 30 - 500 mN, respectively. All samples have a wt% ratio of 85:10:5 (NMC111:CB:PVDF), powder to NMP ratio of 1:2 and are coated with a 200 μm raised gap

Table 4.7: Scratch test results from samples with increasing drying temperature in the convection oven. The non-calendered and calendered coatings have 3.0 mm and 5.0 mm scratch and an increasing load from 30 - 200 mN and 30 - 500 mN, respectively. Thickness is the average thickness of the cathode coating. Scratch depth is the deepest scratch at a certain length and load during the test. All samples have a wt% ratio of 85:10:5 (NMC111:CB:PVDF), powder to NMP ratio of 1:2 and are coated with a 200 μm raised gap

		Non-calendered				**Calendered**			
Drying temp.	**Air flow**	**Thickness**	**Scratch depth**	**Length**	**Load**	**Thickness**	**Scratch depth**	**Length**	**Load**
°C	[m/s]	[μm]	[μm]	[mm]	[mN]	[μm]	[μm]	[mm]	[mN]
22	0	63	65	2.8	200	48	52.5	4.75	470
50	1.0	70	45	3.0	200	50	55	5	500
90	1.0	70	53	2.3	150	58	130	4.5	453
150	1.0	57	59.0	2.8	190	50	90	5	500

4.2.4 Binder migration

The sample dried at 50 °C with an air velocity of 1 m/s (Table 4.5) had longer drying time (Figure 4.23), poor adhesion in the scratch test and more cracks than the 90 °C - 1 m/s and 150 °C - 1 m/s and 150 °C - 0.5 m/s samples (Figure 4.27 and Table 4.6). Therefore, binder migration was investigated through an EDS analysis of the 50°C - 1 m/s sample. The potential presence of agglomerations of CB and NMC111 particles was investigated. The EDS analyses were executed by MSc student Armin Kahrom.

The PVDF binder can be observed as a relatively even distribution of fluoride in Figure 4.29. Dark areas are observed on the underside of the particles. The dark areas may be areas where the binder has migrated from, but since they are concentrated on the underside of the particles, they are most likely caused by the shadow effect. A solution to avoid the shadow effect could be to cut the coating using a focused electron beam (FIB).

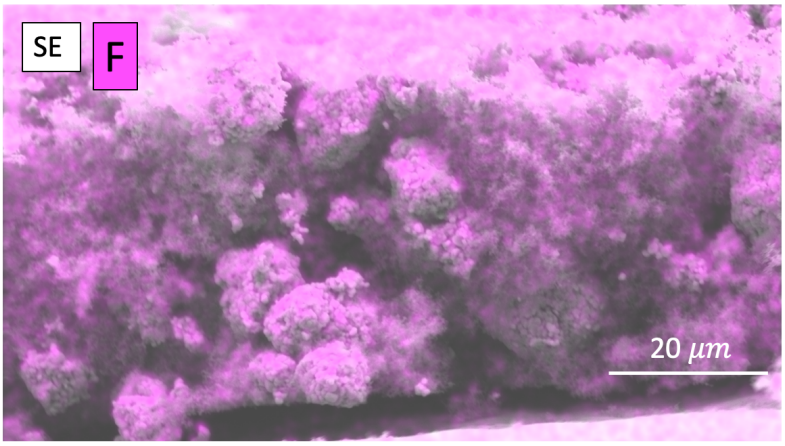

Figure 4.29: SEM image of coating cross section where PVDF binder is traced as fluoride (pink) through EDS analysis. The sample is dried at 50 °C with an air velocity of 1 m/s. Standard powder to NMP ratio of 1:2 with, powder wt% ratio of 85:10:5 (NMC111:CB:PVDF), coated with a 200 μm raised gap.

In order to ensure good electrical conductivity through the electrode the CB should be evenly distributed within the cathode material. From Figure 4.30 some agglomeration of the CB can be observed as grey areas in the center of the cross section. This leaves areas in the electrode with higher transfer resistance, which could decrease the efficiency of the LIB.

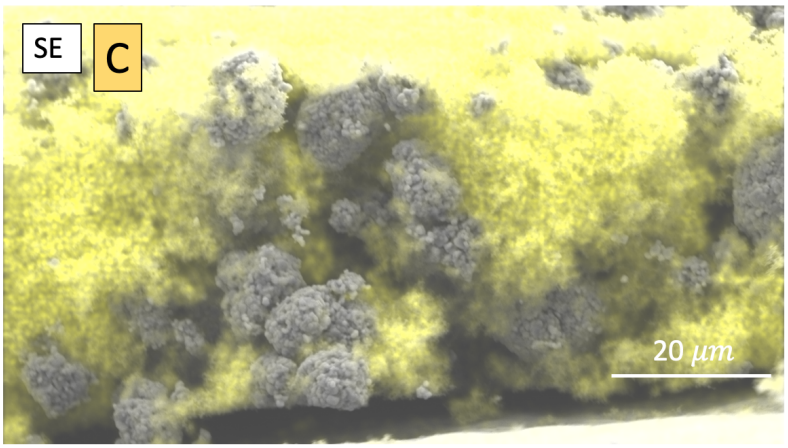

Figure 4.30: SEM image of coating cross section where CB is traced as carbon (yellow) through EDS analysis. The sample is dried at 50 °C with an air velocity of 1 m/s. Standard powder to NMP ratio of 1:2 with, powder wt% ratio of 85:10:5 (NMC111:CB:PVDF), coated with a 200 μm raised gap.

The active material (AM) $LiNi_{1/3}Mn_{1/3}Co_{1/3}O_2$ (NMC111) consists of equal amounts of Ni, Mn and Co, which is confirmed through EDS analyses in Figure 4.31a, 4.31b and 4.31c. The AM also consists of oxygen as shown in Figure 4.31d. Lithium was not traced through this analysis, but should still be present in the electrode material. Figure 4.31 shows that the AM is evenly distributed throughout the coating.

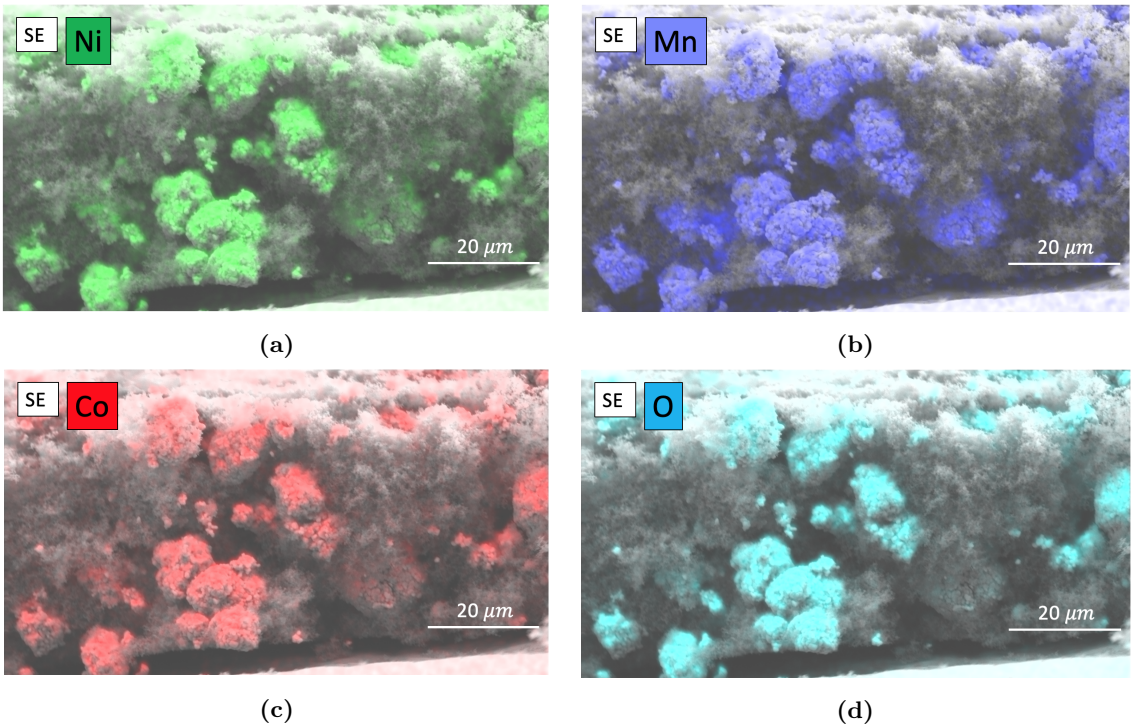

Figure 4.31: SEM image of coating cross section where the $LiNi_{1/3}Mn_{1/3}Co_{1/3}O_2$ (NMC111) is traced as (a) Nickel, (b) Manganese, (c) Cobalt, (d) Oxygen through EDS analyses. The sample is dried at 50 °C with an air velocity of 1 m/s. Standard powder to NMP ratio of 1:2 with, powder wt% ratio of 85:10:5 (NMC111:CB:PVDF), coated with a 200 μm raised gap.

4.3 Lignin as a binder

Introducing lignin as a binder with NMP as solvent was first completed in Section 4.1.3. Further attempting to increase drying efficiency a sample was dried at 150 °C with an air velocity of 0.5 m/s. The same drying conditions were also used on a PVDF sample to investigate how lignin would affect the drying time.

Exchanging PVDF with lignin as a binder when drying at 150 °C and using NMP as solvent did not affect the drying time, as shown in Figure 4.32. The heating phase (phase 1) may be $\sim$ 50 s shorter for the lignin sample. Similar to earlier observations when using lignin as a binder (Figure 4.15), the sample experienced poor adhesion between the electrode material and the Al-foil compared to the sample using pure PVDF as a binder. This is observed in Figure 4.32, where the electrodes have been cut from the cathode material, and flaking around the edges is significantly more pronounced in the lignin sample. Despite this, the lignin sample dried at 150 °C with an air velocity of 0.5 m/s did not flake in the middle of the coating as it did when dried at 90 °C in a vacuum oven (Figure 4.14). This may indicate that 90 °C in a vacuum for a 150 μm coating dried over night is a rougher treatment than 150 °C at 0.5 m/s for a 200 μm sample dried for $\sim$ 500 s.

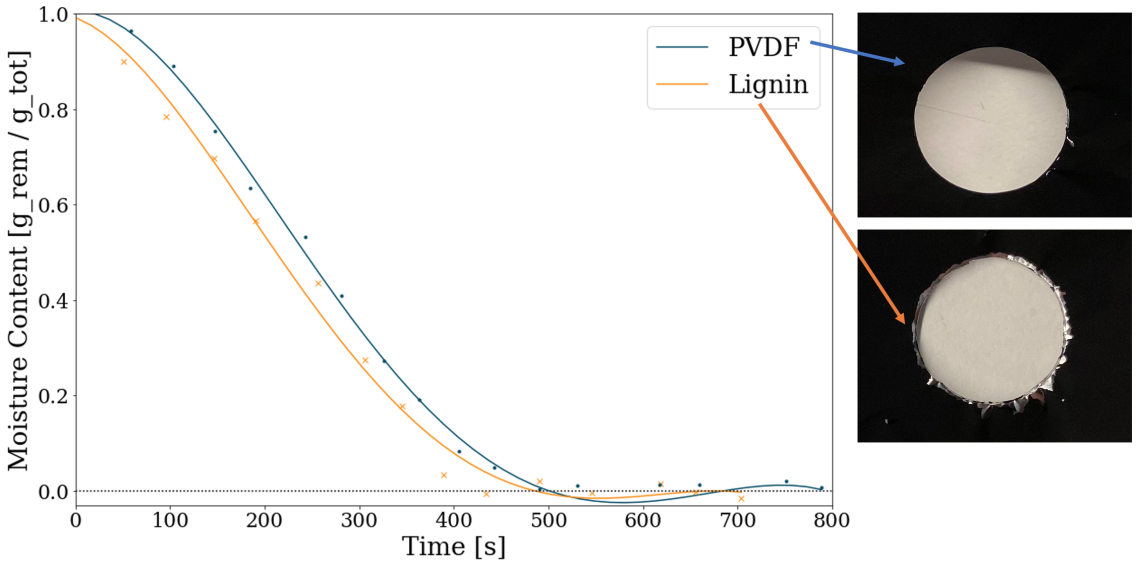

Figure 4.32: Moisture content as a function of drying time on samples using pure PVDF binder and pure lignin binder dried in the convection oven with an air velocity of 0.5 m/s at 150 °C. The arrows point at the coating surface where the electrodes has been cut out. Both samples had a powder to NMP ratio of 1:2, powder wt% ratio of 85:10:5 (NMC111:CB:Binder) and coated with a 200 μm raised gap. Moisture content is measured by grams of the remaining moisture divided by total moisture used in the coating. Symbols represent the actual measuring whereas the solid line is the best fitted polynomial to the symbols.

4.3.1 Water as solvent

As concluded in Section 4.3 exchanging PVDF with lignin did not affect the drying time significantly when using NMP as solvent. Therefore, it would be interesting to see how exchanging NMP with water as solvent affect the drying parameters. Water is a more sustainable choice as it is not toxic, and the recovery step for NMP is unnecessary. The coatings were dried at 50 °C as coatings with pure lignin binder and NMP as solvent dried in a vacuum oven (0 m/s) showed best results at this temperature (Section 4.1.3). Continuing on the wt% ratio of 85:10:5 (NMC111:CB:Lignin), the powder to water (P:W) ratios were varied. The samples in this section have been presented in Section 4.1.4.

The reduction in moisture content as a function of time for the samples with P:W ratio of 1:2, 1:1.7

and 1:1.5 are shown in Figure 4.33. The symbols represent the actual measuring whereas the solid line in the best fitted curve. The samples with P:W of 1:1.7 and 1:2 had a wide spread of symbols which indicates varying evaporation rates. This is likely due to the uneven coating thickness which according to Hawley *et al.* [46] may be due to a thin slurry. Uneven coating thickness on the Al-foil left thinly coated areas that experienced quicker drying, and thicker coated areas that experienced slower drying. The measuring of P:W 1:1.5 showed little deviation between the symbols and their respective curve, indicating steady evaporation.

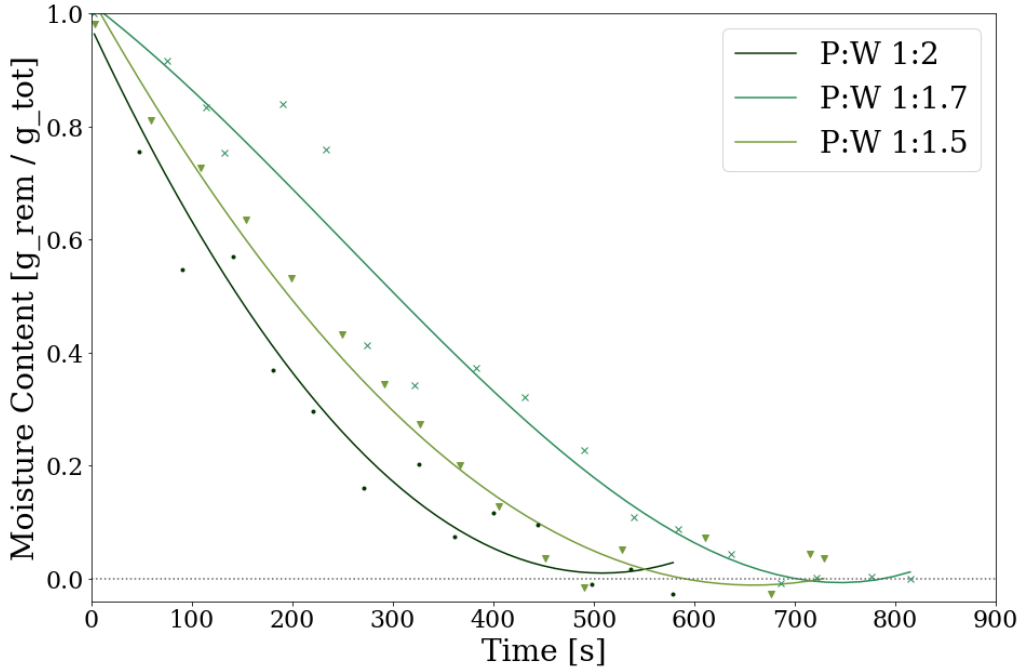

Figure 4.33: Moisture content as a function of drying time when using lignin as binder, water as solvent and varying powder to water (P:W) ratios dried in an convection oven with an air velocity of 0.5 m/s at 50 °C. All samples had a powder wt% ratio of 85:10:5 (NMC111:CB:Lignin), coated with a 200 μm raised gap. Moisture content is measured by grams of the remaining moisture divided by total moisture used in the coating. Symbols represent the actual measuring whereas the solid line is the best fitted polynomial to the symbols.

A parallel of the P:W 1:1.7 sample was made to investigate the reproducibility of the results. This P:W ratio was chosen as the previous coating appeared the most optimal based on visual inspection of the dried coatings. The drying curves of the parallels are presented in Figure 4.34 with their respective coatings. The curves deviate from each other from the start, and have different steepness throughout the plot. The endpoint of the curves differentiate by 200s. With a 95% confidence interval the first (green) had 9% accuracy, whereas the second (purple) had 5% accuracy. The low accuracy of both curves shows low to no signs of reproducibility. This may be due to the slurry being too thin from the beginning, leading to an uneven coating thickness. The uneven coating thickness of the cathode material can be observed in Figure 4.34.

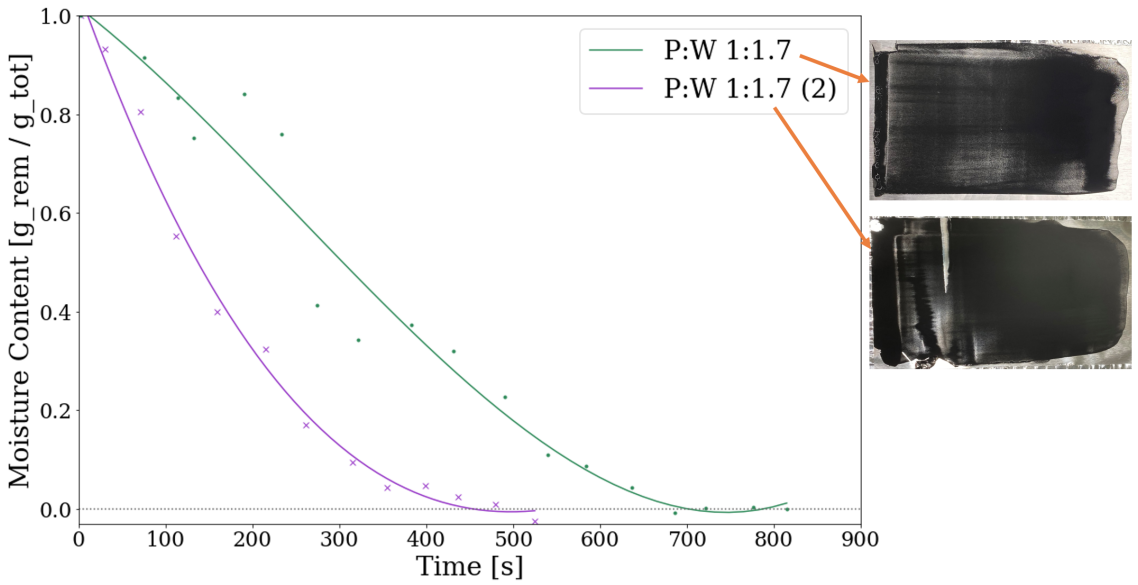

Figure 4.34: Reproducibility of two standard coatings dried at 90°C with an air velocity of 1.0 m/s. Powder to water (P:W) ratio of 1:1.7, powder wt% ratio of 85:10:5 (NMC111:CB:Lignin), coated with a 200 μm raised gap. Moisture content is measured by grams of the remaining moisture divided by total moisture used in the coating. Symbols represent the actual measuring whereas the solid line is the best fitted polynomial to the symbols.

The solvent reduction in the third phase for drying curves presented in this sample can be observed in Table 4.8. The third phase makes up a larger percentage of drying time compared to solvent reduction for water/lignin samples, similar to what was observed for NMP/PVDF samples. There are no clear indications that exchanging binder or solvent has any impact on the percentage-wise energy intensity of the third drying phase.

Table 4.8: Solvent reduction in the third drying phase as percentage of total amount of solvent removed. All samples had a powder 85:10:5 wt% (NMC111:CB:Binder), P:S denotes powder to solvent wt% ratio.

Sample			Drying time	Solvent reduction	Ref Figure
P:S	**Drying temp.[°C]**	**Binder/Solvent**	**[% of tot]**	**[% of tot]**	
1:2	150	PVDF/NMP	19	11	4.32
1:2	150	Lignin/NMP	29	4	4.32
1:2	50	Lignin/Water	34	13	4.33
1:1.7	50	Lignin/Water	25	11	4.33 ,4.34
1:1.5	50	Lignin/Water	37	12	4.33

Chapter 5

Future Work

In Lu *et al.* [35] study, they used an LFP cathode with leached lignin as a binder and water as solvent. They achieved a discharge capacity of 148 mAh/g (C/10) and 117 mAh/g (1C) on the 4th cycle. In section 4.1.3 the NMC111 cathodes with unleached lignin binder and NMP as solvent achieved a discharge capacity of 140 mAh/g (C/10) on the 4th cycle and 123.6 mAh/g (1C) on the 14th cycle. Despite using unleached lignin as a binder, the results are comparable to what Lu *et al.* [35] reported when using leached lignin. It would therefore be interesting to investigate further using leached lignin in the NMC111 cathode, and water as solvent.

In section 4.1.3 decreased adhesion was observed between the current collector and cathode material with lignin as binder. It could be partly due to poor dissolution of lignin in NMP, which may have created heterogeneous areas in the coating with lower adhesion. The lowered adhesion could also be due to opposing forces between lignin and the current collector (Al-foil). Neither possibility has been tested or proved, and they should be investigated further. Coating the Al-foil with carbon could be a solution to increase adhesion.

Most of the scratch tests (Table 4.1, 4.3 and 4.7) had too high loadings as the depth of the scratch was larger than the coating thickness. To evaluate the cohesion between the coating particles, a more sensitive scratch test with a lower minimum load should be tested (< 30 mN).

The slurry composition used in Section 4.1.4 with powder wt% ratio of 85:10:5 (NMC111:CB:Binder) and powder to water (P:W) ratio of 1:1.7 gave the best slurry properties, but was still not mechanically satisfactory. Therefore, none of the electrodes were cycled. After further work to produce useful electrodes, electrochemical cycling of those would be interesting. To compare them with the improved slurry with PA, electrochemical cycling of the cathodes from that experiment would also be useful. In further work with PA, a treatment to create a protective Li_3PO_4-coating on the NMC111 to avoid Li leaching should be investigated.

To get a more accurate picture of the reproducibility from the convection drying experiments in Section 4.2, the coatings should have a uniform geometry and coating thickness. By measuring the coating area, a specific drying rate relative to the area can be calculated. This will enable comparisons of coatings with non-identical areas.

Increased binder migration was expected when increasing the drying temperature. It would therefore be interesting to do an EDS analysis on the 150 °C - 1 m/s to compare it with the 50 °C - 1 m/s from section 4.2.4 4.2.4. The electrodes should be cut with a FIB to minimise or eliminate what is likely shadow effect on 50 °C - 1 m/s (e.g, Figure 4.29).

Chapter 6

Conclusions

In this thesis, a more sustainable cathode production for LIBs was investigated by varying different slurry parameters to replace the traditional PVDF binder with lignin, followed by exchanging the toxic NMP solvent with water. The thesis subgoal was to dry cathode coatings with varying temperature and air velocity using a custom-made oven to decrease the drying time while maintaining or improving the cathode quality.

Based on the results presented and discussed in Section 4.1.1 and 4.1.2 the composition with powder wt% of 85:10:5 (NMC111:CB:PVDF) and powder to solvent ratio of 1:2 showed the overall best performance both in terms of slurry properties and electrochemical performance. Therefore, this composition was chosen for the standard sample used for comparison when introducing lignin as a binder and water as solvent.

Unleached lignin was introduced as binder by gradually exchanging PVDF binder with lignin. A correlation between increasing lignin content and decreasing mechanical properties and cycling capacity was observed. Introducing lignin and reducing NMP content caused rougher surface textures, which might have been due to poor mixing or dissolution of lignin in NMP. Using pure lignin as a binder with NMP as a solvent caused strong cohesion between the particles but low adhesion between the Al-foil and cathode material. The adhesion increased when the drying temperature was lowered from 90 °C to 50 °C. The capacity also increased with the lower drying temperature. Impressively, the lignin sample dried at 50 °C performed almost as good as the standard samples at lower C-rates. On both high and low C-rates, the sample performed on par with previous studies where they used LFP cathodes with leached lignin binder.

With the exception of the sample using pure lignin as binder calendering increased both the mechanical and electrochemical performance of the cathodes.

Exchanging the NMP solvent with water while using lignin as binder was unsuccessful, and resulted in low viscosity slurries and uneven coating thicknesses. This was likely due to the high surface tension of water and low viscosity, compared to NMP. A powder to water ratio of 1:1.7 showed more promising slurry properties than 1:2 and 1:1.5. Adding PA in order to lower the pH of the slurry and avoid corrosion of the Al-foil current collector improved both the slurry properties and adhesion strength to the Al foil.

Higher temperatures gave shorter drying times, and higher air velocities were tougher on the samples. Changing the air velocity had larger effects on cracking than temperature, with less cracking on lower air velocity. EDS analyses of a standard sample dried at 50 °C showed even distribution of the active material, but some agglomeration of carbon black. The binder was evenly distributed within the material.

Uneven coating thickness and geometry caused uneven drying rates across the coatings. This decreased the validity of the results, and no further conclusions were made.

References

[1] National Centers for environmental information. *Assessing the Global Climate in March 2020*. 2020. URL: https://www.ncei.noaa.gov/news/global-climate-202003 (visited on 24/04/2021).

[2] M.R. Allen et al. 'Framing and Context'. In: *Global Warming of 1.5°C. An IPCC Special Report on the impacts of global warming of 1.5°C above pre-industrial levels and related global greenhouse gas emission pathways, in the context of strengthening the global response to the threat of climate change*. 2018.

[3] IEA. *World Energy Outlook 2020, IEA, Paris*. 2020. URL: https://www.iea.org/reports/world-energy-outlook-2020 (visited on 20/04/2021).

[4] Nic Lutsey. 'Global climate change mitigation potential from a transition to electric vehicles — International Council on Clean Transportation'. In: *The International Council on Clean Transportation* 2015.5 (2015), p. 5. URL: https://theicct.org/publications/global-climate-change-mitigation-potential-transition-electric-vehicles.

[5] Linda Ager Wick Ellingsen et al. 'Life Cycle Assessment of a Lithium-Ion Battery Vehicle Pack'. In: *Journal of Industrial Ecology* 18.1 (2014), pp. 113–124. ISSN: 15309290. DOI: 10.1111/jiec.12072.

[6] European Commission. *Study on the EU's list of Critical Raw Materials*. Tech. rep. 2020. DOI: 10.2873/11619. URL: https://www.etrma.org/news/eu-lists-natural-rubber-as-a-critical-raw-material-reconfirming-its-economic-importance-and-the-need-for-supply-diversification/.

[7] Chengjian Xu et al. 'Future material demand for automotive lithium-based batteries'. In: *Communications Materials* 1.1 (Dec. 2020), p. 99. ISSN: 2662-4443. DOI: 10.1038/s43246-020-00095-x. URL: http://dx.doi.org/10.1038/s43246-020-00095-x%20http://www.nature.com/articles/s43246-020-00095-x.

[8] European Commission. *Commission approves €2.9 billion public support by twelve Member States for a second pan-European research and innovation project along the entire battery value chain*. 2021. URL: https://ec.europa.eu/commission/presscorner/detail/en/IP_21_226 (visited on 07/02/2021).

[9] *Slik ble 2020 et avgjørende år for elektrisk transport og batteriindustri i Norge*. 2021. URL: https://www.innovasjonnorge.no/no/om/nyheter/2021/slik-ble-2020-et-avgjorende-ar-for-elektrisk-transport-og-batteriindustri-i-norge/ (visited on 19/03/2021).

[10] Norges vassdrags- og energidirektorat. *Hvor kommer strømmen fra?* 2020. URL: https://www.nve.no/energiforsyning/kraftproduksjon/hvor-kommer-strommen-fra/?ref=mainmenu (visited on 26/04/2021).

[11] Silje Nornes Bryntesen et al. 'Opportunities for the State-of-the-Art Production of LIB Electrodes—A Review'. In: *Energies (Basel)* 14.5 (2021), p. 1406. ISSN: 1996-1073.

[12] Shabbir Ahmed et al. 'Energy impact of cathode drying and solvent recovery during lithium-ion battery manufacturing'. In: *Journal of Power Sources* 322 (2016), pp. 169–178. ISSN: 03787753. DOI: 10.1016/j.jpowsour.2016.04.102. URL: http://dx.doi.org/10.1016/j.jpowsour.2016.04.102.

[13] Dominic Bresser et al. 'Environmental Science Alternative binders for sustainable electrochemical energy storage – the transition bio-derived polymers'. In: *Energy Environ. Sci.* 11.11 (2018), pp. 3096–3127. DOI: 10.1039/c8ee00640g. URL: http://dx.doi.org/10.1039/C8EE00640G.

[14] Chaofeng Liu, Zachary G. Neale and Guozhong Cao. 'Understanding electrochemical potentials of cathode materials in rechargeable batteries'. In: *Materials Today* 19.2 (2016), pp. 109–123. ISSN: 18734103. DOI: 10.1016/j.mattod.2015.10.009. URL: http://dx.doi.org/10.1016/j.mattod.2015.10.009.

[15] Reiner Korthauer. *Lithium-Ion Batteries: Basics and Applications*. Ed. by Reiner Korthauer. Berlin, Heidelberg: Springer Berlin Heidelberg, 2018, pp. 1–413. ISBN: 978-3-662-53069-6. DOI: 10.1007/978-3-662-53071-9. URL: http://link.springer.com/10.1007/978-3-662-53071-9.

[16] Battery University. *BU-105: Battery Definitions and what they mean*. 2017. URL: https://batteryuniversity.com/learn/article/battery_definitions (visited on 27/04/2021).

[17] Battery University. *Coulombic and Energy Efficiency with the Battery*. 2017. URL: https://batteryuniversity.com/learn/article/bu_808c_coulombic_and_energy_efficiency_with_the_battery (visited on 03/05/2021).

[18] Battery University. *What Is C-rate?* 2017. URL: https://batteryuniversity.com/learn/article/what_is_the_c_rate (visited on 15/03/2021).

[19] Elahe Talaie et al. 'Methods and protocols for electrochemical energy storage materials research'. In: *Chemistry of Materials* 29.1 (2017), pp. 90–105. ISSN: 15205002. DOI: 10.1021/acs.chemmater.6b02726.

[20] Albert Zimmerman. 'Self-discharge losses in lithium-ion cells'. In: *Aerospace and Electronic Systems Magazine, IEEE* 19 (Mar. 2004), pp. 19–24. DOI: 10.1109/MAES.2004.1269687.

[21] Morten Helbæk and Signe Kjelstrup. *Fysikalsk kjemi*. Fagbokforlaget, 2017, p. 796. ISBN: 9788245004045.

[22] Lichuan Wang et al. 'Promises and challenges of alloy-type and conversion-type anode materials for sodium–ion batteries'. In: *Materials Today Energy* 11 (2019), pp. 46–60. ISSN: 24686069. DOI: 10.1016/j.mtener.2018.10.017.

[23] Carl Erik Lie Foss. *Thermal Stability and Electrochemical Performance of Graphite Anodes in Li-ion Batteries*. April. 2014. ISBN: 978-82-326-0126-4 (printed ver.) URL: https://brage.bibsys.no/xmlui/handle/11250/249497.

[24] Xin Li et al. 'Review on comprehending and enhancing the initial Coulombic efficiency of anode materials in lithium-ion/sodium-ion batteries'. In: *Nano Energy* 77.June (2020), p. 105143. ISSN: 22112855. DOI: 10.1016/j.nanoen.2020.105143. URL: https://doi.org/10.1016/j.nanoen.2020.105143.

[25] Allan G. Blackman and Lawrence R. Gahan. *SI Chemical Data*. 7th ed. John Wiley & Sons Australia, 2017, p. 185.

[26] Vivian Murray, David S. Hall and J. R. Dahn. 'A Guide to Full Coin Cell Making for Academic Researchers'. In: *Journal of The Electrochemical Society* 166.2 (2019), A329–A333. ISSN: 0013-4651. DOI: 10.1149/2.1171902jes.

[27] 'A journey through layered cathode materials for lithium ion cells – From lithium cobalt oxide to lithium-rich transition metal oxides'. In: *Journal of Alloys and Compounds* 869 (July 2021), p. 159239. ISSN: 09258388. DOI: 10.1016/j.jallcom.2021.159239. URL: https://doi.org/10.1016/j.jallcom.2021.159239%20https://linkinghub.elsevier.com/retrieve/pii/S0925838821006472.

[28] George E. Blomgren. 'The Development and Future of Lithium Ion Batteries'. In: *Journal of The Electrochemical Society* 164.1 (Dec. 2017), A5019–A5025. ISSN: 0013-4651. DOI: 10.1149/2.0251701jes. URL: https://iopscience.iop.org/article/10.1149/2.0251701jes.

[29] 'Surface/Interfacial Structure and Chemistry of High-Energy Nickel-Rich Layered Oxide Cathodes: Advances and Perspectives'. In: *Small* 13.45 (2017), pp. 1–29. ISSN: 16136829. DOI: 10.1002/smll.201701802.

[30] S.-C. Yin et al. 'X-ray/Neutron Diffraction and Electrochemical Studies of Lithium De/Re-Intercalation in Li1-xCo1/3Ni1/3Mn1/3O2 (x = 0 → 1)'. In: *Chemistry of Materials* 18.7 (2006), pp. 1901–1910. DOI: 10.1021/cm0511769. eprint: https://doi.org/10.1021/cm0511769. URL: https://doi.org/10.1021/cm0511769.

[31] Amnesty International. *Time to recharge*. Tech. rep. 2. 2017, p. 87.

[32] Stefan Jaiser et al. 'Impact of drying conditions and wet film properties on adhesion and film solidification of lithium-ion battery anodes film solidification of lithium-ion battery anodes'. In: *Drying Technology* 35.15 (2017), pp. 1807–1817. ISSN: 0737-3937. DOI: 10.1080/07373937.2016.1276584. URL: https://doi.org/10.1080/07373937.2016.1276584.

[33] Jiantie Xu et al. 'The effect of different binders on electrochemical properties of'. In: *Journal of Power Sources* 225 (2013), pp. 172–178. ISSN: 0378-7753. DOI: 10.1016/j.jpowsour.2012.10.033. URL: http://dx.doi.org/10.1016/j.jpowsour.2012.10.033.

[34] Trupti C Nirmale, Bharat B Kale and Anjani J Varma. 'A review on cellulose and lignin based binders and electrodes: Small steps towards a sustainable lithium ion battery'. In: *International Journal of Biological Macromolecules* 103 (2017), pp. 1032–1043. ISSN: 0141-8130. DOI: https://doi.org/10.1016/j.ijbiomac.2017.05.155. URL: https://www.sciencedirect.com/science/article/pii/S0141813017308929.

[35] Huiran Lu et al. 'Lignin as a Binder Material for Eco-Friendly Li-Ion Batteries'. In: *Materials* 9 (2016), p. 127. DOI: 10.3390/ma9030127.

[36] Silvia Maitz et al. 'Preparation and Characterization of a Water-Soluble Kraft Lignin'. In: 2000052 (2020). DOI: 10.1002/adsu.202000052.

[37] Engineering Toolbox. *Water - Saturation Pressure*. 2004. URL: https://www.engineeringtoolbox.com/water-vapor-saturation-pressure-d%7B%5C_%7D599.html (visited on 02/05/2021).

[38] K. Aim. 'Measurement of Vapor-Liquid Equilibrium in Systems with Components of Very Different Volatility by the Total Pressure Static Method'. In: *Fluid Phase Equilib. 2*. 1978, pp. 119–142.

[39] Dataphysics. 'Surface tension values of some common test liquids for surface energy analysis Surface tension values of some common test liquids for surface energy analysis'. In: 49.0 (2020), pp. 1–4. URL: www.dataphysics-instruments.com.

[40] (Eastman Chemical Company). *N-Methyl-2-Pyrrolidone (NMP)*. 2021. URL: https://www.eastman.com/Pages/ProductHome.aspx?product=71103627 (visited on 10/05/2021).

[41] David L. Wood et al. 'Technical and economic analysis of solvent-based Lithium-Ion electrode drying with water and NMP'. In: *35th Annual International Battery Seminar and Exhibit 2018* 2 (2018), pp. 757–762.

[42] Fisher Scientific UK. *1-Methyl-2-pyrrolidinone, 99%, extra pure, ACROS Organics™*. URL: 1-Methyl-2-pyrrolidinone,%2099%5C%25,%20extra%20pure,%20ACROS%20Organics%E2%84%A2%20%5C%0A (visited on 11/05/2021).

[43] Mohanad N Al-Shroofy. 'Understanding and improving manufacturing processes for making Lithium-Ion battery electrodes'. In: (2017), pp. 1–100. URL: https://doi.org/10.13023/ETD.2017.296.

[44] W. Blake Hawley, Harry M. Meyer and Jianlin Li. 'Enabling aqueous processing for LiNi0.80Co0.15Al0.05O2 (NCA)-based lithium-ion battery cathodes using polyacrylic acid'. In: *Electrochimica Acta* 380 (2021). ISSN: 00134686. DOI: 10.1016/j.electacta.2021.138203.

[45] Werner Bauer et al. 'Electrochimica Acta Effects of pH control by acid addition at the aqueous processing of cathodes for lithium ion batteries'. In: *Electrochimica Acta* 317 (2019), pp. 112–119. ISSN: 0013-4686. DOI: 10.1016/j.electacta.2019.05.141. URL: https://doi.org/10.1016/j.electacta.2019.05.141.

[46] W. Blake Hawley and Jianlin Li. 'Electrode manufacturing for lithium-ion batteries—Analysis of current and next generation processing'. In: *Journal of Energy Storage* 25 (2019), pp. 1–36. ISSN: 2352152X. DOI: 10.1016/j.est.2019.100862.

[47] Jianlin Li et al. 'Toward Low-Cost, High-Energy Density, and High-Power Density Lithium-Ion Batteries'. In: *Jom* 69.9 (2017), pp. 1484–1496. ISSN: 15431851. DOI: 10.1007/s11837-017-2404-9.

[48] Arefeh Kazzazi et al. 'Comparative Analysis of Aqueous Binders for High-Energy Li-Rich NMC as a Lithium-Ion Cathode and the Impact of Adding Phosphoric Acid'. In: *ACS Applied Materials and Interfaces* 10.20 (2018), pp. 17214–17222. ISSN: 19448252. DOI: 10.1021/acsami.8b03657.

[49] 'H 3 PO 4 treatment to enhance the electrochemical properties of Li(Ni 1/3 Mn 1/3 Co 1/3)O 2 and Li(Ni 0.5 Mn 0.3 Co 0.2)O 2 cathodes'. In: *Electrochimica Acta* 301 (2019), pp. 8–22. ISSN: 00134686. DOI: 10.1016/j.electacta.2019.01.153. URL: https://doi.org/10.1016/j.electacta.2019.01.153.

[50] Nicholas Loeffler et al. 'Aqueous Electrode Processing'. In: (2016), pp. 1112–1117. DOI: 10.1002/cssc.201600353.

[51] Sadjad Abasi, Saeid Minaei and Mohammad Hadi Khoshtaghaza. 'Performance of a recirculating dryer equipped with a desiccant wheel'. In: *Drying Technology* 34.8 (2016), pp. 863–870. ISSN: 15322300. DOI: 10.1080/07373937.2015.1021421.

[52] Dilip (DPharma Group Inc) Parikh. 'SOLIDS DRYING: BASICS AND APPLICATIONS'. In: (2014). URL: https://www.chemengonline.com/solids-drying-basics-and-applications/?printmode=1.

[53] Dilip M. Parikh. 'Vacuum Drying: Basics and application'. In: *Chemical Engineering (United States)* 122.4 (2015), pp. 48–54. ISSN: 00092460.

[54] Seyed Ghiaasiaan. *Convective heat and mass transfer*. Cambridge University Press, 2011, p. 548. ISBN: 9781107003507.

[55] Roger A. Freedman Hugh D. Young. *University Physics with Modern Physics, Volume 2 (Chs. 21-37), Global Edition*. Pearson Education Limited, 2015. ISBN: 9781292118598.

[56] Inc. USA METER Group. *Measuring moisture content: It's more complicated than you think*. URL: https://www.metergroup.com/food/articles/measuring-moisture-content-its-more-complicated-than-you-think/ (visited on 15/03/2021).

[57] George W. Scherer. 'Theory of Drying'. In: *Journal of the American Ceramic Society* 73.1 (1990), pp. 3–14. ISSN: 15512916. DOI: 10.1111/j.1151-2916.1990.tb05082.x.

[58] Jana Kumberg et al. 'Drying of Lithium-Ion Battery Anodes for Use in High-Energy Cells : In fl uence of Electrode Thickness on Drying Time , Adhesion , and Crack Formation'. In: 1900126.2 (2019), pp. 1–11. DOI: 10.1002/ente.201900722.

[59] Bastian G Westphal and Arno Kwade. 'Critical electrode properties and drying conditions causing component segregation in graphitic anodes for lithium-ion batteries'. In: *Journal of Energy Storage* 18.January (2018), pp. 509–517. ISSN: 2352-152X. DOI: 10.1016/j.est.2018.06.009. URL: https://doi.org/10.1016/j.est.2018.06.009.

[60] Pengfei Yan et al. 'Intragranular cracking as a critical barrier for high-voltage usage of layer-structured cathode for lithium-ion batteries'. In: *Nature Communications* (2017), pp. 1–9. DOI: 10.1038/ncomms14101.

[61] Honghe Zheng et al. 'Calendering effects on the physical and electrochemical properties of NMC cathodes'. In: *Journal of Power Sources* 208 (2012), pp. 52–57. ISSN: 0378-7753. DOI: 10.1016/j.jpowsour.2012.02.001. URL: http://dx.doi.org/10.1016/j.jpowsour.2012.02.001.

[62] Jiri Nohava. 'Scratch test for characterization of adhesion of electrodes in lithium-ion batteries'. In: *Anton Paar* (2020).

[63] JR. William D Callister and David G. Rethwisch. *Materials Science and Engineering*. 9th. John Wiley & Sons, 2015. ISBN: 978-1-118-31922-2.

[64] Azad Mohammed and Avin Abdullah. 'Scanning Electron Microscopy (SEM): A Review Scanning Electron Microscopy (SEM): A Review'. In: *Proceedings of 2018 International Conference on Hydraulics and Pneumatics - HERVEX* (2018). arXiv: ISSN1454-8003.

Appendix A

Experimental Data

A.1 Slurry values

Table A.1: Weighted amounts of the samples chemicals.

Sample		NMC[g]	CB[g]	PVDF[g]	Lignin[g]	NMP[g]	Water [g]
P:NMP	1:1.5	1.5001	0.1830	0.0886	-	2.6526	-
	1:2(Std)	2.0014	0.2352	0.1181	-	4.7413	-
	1:2.5	1.50996	0.1765	0.09015	-	4.45025	-
wt% NMC111	85 (Std)	2.0014	0.2352	0.1181		4.7413	-
(P:NMP 1:2)	90	1.4992	0.1108	0.05481	-	3.3112	-
	96	1.5029	0.0415	0.0213	-	3.1264	-
Lignin:PVDF	Lignin(1):PVDF(2)	2.002	0.2357	0.02884	0.0891	4.7273	-
(P:NMP 1:2)	Lignin(1):PVDF(1)	2.0010	0.2357	0.0588	0.0585	4.4811	-
	Lignin	1.5001	0.1760	-	0.0886	3.5408	-
P:NMP	1:1	1.5067	0.1772	-	0.0884	1.7631	-
	1:1.5	1.5012	0.1764	-	0.0885	2.6573	-
	1:2	1.5000	0.1767	-	0.0892	3.5409	-
P:W	1:1.5	1.0004	0.117	-	0.0589	-	1.7847 (ink. 0.02 g PEG)
	1:1.7	0.998	0.1173	-	0.1764	-	2.0312 (ink. 0.0124 g PEG)
	1:2	1.004	0.1186	-	0.0583	-	2.4212 (ink. 0.015 g PEG)
	1:2 - PA	0.56	0.0656	-	0.0319	-	1.1126 (ink. 0.201 g PA)

Powder:NMP (P:NMP), Powder:Water (P:W)

A.2 Porosity values

Table A.2: An overview of the non calendered and calendered samples porosity results.

Sample		Porosity		
		Non-calendered	**Calendered**	**Change in porosity**
		[-]	[-]	[%]
P:NMP 1:2, **Lignin:PVDF binder**, 85 wt% NMC111. 150 μm raised gap.				
PVDF		0.50	0.14	56
Lignin(1):PVDF(2)		0.57	0.25	39
Lignin(1):PVDF(1)		0.58	0.45	13
Lignin(50°C)		0.72	Deteriorated from calendering	
P:NMP 1:2, PVDF binder, **90wt% NMC111**. 150 μm raised gap.				
90wt%NMC111		0.72	0.48	20
Lignin binder, water as solvent and PA as a pH controller. 150 μm raised gap.				
Lignin/water-PA		0.66	0.30	38
P:NMP 1:2, PVDF binder, 85wt%NMC111, 200 μm raised gap.				
Drying temp.[°C]	Air velocity [m/s]			
22	0	0.53	0.32	25
50	1.0	0.54	0.41	14
90	1.0	0.51	0.38	15
150	1.0	0.62	0.52	9

Bold text is the parameters being varied, Powder:NMP (P:NMP)

A.3 Cycle data

Table A.3: An overview of the assembled coin cells

Sample	Coin cell	Cycle	DisCap [mAh/g]	Capacity retention [%]
P:NMP, PVDF binder, 85 wt% NMC111				
1:1.5	1	N/A	N/A	N/A
1:2	1	1 - 19	156 - 145.4	93
	2	1 - 19	152 - 122	80.33
	3	1 - 19	116.7 - 59.4	50.9
	4	1 - 19	99.9 - 88.1	88.19
	5	1 - 19	112.9 - 90.4	80.1
	6*	1 - 35	145.3 - 147.9	102
1:2.5	1	1 - 19	149.8 - 132.6	88.52
P:NMP 1:2, PVDF binder, **90wt% NMC111**				
90	1	1 - 19	130.7 - 108.4	82.9
	2[c]	1 - 59	140.3 - 56.4	40.2
	3*	2 - 35	137.7 - 135.3	98.3
	4*[c]	1 - 35	0 - 103.1	103.1
P:NMP 1:2, **Lignin:PVDF binder**, 85 wt% NMC111				
1:1	1	1 - 19	110.9 - 20.7	18.67
	2*	1 - 35	0.7 - 19.7	281
	3[c]	1 - 99	136.6 - 46.3	33.9
	4*[c]	1 - 35	94.7 - 104.3	110
1:2	1*	1 - 35	148.9 - 121.7	81.7
	2*[c]	1 - 35	144 - 133.9	93
P:NMP 1:2, **Lignin binder**, 85 wt% NMC111				
90 °C	1	1 - 19	79.1 - 46.9	59.3
	2	1 - 19		Failed 3rd cycle
	3*	1 - 26	85.5 - 1.1	Failed at C/2 (cycle 11)
50 °C	4*	3 - 34	138.4 - 0	Failed at 2C (cycle 20)

Bold text is the parameters being varied, Powder:NMP (P:NMP), * rate test, [c] calendered samples

Appendix B

Python Code for Drying Plots

```
Created on Sun Apr 18 21:23:07 2021

@author: Camilla
"""

import numpy as np
import matplotlib.pyplot as plt



with open('MC_150_05_std2.txt', 'r') as f:
    lines = f.readlines()
    sek = [float(line.split()[0]) for line in lines]
    wt = [float(line.split()[1]) for line in lines]
    ms = [float(line.split()[2]) for line in lines]

n = 0
sek1 = []
wt1 = []


for i, p in enumerate(ms):
    if n == 0:
        if p == 0:
            n = 1
    elif n==1 and p != 0:
        n = 0
        sek1.append(sek[i-1])
        wt1.append(wt[i-1])

coefficients = np.polyfit(sek1, wt1, 4)
poly = np.poly1d(coefficients)

new_x = np.linspace(sek1[0], sek1[-1])
new_y = poly(new_x)

with open('MC_150_05_lignin2.txt', 'r') as f:
    lines = f.readlines()
    sek = [float(line.split()[0]) for line in lines]
    wt = [float(line.split()[1]) for line in lines]
    ms = [float(line.split()[2]) for line in lines]

q = 0
sek2 = []
wt2 = []
```

```
for i, p in enumerate(ms):
    if q == 0:
        if p == 0:
            q = 1
    elif q==1 and p != 0:
        q = 0
        sek2.append(sek[i-1])
        wt2.append(wt[i-1])



coefficients1 = np.polyfit(sek2, wt2, 4)
poly1 = np.poly1d(coefficients1)


new_x1 = np.linspace(sek2[0], sek2[-1])
new_y1 = poly1(new_x1)


plt.figure(figsize=(15,10))
plt.rcParams['font.family'] = 'serif'
plt.plot(new_x, new_y, color='#004c69', linewidth=1.5)
plt.plot(new_x1, new_y1, color= '#ff8d00', linewidth=1.5)
plt.plot(sek2, wt2, "x", color = '#ff8d00')
plt.plot(sek1, wt1, ".", color = '#004c69')
plt.axhline(y=0, linestyle = 'dotted', color = '#616161')
plt.xlim(0,800)
plt.ylim(-0.03,1)
plt.axhline(y=0, color='616161', linestyle='dotted')
plt.legend(['PVDF','Lignin'], prop={"size":28})
plt.xlabel('Time [s]', fontsize=28)
plt.xticks(fontsize=22)
plt.ylabel('Moisture Content [g_rem / g_tot]', fontsize=28)
plt.yticks(fontsize=22)
plt.show()
```

Figure B.1: Python code for calling on the last stable value before air flow was started again in the drying interval (plotted as symbols). The code for the best fit polynom was set to 4th degree and is from line 33-37 and 60-65. Line 48 is missing but it is an empty line.

```python
# -*- coding: utf-8 -*-
"""
Created on Mon Mar 15 14:59:47 2021

@author: Camilla
"""

import numpy as np
import matplotlib.pyplot as plt


with open('room_temp_std.txt', 'r') as f:
    lines = f.readlines()
    x = [float(line.split()[0]) for line in lines]
    y = [float(line.split()[1]) for line in lines]

a = 1.166*0.668

my = np.array(y)
mc = (a+my)/a

plt.figure(figsize=(15,10))
plt.rcParams['font.family'] = 'serif'
plt.plot(x , mc, color='#63ace5', linewidth=1.5)
plt.axvline(x=86400, color='r', linewidth=0.4)
plt.axvline(x=86400*2, color='r', linewidth=0.4)
plt.axhline(y=0, color='616161', linestyle='dotted')
plt.xlim(0,240000)
plt.ylim(-0.05,1)
plt.xlabel('Time [s]', fontsize=28)
plt.xticks(fontsize=22)
plt.ylabel('Moisture Content [g_rem / g_tot]', fontsize=28)
plt.yticks(fontsize=22)
plt.legend(['Room temperature (~22°C) - 0 m/s'], prop={"size":28})
plt.show()
```

Figure B.2: Python code for calling on all the values plotted. Where a is the total amount of slurry used multiplied with the proportion of moisture in the cathode slurry

Appendix C

Risk Assessment

Unit/Department:	Department for Energy and Process Engineering				**Date created**	28.01.2021		
Responible faculty leader(Name):	Terese Løvås				**Last revised**	06.02.2021		
Responsible for the activity being risk assessed (Name):	Nora Kvalsvik, Camilla Jektvik, Ingeborg Ellingsen							
Participants (Name):	Nora Kvalsvik, Camilla Jektvik, Ingeborg Ellingsen, Silje Nornes Bryntesen							
Description of activity, area mv.:	The activity connects with a bachelor thesis where the overall activity is Li-ion coin cell fabrication at the HVAC-lab. The activity's goal is to understand the effect of different drying parameters when drying NMC111, characterise the crystal structure, and understand how this impacts the battery half cell's electrochemical performance.							
Activity/Task	**Possible accidents**	**Existing risk control**	**Probability assessment (P)**	**Impact assessment (I)**		**Risk value (P x I)**	**Proposals for preventive and/or corrective measures**	**Risk value after measures (P x I)**
			(1-5)	Human (1-5)	Ec/materials (1-5)			
Heat treatment of cathode slurry	Burning (burns on skin)	Reminding people it's hot Oven glove Fire extinguisher	3	1		3		
NMP	Spill on skin	Gloves, lab coat	2	1		2		
	Irritation in airways	Work with chemical under a ventilator	2	2		4	Use a fume cupboard	2
	Irritation in eyes	Protective eyewear (lab glasses)	1	2		2		
	Damage to foster	Handle chemical under ventilation to prevent inhalation.	1	1		1		
	Health hazard	Ensure proper disposal of chemical	1			2		
Electrochemical characterization; Arbin Battery Cycler	Electric shock	Letting people know it's turned on	1	2		2		
	Catching fire	The current used are very small Fire extinguisher	1	1		1		
Glovebox	Spill electrolyte	Absorbing tissues are available inside the glovebox, and its filters prevent human exposure to dangerous fumes	3		1	3		
Carbon Black	Swallowing	Not allowed to eat in laboratory	1	2		2		
	Skin exposure	Wear gloves and don't roll up the sleeves on the labcoat	3	1		3		
	Eye exposure	Safety goggles are mandatory in the lab	1	2		2		
	Inhalation	Work with chemical under a ventilator	3	1		3		

Unit/Department:	Department for Energy and Process Engineering				**Date created**	28.01.2021		
Responible faculty leader(Name):	Terese Løvås				**Last revised**	06.02.2021		
Responsible for the activity being risk assessed (Name):	Nora Kvalsvik, Camilla Jektvik, Ingeborg Ellingsen							
Participants (Name):	Nora Kvalsvik, Camilla Jektvik, Ingeborg Ellingsen, Silje Nornes Bryntesen							
Description of activity, area mv.:	The activity connects with a bachelor thesis where the overall activity is Li-ion coin cell fabrication at the HVAC-lab. The activity's goal is to understand the effect of different drying parameters when drying NMC111, characterise the crystal structure, and understand how this impacts the battery half cell's electrochemical performance.							
Activity/Task	**Possible accidents**	**Existing risk control**	**Probability assessment (P)**	**Impact assessment (I)**		**Risk value (P x I)**	**Proposals for preventive and/or corrective measures**	**Risk value after measures (P x I)**
			(1-5)	Human (1-5)	Ec/materials (1-5)			
PVDF	Swallowing	Not allowed to eat in laboratory	1	1		1		
	Skin exposure	Wear gloves and don't roll up the sleeves on the labcoat	2	1		2		
Virus	Getting exposed to Covid-19	1 m distance to other people in the laboratory, wear mask, antibac hands	3	2		6	Register attendance, keep the cohort small at leisure, follow guidlines at all time	4
Electrolyte	Fire	Keep away from heat/sparks/open flames/hot surfaces. Fire extinguishers are available in the lab	1	2		2		
	Swallowing	Not allowed to eat in laboratory	1	2		2		
	Skin exposure	Wear proper lab-clothing + labcoat and gloves	2	1		2		
	Eye exposure	Wear safety goggles	2	2		4	Work in fume cupboard	2
	Chronic damage to kidneys	Work with chemical in a fume cupboard or under ventilator, avoid prolonged exposure	1	2		2		
	Health hazard	Ensure proper disposal of chemical	1			2		
NMC111	Skin exposure	Wear labcoat and gloves	3	1		3		
	May cause cancer	Work with chemical under ventilator	1	3		3		
	Health hazard	Ensure proper disposal of chemical	1			2		

Appendix D

Popular Science Article

Waste From Norway's Paper Industry Could Lead to a More Sustainable Production of Electric Cars

Camilla Jektvik, Ingeborg Ellingsen, Nora Kvalsvik
Norwegian University of Science and Technology
Faculty of Natural Science
Department of Material Science and Engineering

Norway is already in a position to be Europe's battery, with energy storage in hydropower plants. Now, Norway can be a valuable asset in the production of lithium-ion battery (Li-ion battery). The increasing popularity of electric vehicles in combination with Norway's access to renewable energy has opened opportunities to establish a sustainable battery production [1, 2]. In this article, we are exploring how this can be accomplished by switching the plastic PVDF binder with lignin derived from plant matter in a part of the battery. Doing this successfully will allow us to exchange the toxic solvent with water, making the battery production less energy demanding.

Whats happening inside the Li-ion battery?

Firstly, a Li-ion battery converts chemical energy to electrical energy. This can be either non-rechargeable or rechargeable. The Li-ion battery consists of an electrolyte which transfers ions, a separator to avoid short circuit, and a graphite anode and Li-oxide cathode. During charging, positive lithium ions move from the layers of the cathode material through the electrolyte and into the graphite layers where they each receive an electron. During discharge, the lithium ions move from the graphite layers and release their electrons. The current collector transfers the electrons produced and sends them into an external circuit, where the flow of electrons can be used (e.g., to drive your car). It is important that the electrolyte has good ionic conductivity and poor electrical conductivity as you want the electrons to go into the external circuit, while the lithium ions can move through the electrolyte [3, 4]. Figure 1 illustrates the basic principle and the configuration of a Li-ion battery when discharging (i.e., when you are driving your electric car). Li-ion batteries have the highest energy density of all rechargeable batteries. In other words, they can store the most energy per weight [5]. This is very important as low battery weight means that the car will be lighter, and can use the stored energy to drive longer. As of today, the cathode is the capacity-limiting factor in a Li-ion battery, and therefore a hot area of research.

How is the cathode produced?

To make the cathode production easy to explain, we can compare it to baking a cake. In a cake you need flour, sugar, eggs and milk. This can be transferred to the cathode production, where you would need:

- Active Material (flour) - which provides Li-ions to react and produce electricity.
- Conductive Agent (sugar) - to transfer electrons between the cathode and the current collector.
- Binder (eggs) - to hold the cathode together.
- Solvent (milk) - to ensure proper mixing and attain the desired consistency.

A commonly used active material in the electric car battery is the NMC material, which contains lithium, nickel, manganese, cobalt and oxygen. The conductive agent is usually carbon black. The binder typically consists of PVDF, a non-reactive, fluorine-containing plastic [6]. The materials and their dispersion in the cathode is shown in Figure 2. PVDF is

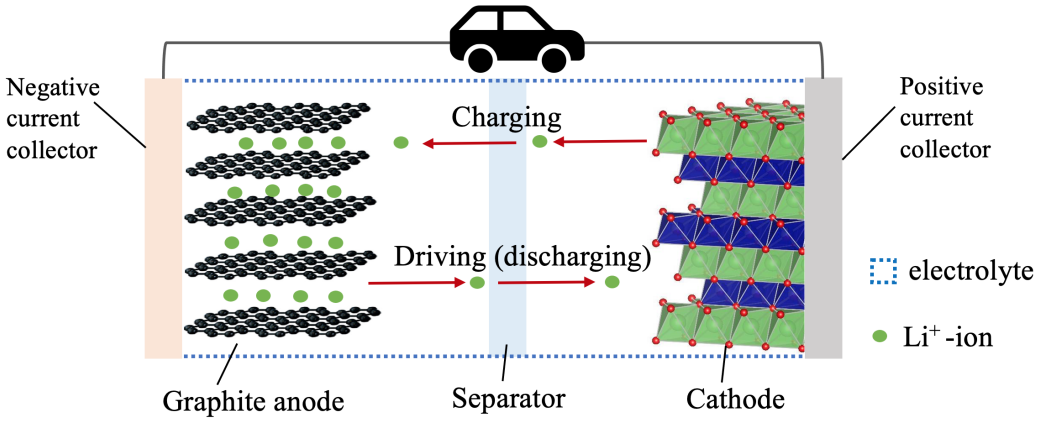

Figure 1: *Schematic of a LIB showing the direction electrons and ions during charge and discharge.*

only soluble in few toxic solvents such as NMP; therefore, NMP is used to mix the cathode components listed above into a slurry (cake batter). After mixing, the slurry is coated onto a current collector, usually an aluminium foil. The slurry must then be dried to remove the NMP before it can go into the battery, just like you have to bake the cake before you eat it. Since NMP is toxic, it can not be released into the atmosphere. That means you need to capture and rinse all the air used in drying, which requires a lot of energy. Cathodes with PVDF binder are also challenging to recycle, as when burning plastics containing flourine, extremely toxic gases are produced that are known to affect the ozone layer [7].

Introducing lignin as a binder

Let's say you want to do something for the environment and decide to go vegan! Eggs and milk play important roles in the recipe, so you would need to investigate possible replacements for the cake to still be as good. This is what we have done with our cathode material. One possible replacement for the PVDF binder is lignin. Lignin can be obtained from the Norwegian paper and pulp industry "waste," as it is a natural component found in all plants and trees. For the exchange to be truly successful, the battery needs to perform as well or better with lignin as it does with PVDF. We managed to create a Li-ion battery that could charge and discharge almost as well as the traditional PVDF cell (shown in Figure 3a). The battery with lignin also performed as well as the PVDF when charging slowly, but not as well with faster charging (Figure 3b). To achieve these results we had to lower the drying temperature. Even though the battery with lignin did not perform as well as the one using PVDF, the results are promising for future work. One of the important parts of replacing our PVDF "egg" with lignin is that lignin is soluble in more environmentally friendly liquids. This means that we can test water as solvent to replace the toxic NMP. Since water is natural we don't need to collect it from the air after drying. This could save a lot of energy in the production of Li-ion batteries in the future.

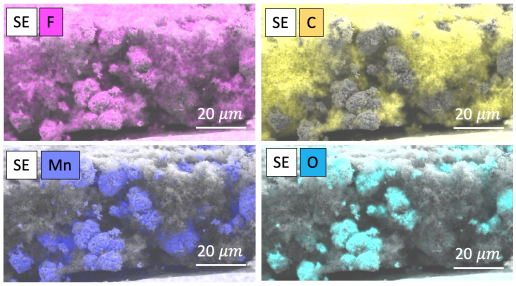

Figure 2: *EDS analysis on SEM image of a cathode cross section. PVDF binder is traced as fluoride (pink), Carbon black carbon (yellow), NMC particle through Manganese (blue) and oxygen (turquoise).*

Future opportunities

There are many things to keep in mind when exchanging ingredients in a well known cake recipe. The best result is a cake that nobody could even

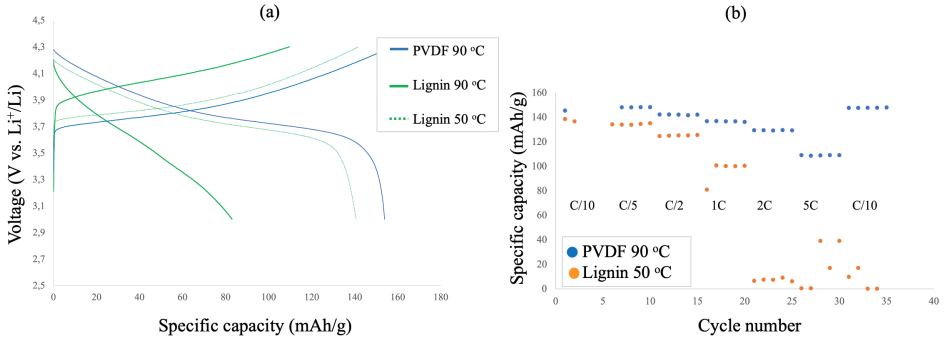

Figure 3: *(a) charge/discharge plot (b) A test to see how the battery holds up on higher charge/discharging rates for a PVDF sample (blue) and a lignin containing sample (orange) dried at 50 °C and 90 °C*

tell is vegan. The same thing relates to the Li-ion battery as you do not want it to affect the taste (i.e., the battery performance) and fall apart when you cut it (i.e., mechanical strength).

By following the same recipe for the toxic cathode, we experienced that an aqueous cathode would need less solvent to achieve the desired consistency. The aqueous slurry we made was too thin, which resulted in an uneven coating thickness and an undesired geometry - like a wonky cake. In other words, when exchanging NMP (milk) with water, we need to find new amounts of the other ingredients to achieve the desired consistency of our "cake batter."

While work remains to perfect the recipe, the results look promising. Replacing the PVDF egg with lignin, and the toxic solvent with water is a big step in the right direction. It will open opportunities for a more environmentally friendly cathode production, and in turn make the battery-production for electric cars more sustainable.

References

[1] *Slik ble 2020 et avgjørende år for elektrisk transport og batteriindustri i Norge*. 2021. URL: https://www.innovasjonnorge.no/no/om/nyheter/2021/slik-ble-2020-et-avgjorende-ar-for-elektrisk-transport-og-batteriindustri-i-norge/ (visited on 03/19/2021).

[2] Norges vassdrags- og energidirektorat. *Hvor kommer strømmen fra?* 2020. URL: https://www.nve.no/energiforsyning/kraftproduksjon/hvor-kommer-strommen-fra/?ref=mainmenu (visited on 04/26/2021).

[3] Reiner Korthauer. *Lithium-Ion Batteries: Basics and Applications*. Ed. by Reiner Korthauer. Berlin, Heidelberg: Springer Berlin Heidelberg, 2018, pp. 1–413. ISBN: 978-3-662-53069-6. DOI: 10.1007/978-3-662-53071-9. URL: http://link.springer.com/10.1007/978-3-662-53071-9.

[4] Chaofeng Liu, Zachary G. Neale, and Guozhong Cao. "Understanding electrochemical potentials of cathode materials in rechargeable batteries". In: *Materials Today* 19.2 (2016), pp. 109–123. ISSN: 18734103. DOI: 10.1016/j.mattod.2015.10.009. URL: http://dx.doi.org/10.1016/j.mattod.2015.10.009.

[5] Merethe Ruud. *Hvordan fungerer litiumholdige batterier?* 2018. URL: https://www.tu.no/artikler/hvordan-fungerer-litiumholdige-batterier-br/454352 (visited on 03/15/2021).

[6] Jiantie Xu et al. "The effect of different binders on electrochemical properties of". In: *Journal of Power Sources* 225 (2013), pp. 172–178. ISSN: 0378-7753. DOI: 10.1016/j.jpowsour.2012.10.033. URL: http://dx.doi.org/10.1016/j.jpowsour.2012.10.033.

[7] Dominic Bresser et al. "Environmental Science Alternative binders for sustainable electrochemical energy storage – the transition bioderived polymers". In: *Energy Environ. Sci.* 11.11 (2018), pp. 3096–3127. DOI: 10.1039/c8ee00640g. URL: http://dx.doi.org/10.1039/C8EE00640G.

NTNU

Kunnskap for en bedre verden